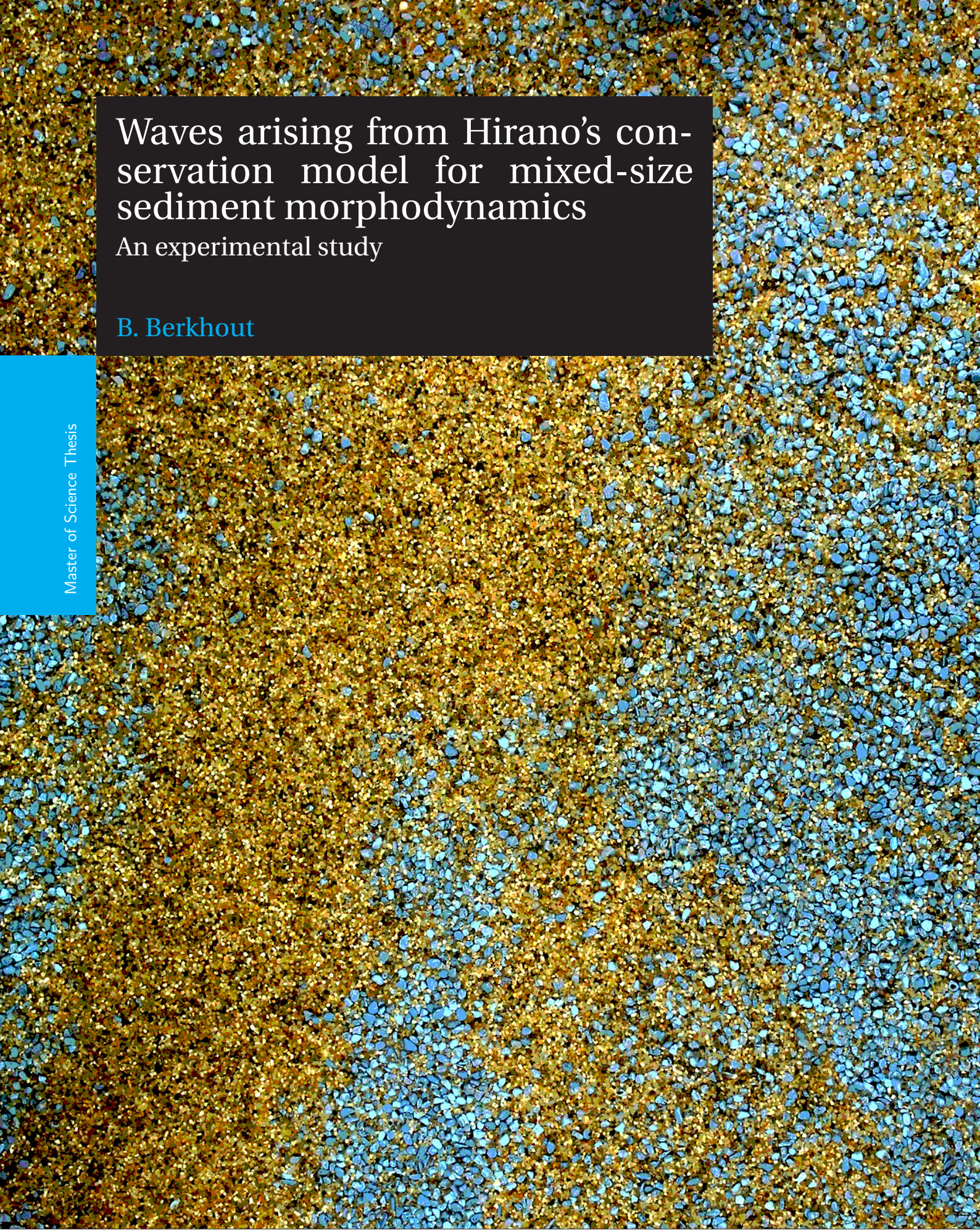

Waves arising from Hirano's conservation model for mixed-size sediment morphodynamics

An experimental study

B. Berkhout

Master of Science Thesis

TU Delft Delft University of Technology

Challenge the future

Waves arising from Hirano's conservation model for mixed-size sediment morphodynamics

Cover: Areal photograph of the bed with mixed-size sediment of the flume experiment performed in this research.

Waves arising from Hirano's conservation model for mixed-size sediment morphodynamics

AN EXPERIMENTAL STUDY

by

Bart Berkhout

in partial fulfillment of the requirements for the degree of

Master of Science
in Civil Engineering

at the Delft University of Technology,
to be defended publicly on Tuesday April 14, 2015 at 15:00 PM.

Student number:	1513710	
Supervisor:	Dr. ir. A. Blom	Delft University of Technology
Thesis committee:	Prof. dr. ir. W. S. J. Uijttewaal,	Delft University of Technology, chair
	Dr. ir. C. J. Sloff,	Deltares, Delft University of Technology
	Dr. G. Stecca,	Delft University of Technology

An electronic version of this thesis is available at http://repository.tudelft.nl/.

TU Delft Delft University of Technology

Preface

This thesis concludes the Master of Science (MSc) programme of Civil Engineering, Hydraulic Track, specialization Environmental Fluid Mechanics and River Engineering, at Delft University of Technology.

In this thesis an experimental study is performed to investigate the physical behaviour of waves arising from the Saint-Venant-Hirano model for mixed-size sediment morphodynamics. The experiments took place in a flume.

After an introduction and review of the research conducted in the past years on this subject, both mathematically and physically, a description is given of the flume experiments performed. The results of the experiments are presented accompanied by analysis and interpretation of the results. Finally a numerical study, simulating the flume experiments, was carried out and the results of which are compared with the measured data.

In the first place I would like to thank Astrid Blom for her daily supervision, valuable guidance and insight she gave on the topic of mixed-size sediment transport and teaching me to write in a proper style. Guglielmo Stecca is thanked for sharing his knowledge on the more mathematical description of this thesis' topic and his patience in helping me with the modelling. The other members of the 'weekly sorted meetings', Clara, Victor and Velia are thanked for their input and support both in the meetings and out.

Further I would like to thank the other members of the graduation committee for their valuable input during the meetings. Thanks is also in order for the technicians of the Water Lab, ruling fiercely but righteously, for giving me insight in practical problems and aiding in constructing the experimental set-up.

B. Berkhout
Den Haag, April 2015

Abstract

River bed degradation is sometimes counteracted with nourishment of sediment material. Sediment nourishment is the dumping of a certain amount of sediment of mixed grain sizes which is transported and deposited over a river reach by the flow. Numerical models — which include Hirano's sediment continuity model for mixed-size sediment — can be used to predict the transport of different sediment fractions (the waves due to spatial variations in the grain size distribution of the bed material are here called Ribberink waves) in the dumped material to find an optimal grain size distribution of the nourishment. Little is known how well these numerical predictions represent physical reality. The uncertainty in predictions of the behaviour of the transport of mixed-size sediment can have severe impact: the grain size distribution influences degradation and aggradation processes and bed friction, both, directly or indirectly, influence water levels and flow velocities that are important for designing measures for hinterland protection. Moreover, numerical models predict Ribberink waves travelling faster than associated bed level perturbations (De Vries waves), which is never observed in reality.

In order to gain insight into the behaviour of morphodynamic changes with mixed-size sediment — especially with regards to the Ribberink waves — two flume experiments were conducted in the Water Lab of the faculty of Civil Engineering and Geosciences of Delft University of Technology. The first experiment is a case with uniform tracer sediment, installing a shoal of different colour than the sediment in the downstream part of the flume. The shoal was installed for the upstream end. Comparing the outcomes of the latter experiment with a numerical simulation gives insight into the question if the Ribberink wave travelling faster than the De Vries wave is an artefact of the Hirano model or that it has physical meaning and relevance. The second experiment was an experiment with a bimodal sediment mixture. A shoal consisting of the coarser fraction is installed at the upstream part of the flume. The coarse fraction has a different colour than the fine fraction so that we were able to track it through the domain.

The tracer experiment shows a distinct propagation of the shoal through the domain. Downstream of the shoal no degradation occurred. The material initially present in the shoal did not travel faster than the shoal. The numerical simulation of the experiment shows tracer material being transported faster than the shoal. The tracer material spread over the bed downstream of the shoal, reaching the end of the computational domain before the end of the simulation.

The mixed-size sediment experiment shows a distinct propagation of the shoal through the domain (De Vries wave), preceded by an degradational wave (Ribberink wave). This degradational wave is caused by the spatial increase of the sediment transport rate, which is the net effect of: (a) a streamwise increasing flow depth; (b) a streamwise decreasing average grain size diameter of the bed surface, and; (c) a turbulent recirculation zone increasing local sediment transport capacities. In the area of degradation, the bed gradually becomes finer than the initial situation. A numerical reproduction of this experiment reproduced the experiment well, showing the same propagation celerity of the shoal and the associated erosion wave (but less deep), but shows no significant change of the grain size distribution compared to the initial bed of the bed downstream of the shoal. The predicted Ribberink wave thus travels with the same celerity as the measured Ribberink wave and does not precedes the De Vries wave.

The conclusions of this thesis show that the grain size distribution of a sediment nourishment is of great influence on the propagation of the nourished material and on bed level changes downstream of the nourishment. As concluded from the flume experiments, when the nourished material (a hump similar to the shoal of the conducted experiments in this thesis) is coarser than the river bed, an erosional wave downstream of the nourishment will arise, travelling with the same celerity as the nourished material. If the nourishment is done to protect or counteract river bed degradation, this erosional effect caused by the shoal should be considered seriously.

Contents

Nomenclature

A	Parameter in Meyer-Peter-Müller formula	$[-]$
B	Flume width	$[m]$
B	Parameter in Meyer-Peter-Müller formula	$[-]$
b	Degree of non-linearity: $b = (u/q_b)(dq_b/du)$	$[-]$
C	Dimensionless Chézy coefficient: $C = C_D/\sqrt{g}$	$[-]$
C_D	Dimensional Chézy coefficient	$[m^{1/2}s^{-1}]$
c_{bed}	Celerity of a perturbation in the bed (De Vries wave)	$[ms^{-1}]$
c_{mix}	Celerity of a perturbation grain size distribution of the bed in the active layer (Ribberink wave)	$[ms^{-1}]$
d_{50}	Median grain size	$[m]$
$d_{k,90}$	Grain size for which 90% is finer in size fraction k	$[m]$
d_{sk}	Grain diameter of size fraction k	$[m]$
$\overline{d_s}$	Average grain diameter	$[m]$
$\overline{d_{90}}$	Geometric grain size of the mixture for which 90% of the grains is finer	$[m]$
$\overline{d_{sT}}$	Average grain diameter in bed load	$[m]$
f_k^I	Volume fraction content of at the interface of active layer and substrate of size fraction k	$[-]$
F_{Ai}	Areal fraction content of size fraction i	$[-]$
F_{ak}	Vertically-averaged volume fraction content of size fraction k in the active layer	$[-]$
f_{sk}	Non-vertically mixed fraction content of the substrate of size fraction k	$[-]$

F_{Tk}	Volume fraction content of size fraction k in the bed load	$[-]$
F_{Vi}	Volume fraction content of size fraction i	$[-]$
Fr	Froude number	$[-]$
g	Acceleration due to gravity	$[ms^{-2}]$
h	Flow depth	$[m]$
k	Sediment fraction index	$[-]$
L_a	Active layer thickness	$[m]$
m_{sub}	Mass of submerged sediment	$[kg]$
N	Total number of sediment fractions	$[-]$
$P_{a,b}$	Volume fraction content of sediment mixtures a or b (Suzuki, 1976)	$[-]$
q	Water discharge per unit width	$[m^2s^{-1}]$
q_b	Total sediment discharge per unit width	$[m^2s^{-1}]$
Q_{bk}	Transport capacity of size fraction k for the given hydraulic load	$[m^2s^{-1}]$
q_{bk}	Sediment discharge per unit width of size fraction k	$[m^2s^{-1}]$
t	Time	$[s]$
u	Mean flow velocity: $u = qh^{-1}$	$[ms^{-1}]$
V_s	Volume of sediment	$[m^3]$
x	Streamwise coordinate	$[m]$
Δz_{max}	Maximum erosion depth relative to the initial bed level	$[m]$
Δ	Relative density: $\Delta = (\rho_s/\rho_w) - 1$	$[-]$
δ	Shoal height	$[m]$
ϵ	Porosity	$[-]$
η	Bed elevation	$[m]$
λ_i^*	Dimensionless eigenvalue: $\lambda_i^* = \lambda_i/u$	$[-]$
λ_i	Eigenvalue	$[ms^{-1}]$
μ	Ripple factor	$[-]$

ψ	Variation in total bed load discharge per unit variation in water discharge	$[-]$
ρ_s	Sediment density: $\rho_s = 2650$	$[kgm^{-3}]$
ρ_w	Sediment density: $\rho_w = 1000$	$[kgm^{-3}]$
θ_c	Critical Shields parameter	$[-]$
θ_k	Shields parameter of size fraction k	$[-]$
ξ_k	Hiding-exposure correction factor	$[-]$

1 | Introduction

1.1 Introduction

River beds are sometimes protected from degradation by a nourishment of sediment material (Figure 1.1). With a nourishment, an amount of sediment of mixed grain sizes is dumped and spread over a river reach by the flow. Knowledge on the propagation of the nourished sediment is paramount to obtain optimal efficiency in protecting the river bed. Smaller grains are entrained and transported more easily by the flow; a nourishment consisting of finer sediment can cause the material to spread over a river reach larger than needed or causes the material to deposit too far downstream, outside the region of interest. On the other hand, when using coarser sediment, the stabilizing effects can remain too local.

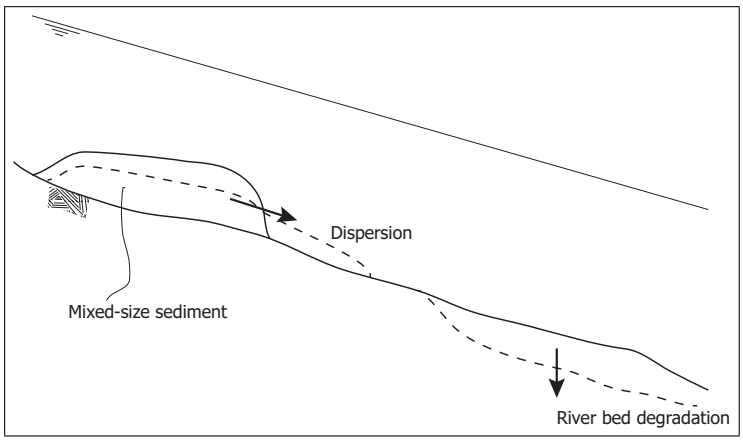

Figure 1.1: River nourishment to protect river bed from degradation or to restore eroded river bed.

This difference in behaviour between finer and coarser material indicates that the different grain size fractions within the supplied sediment propagate with different speeds. This is illustrated by Figure 1.2 which shows field data from a reach of the Rhine river near Iffezheim where a long-term experiment with tracer material was conducted (Gölz et al., 2006). The Iffezheim

case is commented on in more detail in Section 2.2. The figure shows the displacement in time of the centroid of the distribution of a sediment fraction. The finer fractions move with a higher celerity than the coarser fractions. In general, perturbations in the bed level travel through the domain as a wave with a celerity. This 'bed' wave is defined from now as a *De Vries wave* after De Vries (1965) who was the first to describe and identify this wave. A bed of mixed sediment can be represented by an average diameter of the mixture, which changes when the grain size distribution changes. These changes in bed grain size distribution also travel through the domain and can be seen as a wave with a celerity. From now we will define this wave as a *Ribberink wave* after Ribberink (1987) who was the first to describe this wave. So, the propagation of different fractions can be seen as kinematic waves of grain size distribution of the river bed, known as Ribberink waves.

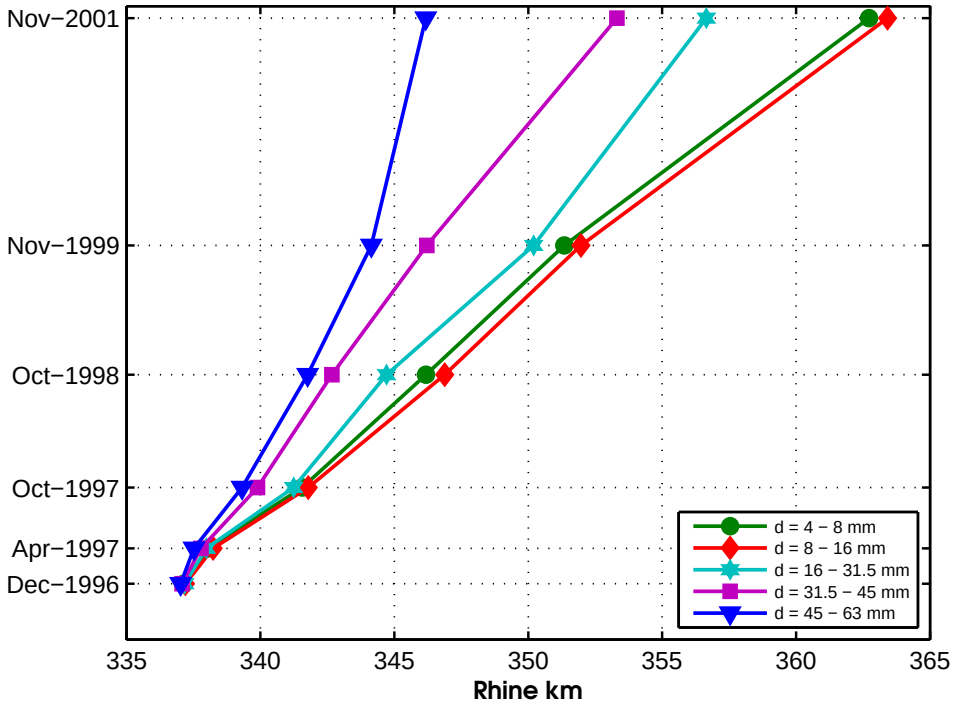

Figure 1.2: Displacement of the centroid of the distribution of a sediment fraction over the longitudinal distance in time, per sediment fraction of the Iffezheim tracer case (Gölz et al., 2006). The finer material is transported faster than the coarser material.

Since the knowledge on the propagation of the supplied sediment is of importance, knowledge on the celerities of the propagation of the grain size fractions in the mixture is essential. Numerical models can be used to simulate the behaviour of Ribberink waves.

To account for sediment sorting in a numerical model a sediment continuity model for non-uniform sediment needs to be included. Hirano (1971, 1972) derived such an equation for conservation of sediment mass with a homogeneous active layer or transport layer that represents the sediment that interacts with the flow and is affected by erosion and sedimentation, taking different sediment fractions into account.

The behaviour of mixed-size sediment and the associated waves are analytically well studied over the years. These studies provide valuable information on the propagation of Ribberink waves.

1.2 Problem

The problem is that little is known about the physical celerities of Ribberink waves and how well the analytical and numerical celerities represent the actual physical celerities.

This is of importance since the absence of scientific knowledge on the propagation of Ribberink waves induces problems to the physical representation and questions the reliability of the numerical outcomes, and thus the reliability of for instance protection measures such as dikes, revetments or any other hinterland protection. The design of these measures rely on water levels and flow velocities, which are directly influenced by changes in bed elevation which in their turn are caused by erosion and sedimentation. The grain size distribution of the bed changes gradients in sediment transport and therefore influence sedimentation and erosion processes. Sorting affects the flow also via the bottom roughness as it is determined by the grain size distribution of the bed and bed-form geometry.

Besides, a second problem arises when solving Hirano's equation in a numerical morphological model. The results show a separation of the Ribberink wave and the wave associated with bed disturbances where the Ribberink wave travels with a higher celerity than the De Vries wave (Berkhout, 2014). This difference between the bed perturbation celerity and the Ribberink wave celerity however, has never been observed in physical reality. As it is unknown if this separation of De Vries and Ribberink wave also occurs in reality, the accuracy of the numerical predictions is questionable.

Mosselman and Sloff (2007) also found that Ribberink waves travelled faster than the bed perturbation with their numerical model of the bifurcation of the Dutch Rhine at Pannerden, which is based on Hirano's sediment continuity model. Patches of bed grain size distribution migrated so fast — the migrating patches are changes in the bed's grain size distribution, which can be seen as Ribberink waves — that they reduced all gradients in sediment transport capacity to zero before any significant bed level changes (De Vries wave) could occur. The bed hardly showed any erosion and sedimentation despite substantial sediment transport capacity and considerable

gradients in the initial sediment transport capacity. Their research shows the importance of modelling mixed sediment processes correctly and moreover highlights the importance of enlarging the knowledge on the behaviour of Ribberink waves. The correctness of the outcomes of the numerical model of the Rhine bifurcation at Pannerden has for instance implications for flood risks, navigation depth and regional water supply.

1.3 Objective

The main objective of this research is to gain insight in the physical behaviour of Ribberink waves. Subsequently it is to be investigated if the celerity of the Ribberink wave is in reality higher than the celerity of the De Vries wave. This is important since the explanation of this phenomenon in the first place brings us a step forward in the understanding of the sorting of sediment in general, but also can have implications for the implementation of Hirano's sediment conservation model in numerical models. This can make model predictions more accurate.

1.4 Research questions

To fulfil this objective the below research questions are formulated:

1. What is the behaviour of a river bed with mixed-size (bimodal) sediment in a physical, controlled environment (flume experiment), regarding De Vries and Ribberink wave propagation?

2. How do the behaviour and celerities of the De Vries and Ribberink wave in the flume experiment compare to predicted celerities?

3. What is the behaviour gives the Hirano model, regarding the Ribberink wave and De Vries wave, if we avoid/dismiss grain-size-selective processes (i.e. in a tracer experiment)?

1.5 Methodology

The investigation of this MSc thesis consists of the following parts:

1.5.1 Flume experiments

Experiments are carried out in the tilting flume in the water laboratory of the Civil Engineering and Geosciences faculty, Delft University of Technology. Two separate cases were studied:

1. An experiment with bimodal sediment. A coarse fraction is installed from the upstream boundary, somewhat higher than the bed level more downstream. The bed downstream consists of a mixture of both sediment fractions.

2. A tracer experiment in which uniform sediment is used. The "coarse" fraction is tracked through colour labelling. In this way the complexities resulting from sorting due to grain-size-selective transport are eliminated. By numerically reproducing the experiment and comparing the results with the result of the laboratory experiment, insight in the question can be given if the Ribberink wave travelling faster than the De Vries wave is an artefact of the Hirano model or that it has physical meaning and relevance.

The detailed design of the experiments and all relevant issues are elaborated in Chapter 3.

1.5.2 Numerical model tests of flume experiments

To compare the results of the flume experiments with predicted values, the flume tests are simulated with a numerical model. Ribberink wave and De Vries wave celerities are found and compared with those measured in the lab experiments.

2 | Literature review

This chapter reviews the research done over the past years on the behaviour of mixed-size sediment transport, in particular regarding waves arising due to grain-size-selective transport. Sorting processes and the associated waves are studied analytically (mathematical review) and in a physical environment (experiments). The last section describes the theory of the propagation of a shoal with non-uniform sediment as will be installed in the flume experiments conducted in this research.

2.1 Mathematical review

Part of this section has been published in a slightly different form in Berkhout (2014).

2.1.1 System of governing equations

The system of differential equations considered below is a mathematical description of a one-dimensional hydrostatic unsteady free-surface water flow over a cohesion-less bottom composed of mixed-size sediment. The mathematical model is composed of a set of governing equations expressing physical principles, i.e. conservation of water and sediment mass and the momentum principle.

Hydrodynamic model
In this one-dimensional, non-linear system of partial differential equations the water motion is described by the Saint-Venant equations, consisting of the equation for conservation of water mass, the continuity equation:

$$\frac{\partial h}{\partial t} + \frac{\partial q}{\partial x} = 0, \tag{2.1}$$

and the momentum balance:

$$\frac{\partial q}{\partial t} + \frac{\partial}{\partial x}\left(\frac{q^2}{h} + \frac{1}{2}gh^2\right) + gh\frac{\partial \eta}{\partial x} + \frac{u|u|}{C^2} = 0, \tag{2.2}$$

in which h $[m]$ is the flow depth, q is the water discharge per unit width $[m^2 s^{-1}]$, $g = 9.81 m s^{-2}$ the acceleration due to gravity, η the bed elevation $[m]$ and C the dimensionless Chézy coefficient. The mean flow velocity u is defined as $u = qh^{-1}$.

Sediment continuity model
The Exner equation for the total sediment mass balance is given by:

$$(1-\varepsilon)\frac{\partial \eta}{\partial t} + \frac{\partial q_b}{\partial x} = 0, \tag{2.3}$$

with ε is the porosity, η is the bed elevation as defined in Figure 2.1 and q_b is the total sediment discharge per unit width $[m^2 s^{-1}]$. The latter is determined using a sediment transport model, e.g. by Meyer-Peter and Müller (1948).

To account for sediment sorting processes, Hirano (1971, 1972) developed a sediment continuity model for mixed sediment in which he divided the bed into an active layer and a substrate layer (Figure 2.1). The active layer is the part of the bed that interacts with the flow and is therefore affected by aggradation and degradation. The active layer is a layer with thickness L_a and is located immediately under the bed surface. The sediment is considered to consist of N sediment fractions with k the index ranging from 1 to N corresponding to a grain diameter d_{sk}. The active layer is assumed to be vertically mixed. The vertically-averaged volume fraction content of size fraction k of the active layer is denoted with F_{ak}. The non-vertically mixed fraction content of the substrate is denoted as f_{sk}. The volume fraction contents of both layers are defined as follows:

$$\sum_{k=1}^{N} F_{ak} = 1, \quad \sum_{k=1}^{N} f_{sk} = 1 \tag{2.4}$$

At the interface between the active and substrate layer, a vertical flux of sediment mass exchanges sediment between the two layers under conditions of aggradation or degradation. The volume fraction content at the interface is denoted as f_k^I. The general continuity equation for sediment in the active layer, for a sediment fraction k (Hirano, 1971, 1972):

$$(1-\varepsilon)\left[\frac{\partial F_{ak} L_a}{\partial t} + f_k^I \frac{\partial(\eta - L_a)}{\partial t}\right] + \frac{\partial q_{bk}}{\partial x} = 0 \tag{2.5}$$

in which q_{bk} $[m^2 s^{-1}]$ is the specific sediment discharge of size fraction k given by:

$$q_{bk} = F_{ak} Q_{bk} \tag{2.6}$$

where Q_{bk} is the transport capacity of each size .fraction for the given hydrodynamic conditions, to be evaluated using a bed-load transport model

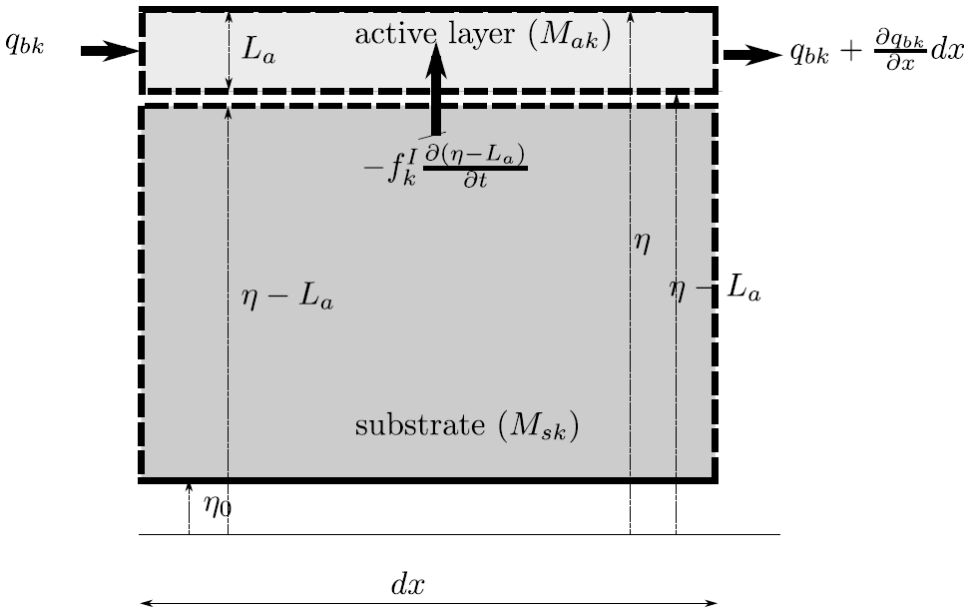

Figure 2.1: Schematization of the active layer model by Hirano. Figure by Stecca et al. (2014)

2.1.2 Analytical eigenvalue approximations to the system of governing equations

The analytical eigenvalue approximations of the system of governing equations (Equations 2.1 to 2.3 and Equation 2.5) can be seen as the celerities of the waves described by the system, provided full mobility of all fractions. These waves are of small amplitude.

It should be noted that the analytical eigenvalue apporximations to the system of governing equations are linear and are inviscid, i.e. the frictional source terms in the momentum equation are neglected. This implies that the solutions only apply to waves that develop and propagate over short time and length scales.

When considering a unisize-sediment case, where $N = 1$, the system reduces to the Saint-Venant-Exner model. This system of equations has been analysed by De Vries (1965) and Lyn and Altinakar (2002), among others. De Vries (1965) found for the approximations to the eigenvalues of the system:

$$\lambda^*_{1,2} = 1 \pm \frac{1}{Fr}, \quad \lambda^*_3 = \frac{\psi}{1 - Fr^2}, \tag{2.7}$$

where $\lambda_i^* = \lambda_i/u$ $(i = 1, 2, 3)$ represent the dimensionless eigenvalues. Fr is the Froude number and ψ represents the variation in total bed load discharge per unit variation in water discharge:

$$Fr = \frac{u}{\sqrt{gh}}, \quad \psi = \frac{\partial q_b}{\partial q} \tag{2.8}$$

The approximation is valid under well developed super or subcritical flow, $Fr < 0.8$ and $Fr > 1.2$ (Stecca et al., 2014). In his quasi-steady analysis De Vries (1965) shows the physical representation of the characteristic celerity λ_3^* to be the celerity of bed perturbations, i.e. the celerity of the associated De Vries wave (c_{bed}). When the celerity is positive the wave travels in downstream direction under subcritical flow. Under supercritical flow the wave propagates in upstream direction. $\lambda_{1,2}^*$ are the celerities of the fixed-bed shallow water model (Saint-Venant model), waves of flow characteristics (Lyn and Altinakar, 2002).

Ribberink (1987) conducted a one-dimensional mathematical analysis of the characteristics of the governing system of partial differential equations considering multiple fractions. For simplification he assumed the following:

1. The N number of fractions are represented by one average grain diameter $\overline{d_s} = \sum_{k=1}^{N} F_{ak} d_{sk}$
2. Quasi-steady flow
3. The total sediment discharge is only depending on mean sediment diameter and water velocity
4. The bed load grain size distribution is equal to that at the interface between the substrate and active layer, in aggradational conditions $(\partial(\eta - L_a)/\partial t > 0)$

His analysis of the system results, together with the above mentioned eigenvalues $\lambda_{1,2}^*$ of Equation 2.7, in the following approximations:

$$\lambda_3^* = \frac{\psi}{1 - Fr^2}, \quad \lambda_4^* = \frac{q_b}{uL_a}. \tag{2.9}$$

Here λ_3^* again represents the De Vries wave celerity. Here, λ_4^* represents the celerity of perturbations in the average diameter of the mixture, i.e. perturbations in the grain size distribution in the active layer. In Section 1.1 this already has been defined as the Ribberink wave celerity. Equation 2.9 shows that the celerity of the perturbation in grain size distribution is inversely proportional to the active layer thickness: a thinner active layer gives rise to higher Ribberink wave celerities.

Mosselman and Sloff (2007) performed the analysis again, expressing the celerities in terms of the average sediment grain size, taking also into account

the difference in mean diameter between bed load and active layer material. In dimensional form $[ms^{-1}]$:

$$c_{bed} = \frac{bq_b}{(1-\varepsilon)(1-Fr^2)h}, \quad c_{mix} = \frac{\overline{d_{sT}}q_b}{\overline{d_s}L_a(1-\varepsilon)}, \tag{2.10}$$

with,

$$\overline{d_s} = \sum_{k=1}^{N} F_{ak}d_{sk}, \quad \overline{d_{sT}} = \sum_{k=1}^{N} F_{Tk}d_{sk}, \tag{2.11}$$

in which b is the degree of non-linearity of q_b defined as $b = (u/q_b)(dq_b/du)$, F_{Tk} is the relative occurrence of sediment size fraction k in the bed load, $\overline{d_s}$ an average grain size of sediment mixture in the active layer $[m]$, $\overline{d_{sT}}$ the average grain size of the bed load $[m]$.

Mosselman and Sloff (2007) defined c_{bed} as: '...the celerity of a kinematic bed topography wave forced by gradients in bed load transport capacity', which can be interpreted as a bed elevation wave and c_{mix} as: 'the celerity of a kinematic wave of grain size distribution of the bed forced by bed level changes and a difference between the grain size distributions of the bedload and the bed.'

Both Ribberink (1987) and Sloff and Mosselman (2012) analysed the ratio of celerities of De Vries and Ribberink wave and found a ratio of λ_3^* to λ_4^* to be around 0.3–4 (Ribberink, 1987) and 2–8 (Sloff and Mosselman, 2012). This shows an at least as high or possibly higher celerity for the Ribberink wave than for the De Vries wave.

Stecca et al. (2014) list the following three limitations to the approximations of Ribberink (1987) and Mosselman and Sloff (2007): *' 1) due to the quasi-steady flow assumption, they do not apply to transcritical conditions; 2) they only include a single, representative celerity for the evolution of the average diameter, i.e. c_{mix}, rather than distinct celerities due to various size fractions; and 3) being developed in aggradational conditions, they can be applied to degradation only if the top of the substrate layer has the same grain size distribution as the active layer, as is done by Mosselman et al. (2008). '*

Suzuki (1976) performed, instead of the previous case, a characteristics analysis of the system with retaining independent active layer equations for áll the fractions. His approximation only applies to well-developed sub and supercritical regimes since he assumed quasi-steady flow. The celerities of the distinct Ribberink waves are:

$$\lambda_{3+k}^* = \frac{Q_{bk} + F_{ak}\frac{\partial Q_{bk}}{\partial F_{ak}}}{uL_a} \tag{2.12}$$

Sieben (1997) performed a fully unsteady analysis of the Saint-Venant-Hirano model, under any Froude regime, for a case of two sediment fractions ($N = 2$). His analysis also resulted in an expression for the Ribberink wave, which is positive throughout the Froude domain. However, it is important to remark that Sieben (1997) did not found a closed-form expression for the characteristic celerities of the Saint-Venant-Hirano model, but that he only provides a graphical representation of the characteristic celerities for various values of the active layer thickness.

Stecca et al. (2014) extended the analysis of Ribberink (1987) of the Saint-Venant-Hirano model by including full unsteadiness and grain size selectivity of the transported load. This was done by explicitly considering multiple sediment fractions. This resulted in characteristic relations for the distinct waves $\lambda^*_{1,2}$ and λ^*_3, together with analytical approximations of celerities of the Ribberink waves per fraction under any Froude regime:

$$\lambda^*_{3+k} = \frac{Q_{bk}(1 - f^I_k) + f^I_k Q_{bN}}{uL_a} \qquad \text{for } 1 \leq k \leq N - 1 \tag{2.13}$$

Stecca et al. (2014) found that:

> *'...initial gradients in the grain size distribution of the active layer are able to trigger significant bed variations, which propagate in the downstream direction at faster pace than the 'bed' wave (De Vries wave, BB) arising from the unisize-sediment Saint-Venant-Exner model. We also verify that multiple 'sorting' waves (Ribberink waves, BB) carry multiple associated bed perturbations, travelling at different speeds.'*

Although the Ribberink wave and De Vries wave are here described as distinct waves with celerities, they both interact and influence each other. Changes in grain size distribution trigger bed level changes and vice versa. The streamwise sorting process is affected by perturbations in the bed as well as by the perturbations in the grain size distribution of the bed, which are both propagating through the domain. The terms Ribberink wave and De Vries wave serve as useful terms, named after the persons to first describe the waves (Ribberink, 1987; De Vries, 1965), to distinct between the waves carrying perturbation information of solely the bed or grain size distribution change and the actual change in bed level and grain size distribution which are governed by contributions from in principle all waves.

2.2 Review of experiments

2.2.1 Suzuki (1976)

Suzuki (1976) studied the system of differential equations describing the

transport of non-uniform sediment to obtain the characteristic relations of the system. In order to verify the expressions he found for the De Vries wave celerity and Ribberink wave celerity (Equation 2.12), he conducted a series of flume experiments in which both uniform and non-uniform sand was used.

The experiments provide valuable information on the physical propagation speed of Ribberink waves.

Experimental set-up

Figure 2.2 shows the set-up of the flume experiments conducted by Suzuki (1976). We only consider the non-uniform sediment flume experiments, as only in these experiments sorting was present. The experimental details are listed in Table 2.1 and Table 2.2.

In Experiment 2 the bed consisted of the coarse sediment a. The input sediment is largely coarse (75 % of sediment type a) but mixed with the finer sediment (25 % of sediment type b). In this case the propagation of the finer sediment b through the domain in was measured. In Experiment 4 this is the other way around. The bed consisted of finer material b. A mixture of 25% of sediment a and 75 % of sediment b was fed. The propagation of sediment a through the domain was measured.

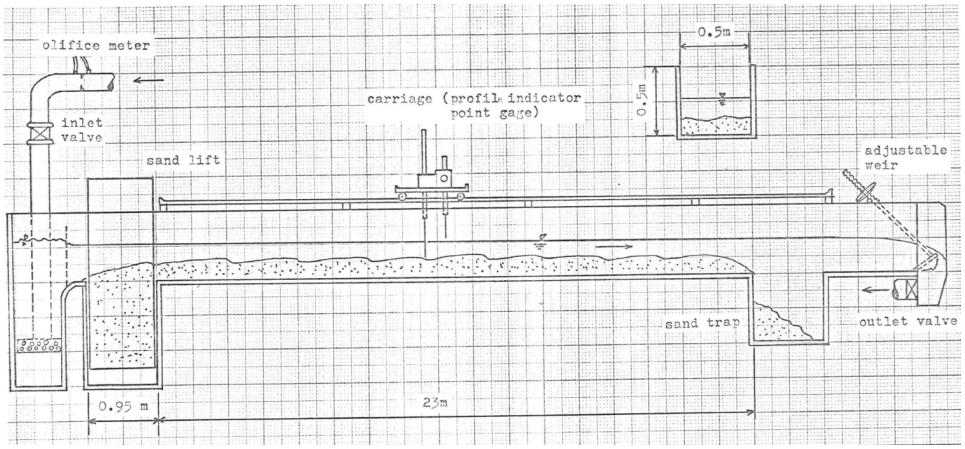

Figure 2.2: Side view of set-up for the flume experiments conducted by Suzuki (1976). Figure from Suzuki (1976).

To obtain the celerities of the bed perturbations the bed level was measured at certain time intervals. For the celerities of the Ribberink waves samples of the bed were taken at certain time intervals by stopping the flow and keeping the water depth larger than the original flow depth. Stopping and restarting the flow influences the experiment negatively since during stopping and starting different flow conditions are present. The flow depth during the sampling was kept higher than the original flow depth to keep

Table 2.1: Experimental details of the flume experiments conducted by Suzuki (1976)

Experiment		Coarse feed **2**	Fine feed **4**
Water discharge	$[m^3 s^{-1}]$	0,045	
Slope	$[-]$	0,0011	0,0010
Total input sed discharge	$[m^3 s^{-1}]$	4.9E-6	
Water depth	$[m]$	0,19	0,20
Flow velocity	$[ms^{-1}]$	0,47	0,45
Froude number	$[-]$	0,34	0,32
Dune height	$[m]$	0,040	0,055

Table 2.2: Sediment composition of the bed sediment and input sediment according to the fraction P of sediment types a and b. Characteristics of sediment types a and b are given in Figure 2.3.

Bed	***2***	***4***
P_a	1	0
P_b	0	1
Input		
P_a	0,75	0,25
P_b	0,25	0,75

flow velocities low and minimize negative effects of changing flow conditions. The top layer of the bed was removed at certain locations in the longitudinal cross-section and the sample obtained was analysed through sieving to determine the relative amount of one of the two sediment fractions. The sample was taken to a depth representative of the full active layer, which was defined as half the dune height. The locations where the sampling took place were at the whole area of the upstream side of the dunes. After the analysis, the samples were placed back in their position on the bed.

Experimental results

Samples of the grain size distribution of the bed during the experiments result gave information on distribution of the fed sediment over the length of the flume. An x-t diagram can be constructed, showing the displacement of the Ribberink wave in space over time. The result is shown in Figure 2.4. It is clear that the wave of fine sediment in a coarse domain moves faster through the domain than the coarser sediment through a fine domain.

Table 2.3 shows the analytical celerities by Ribberink (1987) (Equation 2.9) and Stecca et al. (2014) (Equation 2.13) for the De Vries wave and Ribberink wave for the experimental case of Suzuki (1976) together with

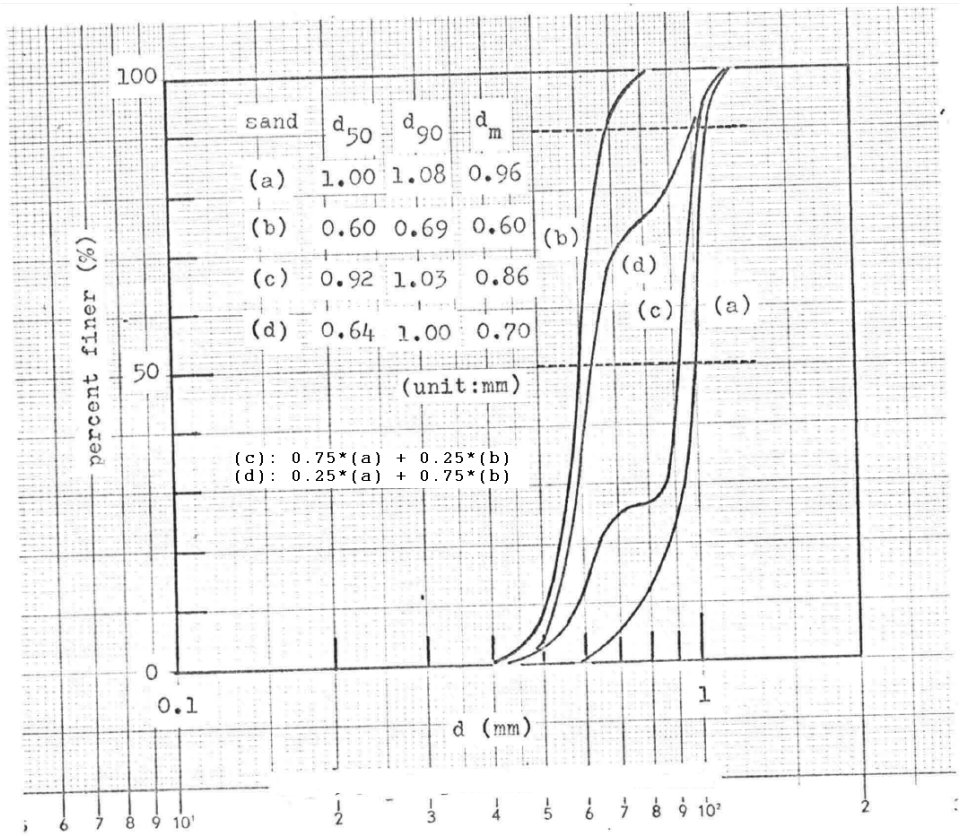

Figure 2.3: Grain size distribution of sediment used in the experiments by Suzuki (1976). The sediment mixtures c and d are a combination of sediment mixtures a and b. Figure from Suzuki (1976).

the values of the Ribberink wave celerity from the experimental data of Suzuki (1976). The latter ones are obtained by taking the centroid of the distribution of the sediment type originally not in the bed and the front of that distribution. For the experiments where the perturbation in the bed grain size distribution was measured, Suzuki (1976) does not provide any data on De Vries wave celerities.

Regarding experiment 2, the Ribberink wave celerities as calculated from the linearised approximations are both faster than the Ribberink wave celerities from the experiment, for the front (about 2 times as fast) as well as the centroid celerity (4 times as fast). The analytical De Vries wave is several times slower than the analytical Ribberink wave. Regarding experiment 4, the analytical celerities of the Ribberink waves are larger than the celerity of the Ribberink wave from the experiment. Also the analytical De Vries wave celerity is lower than the analytical Ribberink wave celerity. Comparing the results of experiment 2 and 4, it shows that the analytical Ribberink wave celerity of Stecca et al. (2014) is higher in experiment 2 than in experiment

4, but for the celerity as calculated with the linearised approximation by Ribberink (1987) this is the other way around.

Table 2.3: Analytical celerities by Ribberink (1987) (Equation 2.9) and Stecca et al. (2014) (Equation 2.13) compared with the experimental data of Suzuki (1976) for the De Vries waves and Ribberink waves. Units in $[ms^{-1}]$. **N.B.**: Suzuki (1976) provides no data on the De Vries waves in experiment 2 and 4. He did perform experiments with a disturbance in bed height but with different grain size distribution of bed and input sediment.

		Experiment			
		2		4	
		DV wave	Rib. wave	DV wave	Rib. wave
Analytical	Ribberink	1.79E-04	5.38E-04	1.43E-04	5.68E-04
	Stecca et al.	1.79E-04	6.56E-04	1.43E-04	4.64E-04
Experimental	Suzuki (front)		3.44E-04		2.04E-04
	Suzuki (centroid)		1.47E-04		1.34E-04

2.2.2 Ribberink (1987)

Ribberink (1987) performed a series of flume experiments to verify his mathematical analysis of the system of partial differential equations (PDEs) regarding the eigenvalue approximations (Section 2.1.2). His flume experiment E8-E9 provides information which gives insight in the behaviour of morphological changes with mixed-size sediment in a physical environment.

The experiment was carried out in a flume of 30 meters length. The sediment mixture was a combination of two sediment fractions, $d_1 = 0.78\ mm, d_2 = 1.29\ mm$. After the reaching an equilibrium situation, the experiment was started. During the experiment the grain size distribution of the input sediment load was gradually coarsened, keeping the input rate constant.

Figure 2.5 shows the experimental results regarding the grain size distribution of the active layer at several moments in time from 5 to 50 hours after the start of the experiment. The figure shows clearly the coarsening of the bed over time.

Figure 2.6 shows the measured bed level at different positions along the flume length. Both a sedimentation wave and an erosion wave (Ribberink wave) are present, the latter preceding the former. The erosion increases over the length of the flume.

In two separate studies the experiment E8-E9 by Ribberink (1987) are numerically reproduced. First, by Blom (2008) three mixed sediment continuity models were tested along with the sediment continuity model for non-uniform sediment by Hirano for this experiment. Stecca et al. (submitted) provides the experimental outcomes of experiment E8-E9 combined with the results of a numerical reproduction of the experiment to verify

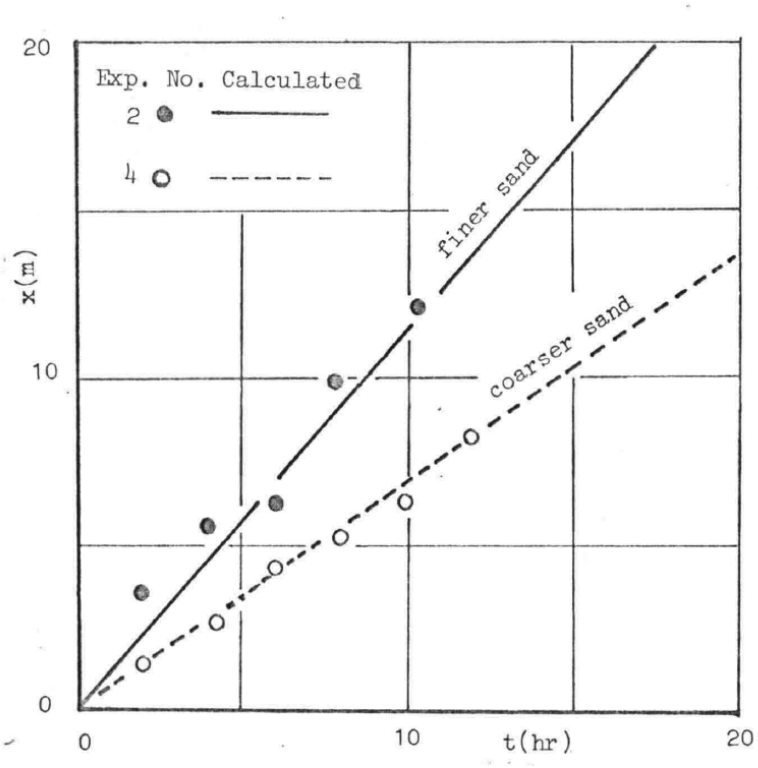

Figure 2.4: x-t diagram of the displacement of the distribution of the sediment type originally not in the bed over the longitudinal direction of the flume, representing the displacement of the Ribberink wave. The celerity of the Ribberink wave in the experiment with a coarser sediment feed is slower. The calculated lines are based on Equation 2.12. Figure from Suzuki (1976).

outcomes of the model they developed.

2.2.3 Iffezheim field experiment (Gölz et al., 2006)

In a long-term field experiment carried out in the river Rhine at Iffezheim, tracer sediment, 28,000 tons of broken granite, has been dumped into the river between river-km 336.2 and 337.1 and monitored for a period of 60 months (Gölz, 2002; Gölz et al., 2006). The sediment consisted of five different fractions ranging from $4 - 63\ mm$. The grain size distribution of the dumped tracer material was similar to the grain size distribution of the gravel dumped in the past few years.

The distribution of tracer material was monitored at 2, 6, 12, 24, 36 and 60 months. Samples of the river bed were analysed regarding the percentage of tracer sediment. The samples were taken from river-km 336,3 where the material was dumped until river-km 402,6. In every sampling campaign, samples where taken at 9 to 13 locations over the length, taking per location

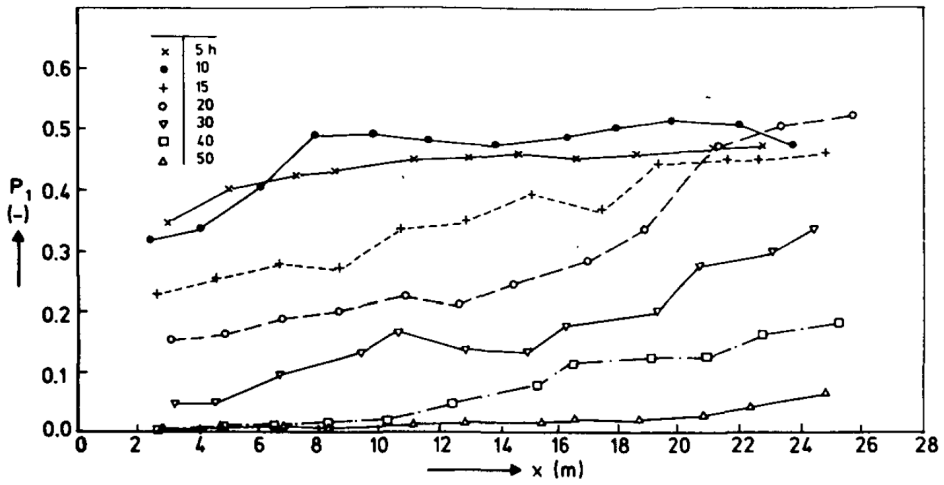

Figure 2.5: Grain size distribution of the bed from over the length of the flume for several moments in time of experiment E8-E9 from Ribberink (1987). p_1 is the probability of size fraction d_1 in the sediment mixture in the active layer. Figure from Ribberink (1987).

5 samples over the cross-section. The data was gathered with the diving-bell vessel 'Carl Straat'.

Figure 2.7 shows the hydrograph over the period of sampling including the moments at which the samples were taken. In the year 1999 a larger flood is visible. Additional information on the morphological characteristics of the Rhine downstream of Iffezheim can be found in Weichert et al. (2010).

Results

We plot the concentration of the tracer material per fraction along the longitudinal direction of the river in Figure 2.8. More tracer concentration profiles are shown in Appendix A. Figure 2.9 is constructed by finding the river-km locations of each centroid (mass mean) of the distributions of tracer material and plotting them against the moment when the sample is taken. The average propagation celerities of the different fractions are listed in Table 2.4. This table presents, apart from the propagation celerities of the centroid of the distribution, also the celerities of the front of the distributions.

Figure 2.9 and Table 2.4 shows that the finer fractions travel faster than the coarser fractions. However the fraction of $8 - 16$ mm is slightly faster than the finest fraction $4 - 8$ mm. This may be explained by hiding effects, meaning that the finer grains 'hide' behind the larger grains, making the finer grains less and the larger grains more mobile compared to a situation with uniform sediment.

Appendix A.2 shows al the curves of the tracer sediment distribution over the river reach for all dates per fraction. These figures show the degree of

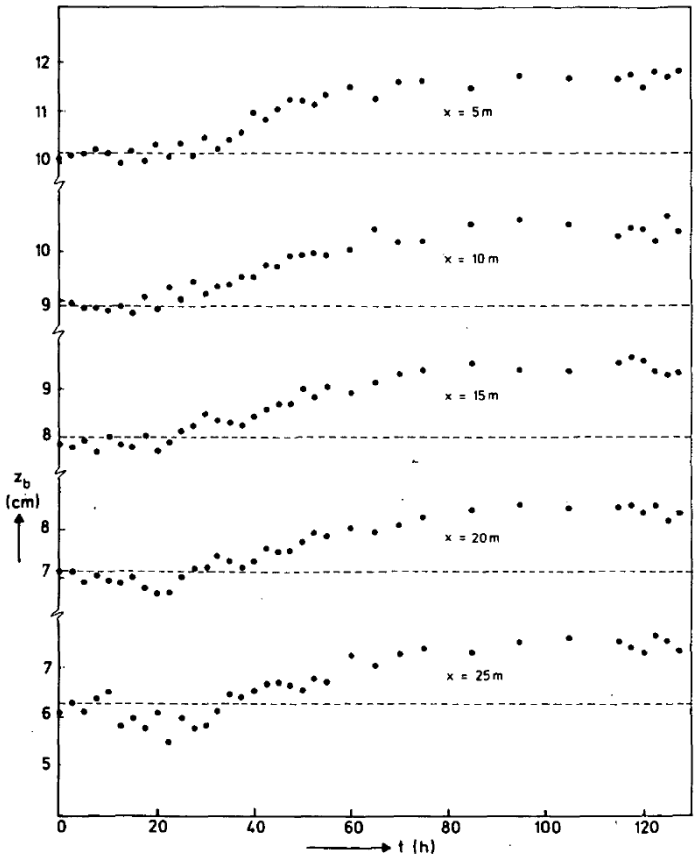

Figure 2.6: The average filtered bed level (z_b) over time at different locations along the length of the flume of experiment E8-E9. Figure from Ribberink (1987).

dispersion of the tracer during transport. It is worth mentioning that the tracer disperses over the reach over time, and migrates downstream.

2.3 Shoal propagation

This section describes the theory of the propagation of a shoal with non-uniform sediment as will be installed in the flume experiments conducted in this research.

2.3.1 The shoal and sediment transport

Figure 2.10 shows a shoal, or backward-facing step on the river bed, with bimodal sediment, where the shoal consists of coarser sediment than the bed $\overline{d}_{s,I} > \overline{d}_{s,II}$. A shoal is schematically visualised in this figure to explain the basic concepts about how a shoal behaves in a flow. Two parameters are paramount in the propagation of the shoal: the flow velocity u and the

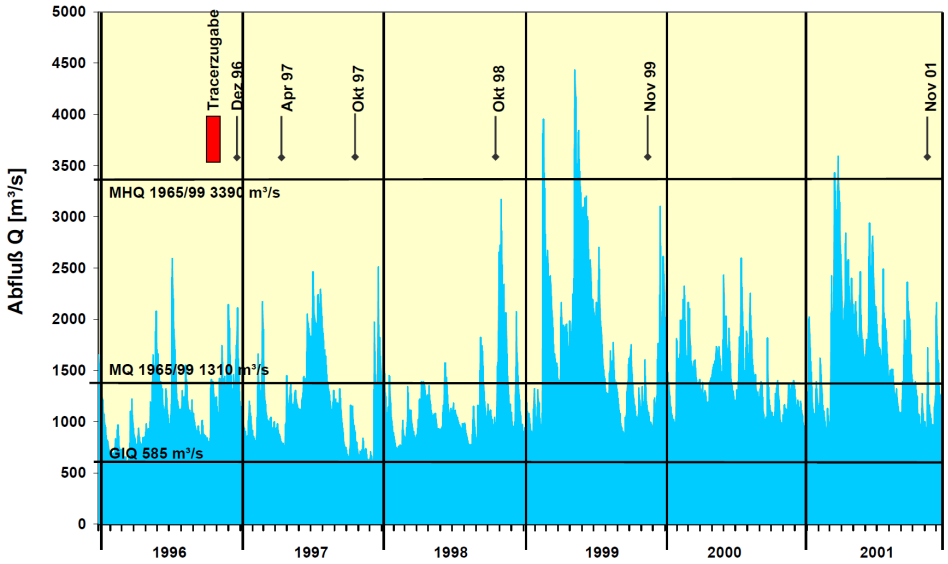

Figure 2.7: Hydrograph of the Rhine river near Iffezheim over the period of sampling. The moments at which the bed samples were taken are indicated at 2, 6, 12, 24, 36 and 60 months after the moment of dumping the tracer material. Figure from Gölz et al. (2006).

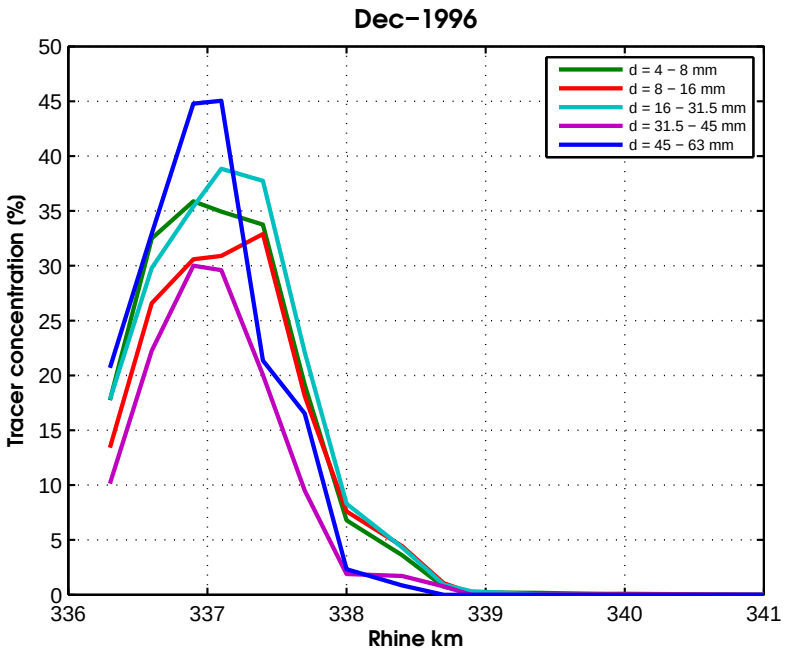

Figure 2.8: Distribution of all fractions over longitudinal direction.

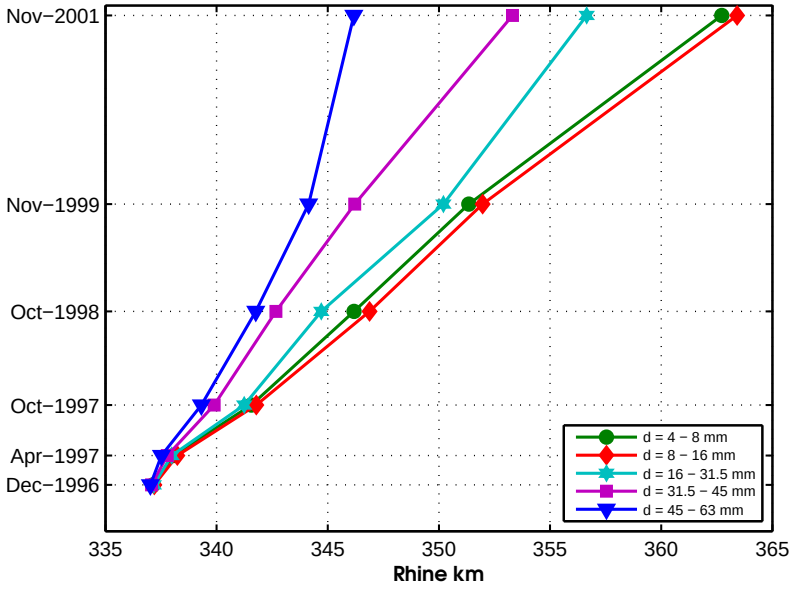

Figure 2.9: Displacement of the centroid of the distribution of a sediment fraction over the longitudinal distance in time, per sediment fraction. Summary of data from the Iffezheim tracer case obtained by Gölz et al. (2006). The finer material is transported faster than the coarser material.

average diameter of the sediment mixture $\overline{d}_s$. The flow velocity in cross-section I is larger than flow velocity in cross-section II, $u_I > u_{II}$. This effect alone results in a higher sediment transport capacity in cross-section I than in cross-section II: $q_{b,I} > q_{b,II}$.

Since the shoal consists of coarser material than the bed, $\overline{d}_{s,I} > \overline{d}_{s,II}$ which means that due to this effect alone, the sediment transport capacity in cross-section II is likely to be larger than in cross-section I, $q_{b,I} < q_{b,II}$. One of both effects is likely to be dominant in the determination of the shoal propagation characteristics.

Fennis (2013) and De Way (2014) both did a numerical study into the

Table 2.4: Mean celerities of the front and mass mean of the distributions of different fractions. These celerities represent the celerities of the waves of sediment fractions in km/y

		Sediment fraction $[mm]$				
Celerity	$[km/y]$	4 - 8	8 -16	16 - 31.5	31.5 - 45	45 - 63
Mass mean		4.95	5.14	4.11	3.19	2.14
Front		12.92	12.04	10.06	6.11	2.59

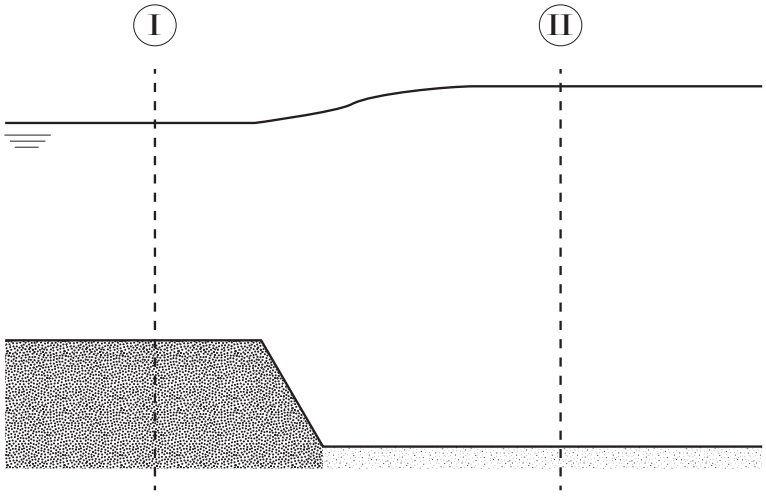

Figure 2.10: Schematization of a shoal on the river bed, with bimodal sediment, where the shoal consists of coarser sediment than the downstream bed. Two parameters are paramount in this case for the propagation of the shoal in downstream direction: the flow velocity u $[ms^{-1}]$ and the average diameter of the sediment mixture $\overline{d_s}$ $[m]$. They both influence the sediment transport q_b. One of them is dominant in the determination of shoal propagation characteristics.

propagation of a shoal on the river bed. They described among other things the effect of the flow on the propagation of the shoal and on the change of bed grain size distribution resulting from mixed sediment transport. They both distinguished two situations with different effects: one with a 'high' and one with a 'low' discharge.

1. 'Low discharge': In the case of a relative low discharge, the ratio of shoal height to flow depth is relatively large. The Bernoulli effect above the shoal is stronger than for the 'high discharge'. Considering the streamwise variation in sediment transport rate over the shoal, the increase in flow depth downstream of the shoal is dominant and leads to a streamwise decrease in the transport rate. This results in aggradation behind the shoal and thus migration of the shoal in downstream direction.

2. 'High discharge': In the case of a relative high discharge, the relative streamwise increase in flow depth is smaller than for the 'low discharge'. Now the effect of the streamwise increase in flow depth on the streamwise variation of the sediment transport capacity is compensated by the fact that the shoal is coarser than the reach just downstream of the shoal. In this case, the sediment transport capacity increases in downstream direction over the downstream end of the shoal. A scour hole or trough downstream of the shoal is formed. This scour hole will

smooth out over time since the sediment transport gradient becomes less steep. Shoal and scour hole propagate in downstream direction with potentially different migration celerities. Because the sediment transport rate for finer sediment is higher than of coarser sediment with the same flow characteristics the trough contains a higher volume fraction of coarse sediment. The propagation of the trough can be seen as a propagation of the coarser fraction, thus a Ribberink wave travelling in downstream direction.

2.3.2 Turbulent flow structure behind shoal

Figure 2.11 shows the flow structure downstream of a shoal-like backward-facing step. Because of the abrupt increase of flow depth, flow separation occurs, creating a recirculation zone downstream of the backward-facing step. This recirculation zone changes the local flow condition, therefore having influence on the local sediment transport. According to Bradshaw and Wong (1972) the reattachment point of this recirculation zone is $O(10h)$ downstream of the front of the shoal. At this point of reattachment, the flow is highly turbulent, creating what is called 'turbulent bursts'. Brodkey et al. (1974) defines turbulent bursts as '[a] *sequence of events consisting of the lifting of low-speed fluid, oscillatory growth and breakup*' in which '*higher momentum fluid moving towards the wall* [*bed*, BB] *(sweep-type event) and the lower momentum fluid moving outwards from the wall (ejection-type event)*' combined give shear stresses acting on the bed sediment '*exceeding 100% of the stress over the whole wall region*'.

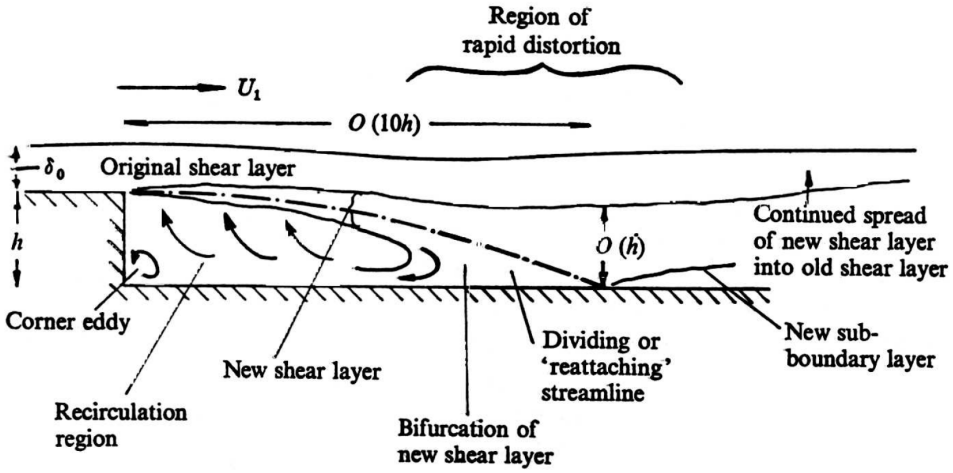

Figure 2.11: Flow structure downstream of backward-facing step – having the same characteristics as our shoal (from Bradshaw and Wong, 1972, Fig 2, p. 116)

2.4 Conclusions

From Section 2.1.2 it can be concluded that the mathematical system describing mixed sediment transport, the Saint-Venant-Hirano model, is thoroughly analysed regarding the waves arising in the system and are described by the eigenvalues of the system. From this we have a well understanding of how the theoretical waves behave and what parameters influence them. Since the solutions are linearised and inviscid, the question arises how well the eigenvalue approximations describe reality.

The analysis of the experiments conducted by Suzuki (1976) shows that the analytical values for the celerities of the Ribberink and De Vries waves is about 2 to 4 times as large as the measured celerities. Also for both experiments the analytical Ribberink wave is faster than the De Vries. The question rises if this would also be the case in reality. Or more general: is the behaviour of the analytical waves an indication for the behaviour of the real life waves?

The field test in the Rhine river near Iffezheim (Section 2.2.3) illustrates how different fractions of sediment are transported with different celerities through the river reach. Also the dispersive character is visible. This data from reality follows the observations from the mathematical analysis, i.e. waves of different grain size travel with different celerities, the coarser slower than the finer fractions. Unfortunately, the Iffezheim case does not provide information on bed levels. Therefore the celerities of bed level disturbances could not be compared to analytical values and with the celerities of the waves of sediment fractions.

From this it follows that additional tests with mixed-size sediment are needed in which a clear bed disturbance travels through the domain. In such a study also the influence of bed perturbations on the sorting process can be studied.

3 | Set-up of laboratory experiments

3.1 Experimental scheme

The flume experiments are conducted in the flume of the Water Lab of the Faculty of Civil Engineering and Geosciences at Delft University of Technology. Two experiments are performed: E1, a tracer experiment in which uniform sediment is used, with only the shoal part painted and E2 an experiment with a bimodal sediment mixture, with the coarsest fraction is painted in a different colour[1]:

E1 A tracer experiment with uniform sediment. In this way the complexities of sediment sorting are eliminated. The tracer fraction is tracked through colour. The initial bed consists of only the tracer fraction from the upstream end of the flume over 4 m length in downstream direction. The bed surface elevation of the tracer reach is 3 cm higher than the downstream part of the flume. By numerically reproducing the experiment and comparing the results with the result of the laboratory experiment, the question can be answered if the Ribberink wave is an artefact of the Hirano model or that it has a physical reason for originating.

E2 An experiment with bimodal sediment. The initial bed consists of only the coarser fraction from the upstream end of the flume over 4 m length in downstream direction. The bed surface elevation of the coarse reach is 3 cm higher than the downstream part of the flume (Figure 3.2). Downstream the bed consists of a mixture of coarse and fine sediment (30% and 70% respectively).

[1]Berkhout (2014) did a numerical study into the behaviour of Ribberink waves and concluded that for a thorough investigation of the physical behaviour of Ribberink waves a series of three experiments would be needed. A tracer experiment and two experiments with a bimodal sediment mixture but different flow conditions (Froude number). During preliminary checks in the flume, it became clear that the experiment with a relatively higher Froude number would induce flow velocities too high to preform the measurement correctly. Therefore the following two flume experiments were conducted in the end.

3.2 Experimental set-up

The flume used in this research is a tilting flume with a constant, rectangular cross-section, dimensions and characteristics listed in Table 3.1 and is shown in Figure 3.1. The flume has a length of 14 meters but the area effectively measured is a bit over 10 meters.

Table 3.1: Dimensions and characteristics of the tilting flume of the Water Lab.

Feature	**Value**	
Length	14.0	$[m]$
Width	0.4	$[m]$
Height	0.45	$[m]$
Slope (max.)	0.04	$[-]$
Discharge (max.)	0.088	$[m^3 s^{-1}]$

Figure 3.1: Picture of the tilting flume of the Water Lab of the Faculty of Civil Engineering and Geosciences of Delft University of Technology. The upstream side is at the right hand side.

3.2.1 Initial conditions

In both experiments the same geometrical set-up is used: a shoal is build from the upstream boundary of the flume, extending four meters in downstream direction ending in a mild slope (see Figure 3.2). The upstream part of the shoal has a mild slope to force the flow gently over the shoal and bed without creating too much turbulence. A plastic sheet is placed on top of this slope to avoid local erosion. The bed downstream of the shoal has a thickness of 0.1 m. Table 3.2 lists the dimensions of bed and shoal and the sediment grain size distribution of both. The characteristics of the types of sediment used can be found in Section 3.3.

3.2.2 Boundary conditions

At the upstream boundary three boundary conditions will need to be imposed: one hydraulic boundary condition and two conditions for the sedi-

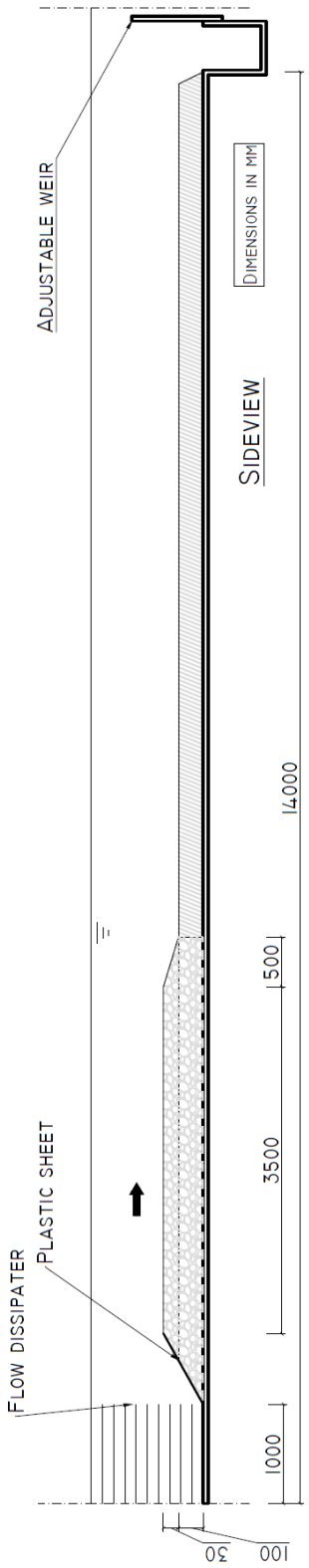

Figure 3.2: Drawing of experimental set-up. In experiment E1 both shoal and bed are of 100% coarse material, with the shoal sediment painted blue. In experiment E2 the shoal consists of 100% coarse material and the bed of 30% coarse and 70% fine. Flow is from left to right.

Table 3.2: Dimensions and composition of bed and shoal for both the mixed size and tracer experiment. The shoal thickness is the height of the shoal above the bed. F_{a1}, F_{a2a} and F_{a2b} are respectively the volume fraction contents of the fine, painted coarse and unpainted coarse sediment fraction (see Section 3.3).

		Tracer (E1)		**Mixed (E2)**	
Shoal thickness	$[m]$	0.03			
Shoal length		4			
Bed thickness		0.1			
		Bed	Shoal	Bed	Shoal
Fa1	$[-]$	0	0	0.7	0
Fa2a (painted)		0	1	0.3	1
Fa2b (unpainted)		1	0	0	0

ment transport. The hydraulic boundary condition is the discharge.

The sediment feed from the upstream boundary for both fractions (hence two boundary conditions) are set to be zero, following Berkhout (2014). This is done to prohibit difficulties regarding feeding the equilibrium sediment discharge, as it is hard to estimate. Thereby, a lack of incoming sediment initiates an erosion hole at the upstream end of the domain but does not significantly influence the propagation of the shoal.

At the downstream boundary, a constant water level is set, keeping the flow depth as similar as possible to the equilibrium flow depth to minimise backwater effects. As bed level will changes, flow depth changes but the resulting backwater effect is thought to be negligible since bed level changes are not severe at the downstream end of the domain.

An overview of the boundary conditions is given in Table 3.3.

Table 3.3: Boundary conditions of the flume experiments. All variables in this table are kept constant during the experiment.

			Tracer (E1)	**Mixed (E2)**
Upstream	Discharge	$[m^2 s^{-1}]$	0.1375	0.125
	Sediment discharge	$[m^2 s^{-1}]$	0	0
Downstream	Water level	$[m]$	0.36	0.32
	Slope	$[-]$	0.0013	

3.3 Sediment specifications

Figure 3.3 shows the grain size distribution of the sediment types used in the experiment, obtained by sieving. The sediment types are: the fine fraction (ranging from 0.7 mm – 1.4 mm) and the coarse fraction (ranging from

1.7 mm – 2.5 mm). Part of the coarse fraction is painted in order to observe the transport of coarse fraction through the domain with the method developed by Orrú et al. (2014), which will be described in Subsection 3.4.1. Figure 3.4 shows a picture of each of the three sediment types.

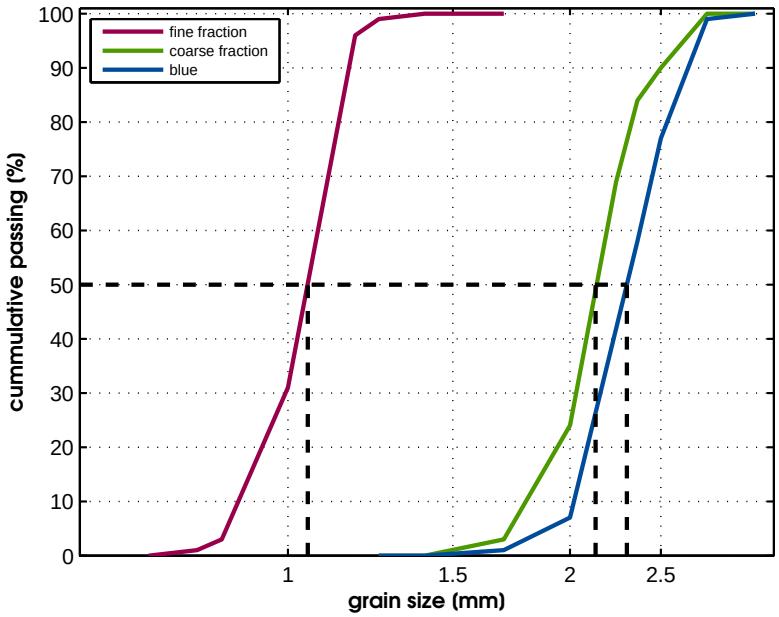

Figure 3.3: Grain size distribution of the sediment types used in the experiments. $d_{50,fine} = 1.05\ mm$, $d_{50,coarse,painted} = 2.30\ mm$ and $d_{50,coarse,unpainted} = 2.13\ mm$.

3.4 Measurements

The following parameters are measured during the experiments. The measuring methods are elaborated below:

- Grain size distribution of the bed surface
- Bed elevation
- Water level
- Downstream water level (base level)
- Water discharge
- Sediment discharge
- Grain size distribution of the sediment load

(a) Fine fraction, unpainted **(b)** Coarse fraction, painted **(c)** Coarse fraction, unpainted

Figure 3.4: Three types of sediment that are used in the flume experiments. The coarse fractions, painted (b) and natural colour (c) have the same grain size distribution (Figure 3.3).

3.4.1 Grain size distribution of the bed surface

Measuring method

Orrú et al. (2014) developed a measuring technique in which the grain size distribution of the bed surface can be determined by taking areal images of the bed surface, and analysing the images using a colour segmentation algorithm. To analyse the areal fraction content of each grain size the colours of the grain sizes need to be sufficiently distinct to allow for an optimal analysis of the photograph. From the image the areal fraction content, i.e. the relative presence of each size fraction over the bed surface, is determined.

The photographs are taken using 'a boat', Figure 3.5 , which is a glass plate with wooden edges of a certain height to allow the plate to be positioned just below the water surface, without being submerged. The glass plate prevents the reflection of light on the water surface and so guarantees accuracy of the analysis of the grain size distribution of the bed. The glass plate also facilitates the positioning of lights to light the bed. The boat is fixed on a carriage that runs on the rails of the flume but allowed to have free vertical motion (Figure 3.6).

To obtain a profile of grain size distribution over the length of the flume, the domain is divided into compartments of 28 *cm* length of which a photograph is taken. Figure 3.7 shows one of these photographs. These compart-

ments are separated by red stripes on the side of the flume. By analysing the position of the red stripes, the pictures can be cropped to fit the exact position (yellow dots in Figure 3.7). The cropped photographs are then divided into 10 area's of equal size in stream-wise direction, taking the middle one third of the width (hatched area in Figure 3.7). For each area the average areal fraction content is determined.

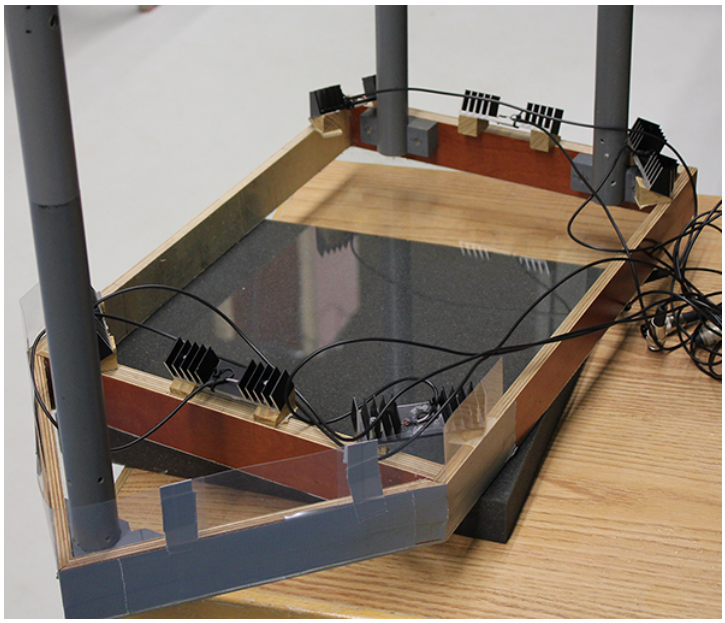

Figure 3.5: Boat with wooden edges and glass bottom to be used when taking the photographs to eliminate the water surface's reflection.

Areal to volume fraction content

Parker (1991a,b) (also see Orrú et al., 2014) provide Equation 3.1 to convert the areal volume fraction content to the volumetric fraction content:

$$F_{Vi} = \frac{F_{Ai}\sqrt{d_{si}}}{\sum_{k=1}^{N}(F_{Ak}\sqrt{d_{sk}})}, \tag{3.1}$$

where F_{Vi} denotes the volume fraction content of size fraction i in a sediment layer $[-]$, F_{Ai} is the areal fraction content of size fraction i of the same sediment layer $[-]$, and d_{si} is the grain size of size fraction i $[m]$. Like the index i, the index k denotes the size fraction.

3.4.2 Bed elevation and water level profiles

The bed and water level are both measured using a laser device, optoNCDT 1302 (MICRO-EPSILON), known as an intelligent laser optical displacement

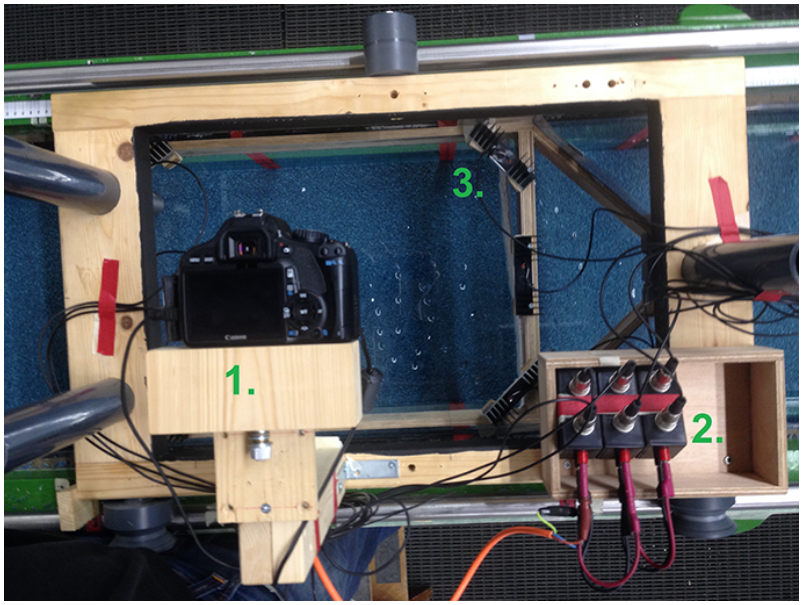

Figure 3.6: Carriage mounted on the rails of the flume to keep the glass plate (Figure 3.5) in a fixed position but allowing for vertical movement. The photo camera (1.) is fixed on the wooden frame of the carriage where also the cables (2.) run to provide power for the lights (3.) on the boat.

measurement[2]. The lasers for the bed and water level are mounted on a carriage that allows for taking profiles over the flume length (Figure 3.8).

Since the water level laser needs to reflect on the water surface, a piece of plastic sheet was kept floating on the water surface to let the laser reflect on. The bed level laser was mounted inside a watertight plastic box, so that is was possible to hold it underneath the water surface and let the laser beam reflect on the bed surface without having problems with the transition of the laser beam through different media.

3.4.3 Downstream water level (base level)

The downstream water level, or base level, is measured continuously during the experiment via a pitot tube (static pressure) connected to a device to measure the water level, a Temposonics® magnetostrictive linear position sensor (G-series). The water level meter is fitted in the grey tube shown in Figure 3.9

3.4.4 Water discharge

An ultrasonic flow meter (Proline Prosonic Flow 91W) on the inflow pipe is used to measure the flow discharge (Figure 3.10a). The digital display

[2]Instruction manual optoNCDT 1302

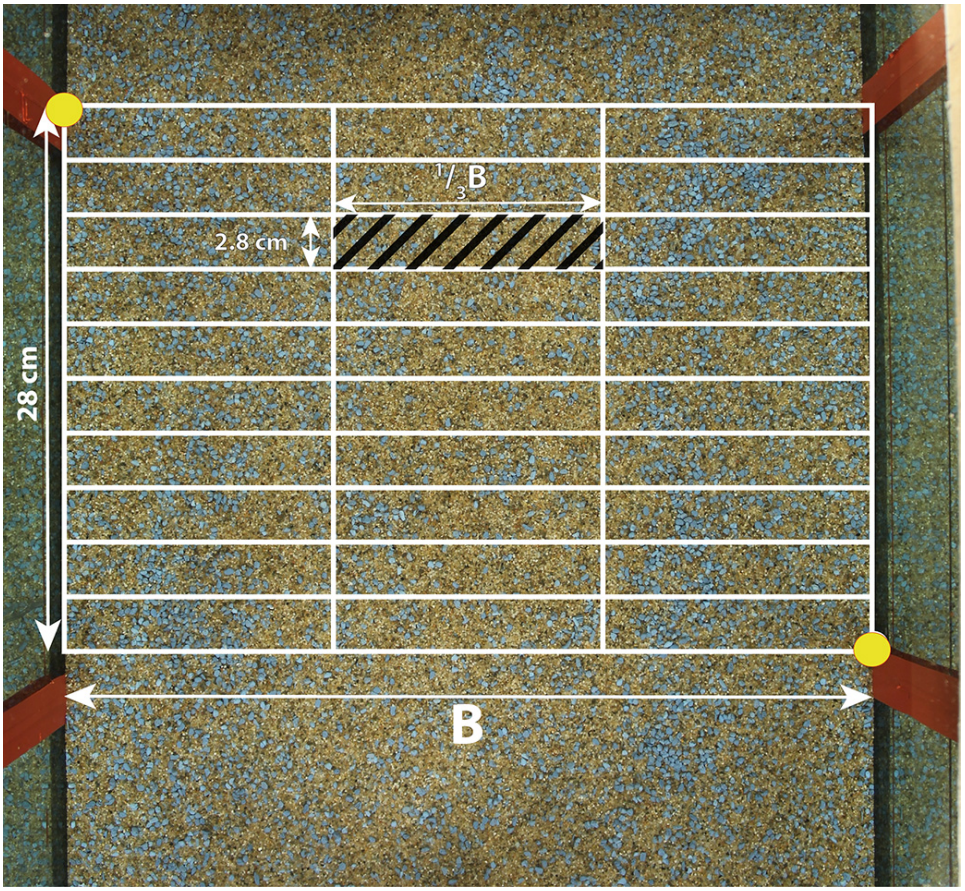

Figure 3.7: Picture of the flume bed to be analysed regarding grain size distribution. The picture is cropped using the coordinates of the red stripes on the side of the flume (yellow dots). The cropped image is divided into 10 equal areas in stream-wise direction and we then consider the middle one third of the width (hatched area). Each area is then analysed individually to obtain the areal fraction content.

(Figure 3.10b) is connected to a computer to which it sends the output signal.

3.4.5 Sediment discharge

A plastic container placed on a scale catches the sediment that is pumped out of the sand trap to measure the sediment discharge continuously during the experiment (Figure 3.11). The sand trap catches the sediment at the downstream end of the flume. By letting the water overflow and thus keeping the water level in the plastic container constant, the increased weight equals the increased submerged mass of the sediment. From this the sediment discharge can be calculated:

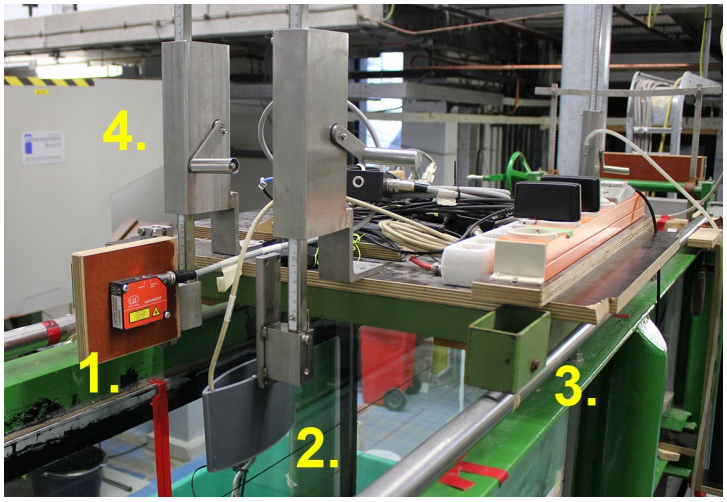

Figure 3.8: Picture of the water level laser (1.) and the bed level laser (2.) mounted on a carriage (3.). The bed level laser is placed inside a plastic box so that it can be positioned below the water surface. The vertical position of the lasers is measured using a ruler (4.)

$$V_s = \frac{m_{sub}}{\rho_s - \rho_w}, \tag{3.2}$$

in which V_s $[m^3]$ is the volume of sediment entering the plastic container, m_{sub} $[kg]$ is the submerged mass of the sediment, measured by the scale. $\rho_s = 2650$ $[kgm^{-3}]$ and $\rho_w = 1000$ $[kgm^{-3}]$ are, respectively the densities of sediment and water. The volume of sediment V_s per unit of time is the sediment discharge.

3.4.6 Grain size distribution of the sediment load

Samples from the sediment that is pumped from the sand trap to the green plastic container are taken every 30 minutes . Figure 3.12 shows the device to collect the samples. These samples are later sieved to analyse the ratio of coarse and fine fraction in the sediment discharge at the downstream end of the flume.

3.4.7 Measurement frequency

From the start of the experiment the measurements of the **bed elevation**, **water level** and **grain size distribution of the bed** need to be done as often as possible to provide sufficient data on the (possibly) rapid initial changes in the flume. This frequency was about 10 to 15 minutes. After about two hours the frequency was decreased to every 30 minutes.

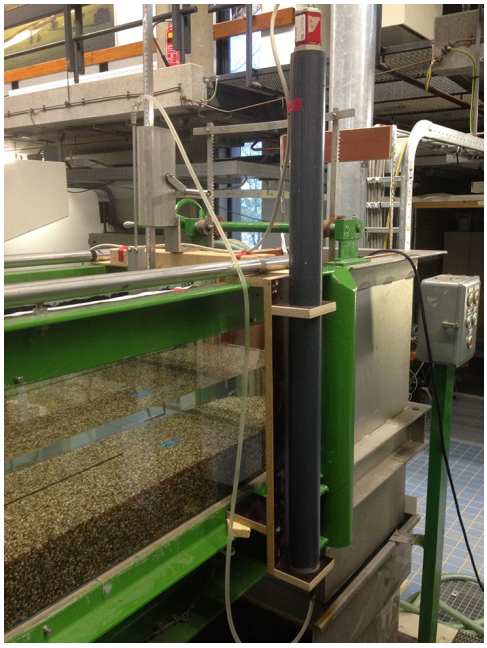

Figure 3.9: Water level meter at the downstream end of the flume. The meter is a Temposonics® magnetostrictive linear position sensor (G-series) and is fitted inside the grey tube, connected to a pitot tube in the water that measures the static water pressure.

The **water level downstream (base level)**, **discharge** and **sediment discharge** were measured continuously with time.

Samples of the **composition of the sediment discharge** were taken every 30 minutes.

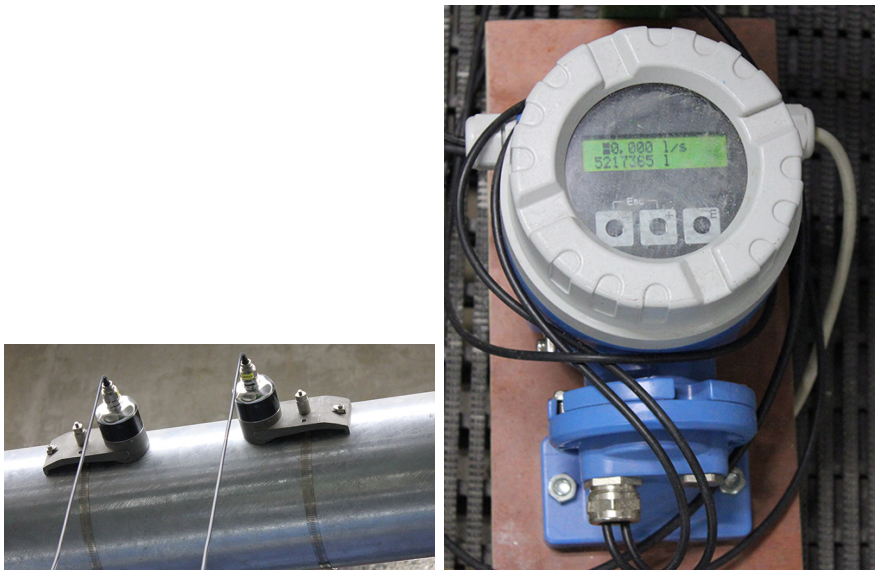

(a) Ultrasonic flow meter on the inflow pipe.

(b) Digital display connected to a computer.

Figure 3.10: Proline Prosonic Flow 91W Ultrasonic flow meter.

Figure 3.11: Plastic container (1.), placed on a scale (2.), to catch the sediment pumped out of the sand trap (3.). The water in the container is kept at a constant level (4.), thus the amount of increased weight equals the increased submerged weight of the sediment. The weight is read from a digital display (5.) connected to a computer to store the data.

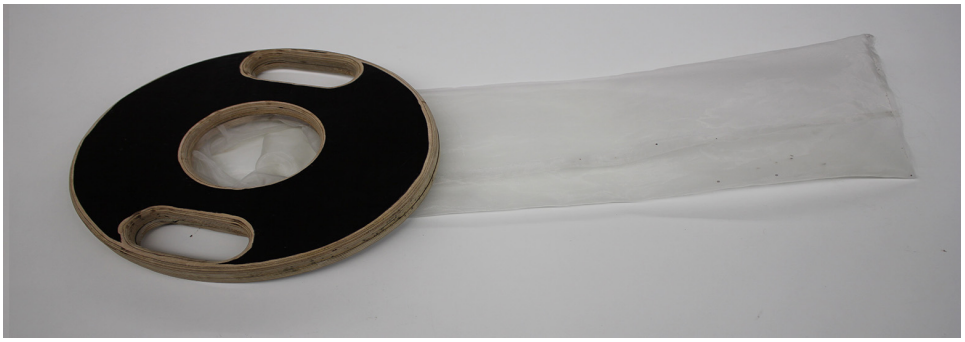

Figure 3.12: Device to collect samples from the sediment flow pumped out of the sand trap at the downstream end of the flume.

4 | Results and analysis of laboratory experiments

4.1 Tracer experiment (E1)

4.1.1 Experimental characteristics

The uniform sediment in this experiment is size fraction 2 of which a part is painted and installed in the shoal, acting as the tracer in this experiment. Figure 4.1 shows the Froude number on three different locations in the flume over time to illustrate that the experiment was governed by conditions of subcritical flow. The experiment lasted until the moment the upstream erosion — i.e. the erosion that occurred after the attachment to the upstream boundary as a result of a lack of sediment coming from upstream — reached the bottom of the flume: 6 h 59 min.

In Figure 4.2 the net weight of the sediment is shown, captured at the downstream end of the flume. The weight is the weight of the dry sediment. No tracer material reached the downstream end of the flume. Figure 4.3 shows the specific sediment discharge $[m^2 s^{-1}]$, calculated by taking a 30 min average of the net weight of sediment collected at the downstream of the flume (Figure 4.2) over time, calculating mass to volume with the sediment density $\rho_s = 2650$ $[kgm^{-3}]$.

4.1.2 Regions of interest

Figure 4.4 shows the bed and water level (top panel) and grain size distribution of the bed in terms of F_{a2} (bottom panel) at 2 h 20 min (after the start of the experiment). This figure points out three regions of interest:

I. Upstream region of degradation induced by the lack of sediment input from upstream since the sediment feed rate is set to be zero (Section 3.2.2).

II. Region over which the shoal has propagated.

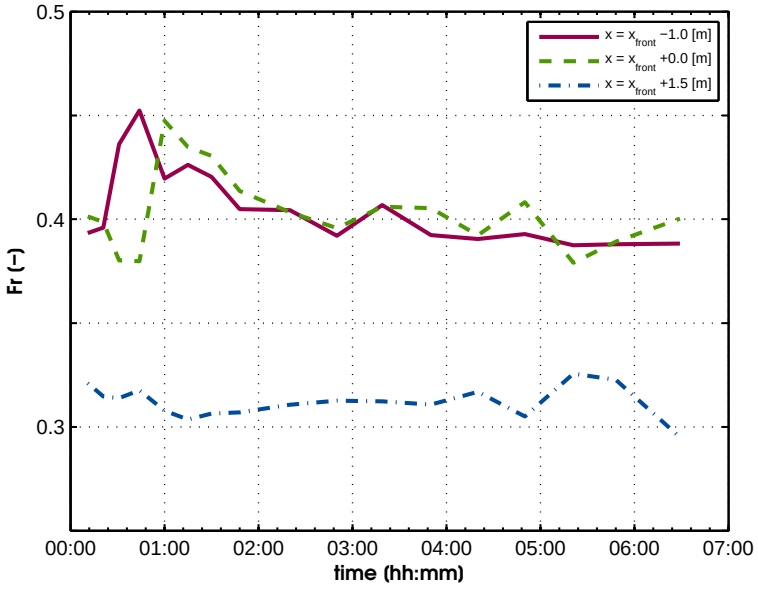

Figure 4.1: Froude number of the tracer experiment (E1) over time at three different locations in the flume, 1 m upstream of the shoal front, at the front of the shoal and 1.5 m downstream of the shoal front.

III. Region downstream of the shoal where no degradation of the bed occurred. Also no bedforms were present.

4.1.3 Bed level

Figure 4.5 shows the evolution of the bed level η with time. Due to a technical malfunction the bed level profiles were not measured until the end of the flume and differ in length. Figure 4.6 shows the bed level relative to the initial bed level.

The bed level evolution in time shows a distinct propagation of the shoal in downstream direction. From the beginning to 0 h 44min bed forms are present on the shoal. Further a region of erosion at the upstream boundary is visible, due to the lack of sediment feed.

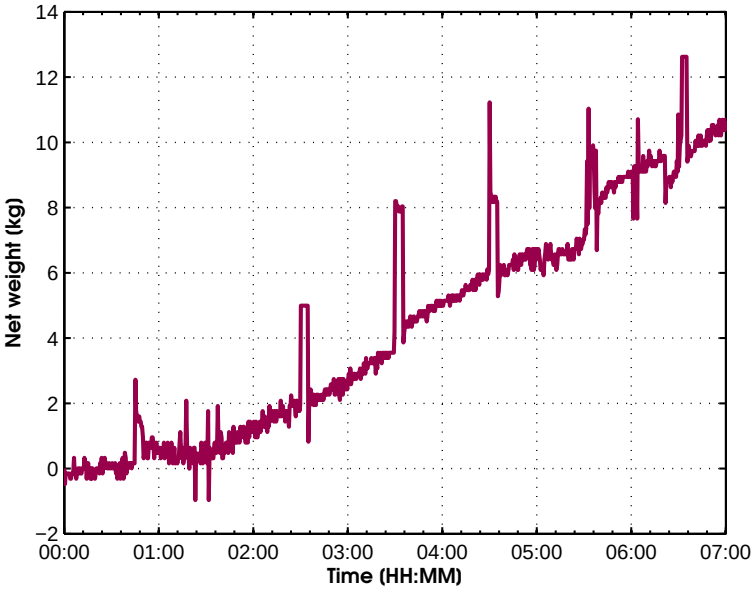

Figure 4.2: Net weight $[kg]$ of the sediment captured at the downstream end of the flume. The net weight is the weight of the dry sediment. The perturbations in the signals are due to the taking of the samples of grain size distribution of the sediment discharge. No tracer material reached the downstream end.

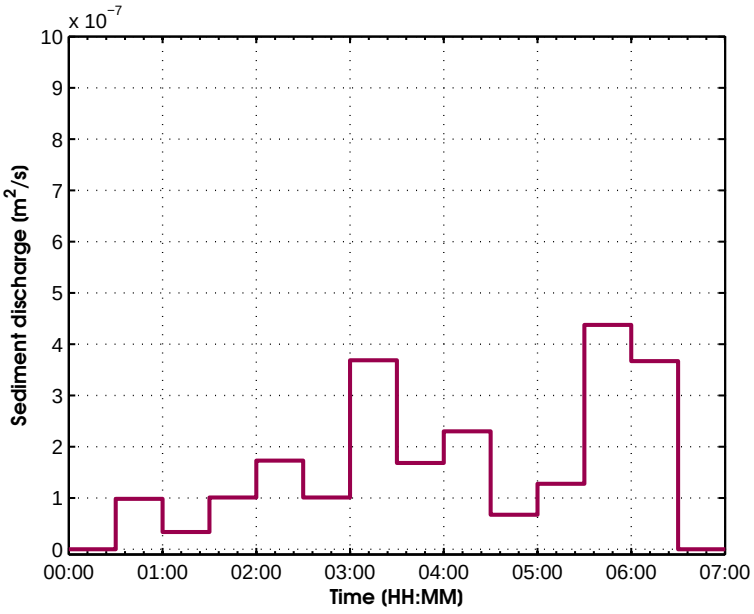

Figure 4.3: Specific sediment discharge $[m^2 s^{-1}]$ at the downstream end of the flume. The graph is constructed taking a 30 min average of the net weight of sediment collected at the downstream of the flume (Figure 4.2) over time, calculating mass to volume with the sediment density $\rho_s = 2650$ $[kgm^{-3}]$.

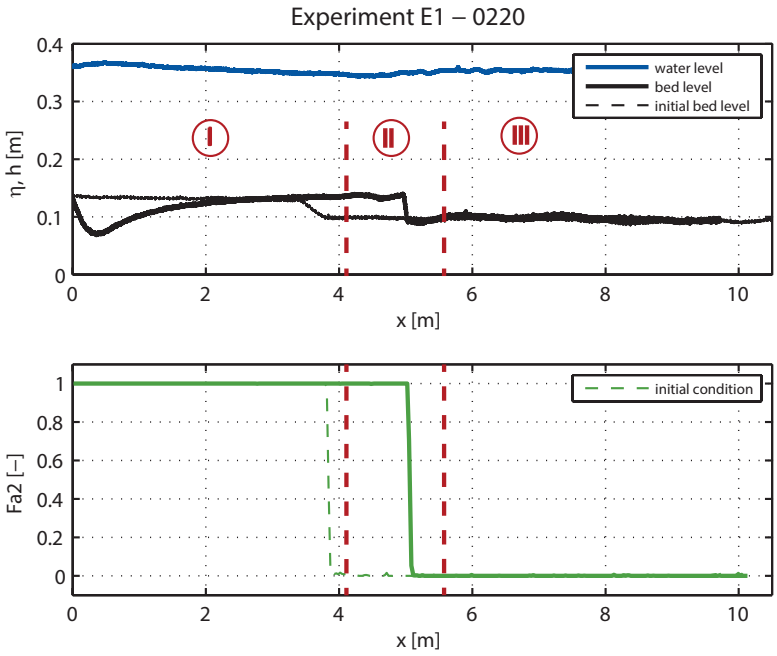

Figure 4.4: Result of Experiment E1, tracer experiment, at 2 h 20 min. In the top panel the water level (h) and bed level (η) and in the bottom panel the volume fraction content of the coarse fraction (F_{a2}). Flow is from left to right. In red the three regions of interest explained above are indicated.

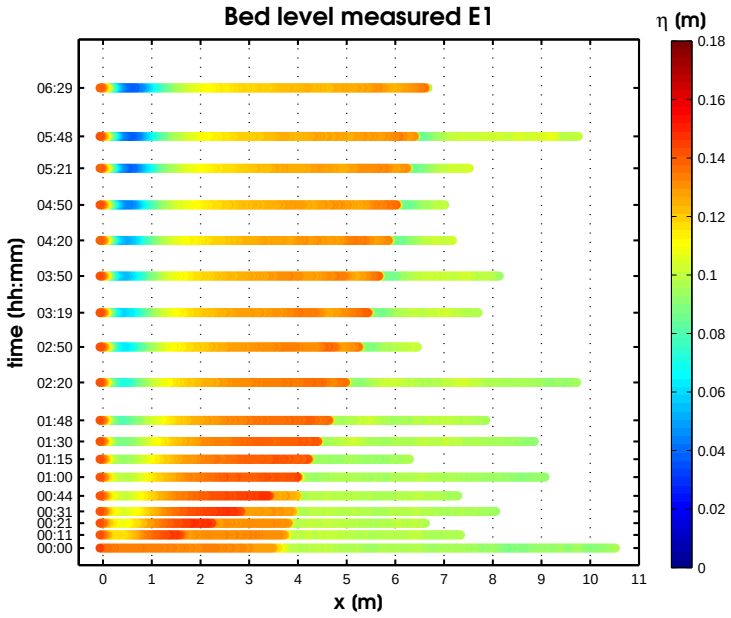

Figure 4.5: Bed level η $[m]$ over time of Experiment E1. The propagation of the shoal is well visible. Also the erosion at the upstream boundary is shown. Due to a technical malfunction the bed level profiles were not measured until the end of the flume and differ in length.

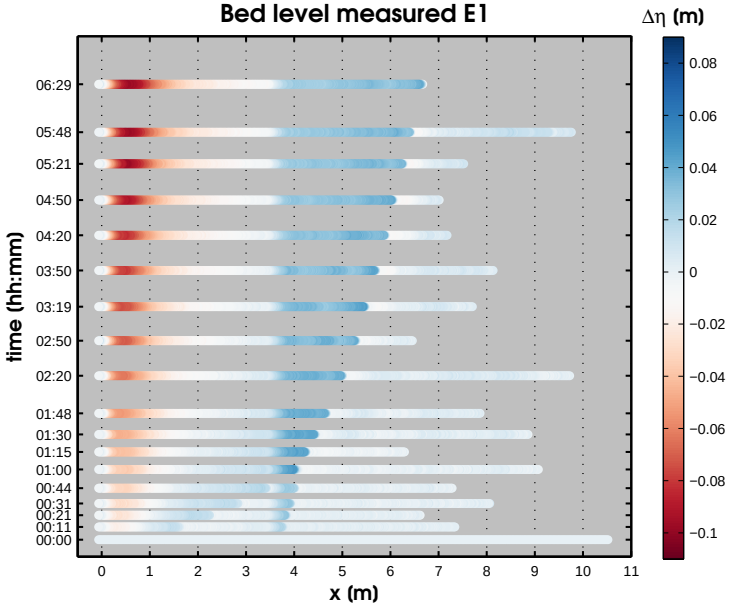

Figure 4.6: Bed level relative to the initial bed level $\Delta\eta = \eta - \eta_{initial}$ $[m]$ over time of Experiment E1. The propagation of the shoal is well visible. Also the erosion at the upstream boundary is shown.

4.1.4 Grain size distribution of the bed surface

Figure 4.7 shows the grain size distribution of the the bed over time in terms of the volume fraction content F_{a2} of the tracer fraction, which is only present in the shoal. As the tracer fraction has not passed the front of the shoal, the propagating shoal is accompanied by a change in the grain size distribution of the bed surface. Appendix C shows the actual pictures per time step, with flow from left to right.

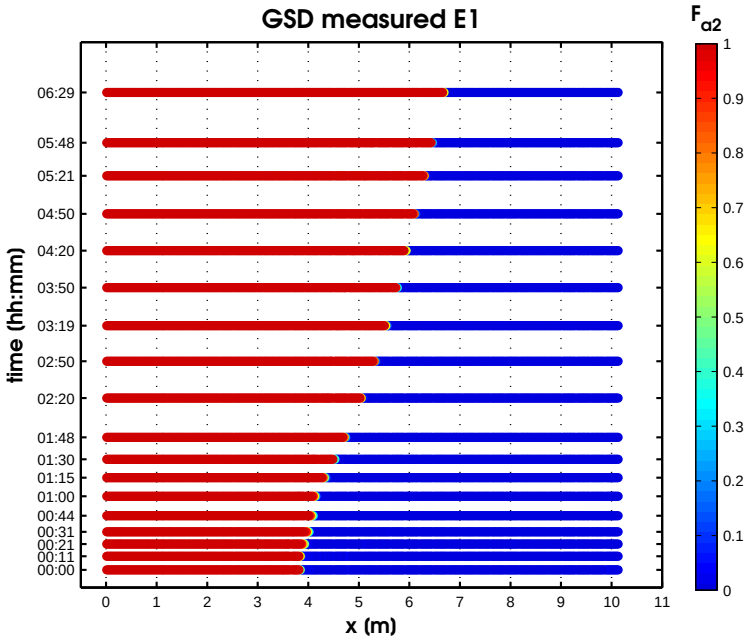

Figure 4.7: Grain size distribution of the bed surface (volume fraction content in the active layer of the painted fraction, F_{a2}) in Experiment E1.

4.1.5 Celerities of De Vries and Ribberink wave

Figure 4.8 shows the x-t diagram of the displacement of shoal front and of the front of the Ribberink wave, i.e. the most downstream x-coordinate for which $F_{a2} = 1$. It shows that there is no difference in celerity in the De Vries wave and the Ribberink wave, so the Ribberink wave does not precedes the De Vries wave in the tracer experiment.

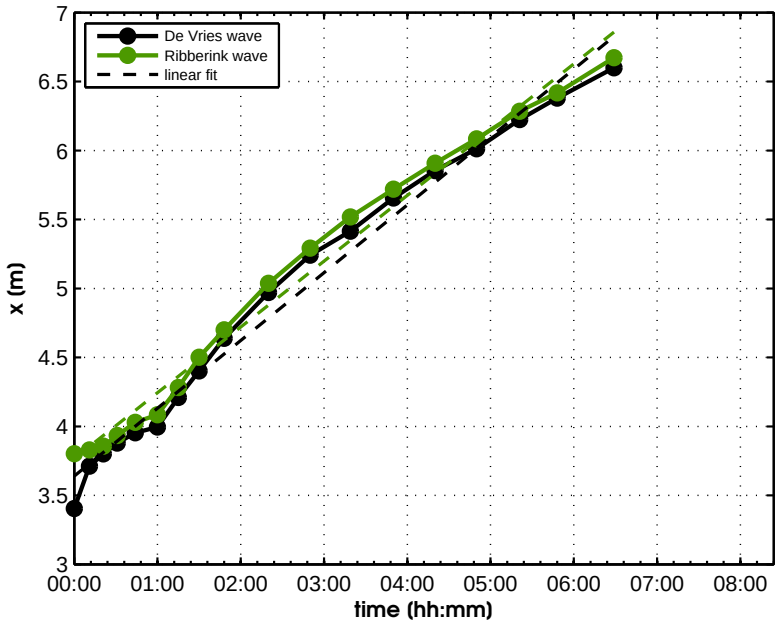

Figure 4.8: x-t diagram of tracer experiment E1 of displacement the front of the shoal and the front of the Ribberink wave, i.e. largest x-coordinate for which $F_{a2} = 1$. Ribberink wave and De Vries wave do not differ in celerity. In this experiment, uniform sediment is used; F_{a2} represents the painted tracer fraction of the shoal.

4.2 Mixed-size sediment experiment (E2)

4.2.1 Experimental characteristics

Experiment E2 is a mixed-size sediment with a bimodal sediment mixture. The experiment lasted until the moment the upstream erosion — i.e. the erosion that occurred downstream of the attachment to the upstream boundary as a result of a lack of sediment coming from upstream — reached the bottom of the flume: 7 h 55 min.

Figure 4.9 shows the Froude number over time at three different locations in the flume, respectively 1 m upstream of the shoal, at the shoal and 1.5 m downstream of the shoal to illustrate that the experiment was conducted in a subcritical flow regime.

In Figure 4.10 the net weight of the sediment discharge at the downstream end of the flume is shown, which is the weight of the dry sediment. The bottom panel shows the fraction content of the coarse and fine fraction. Figure 4.11 shows the specific sediment discharge $[m^2 s^{-1}]$, calculated by taking a 30 min average of the net weight of sediment collected at the downstream of the flume (Figure 4.10) over time, calculating mass to volume with the sediment density $\rho_s = 2650$ $[kgm^{-3}]$.

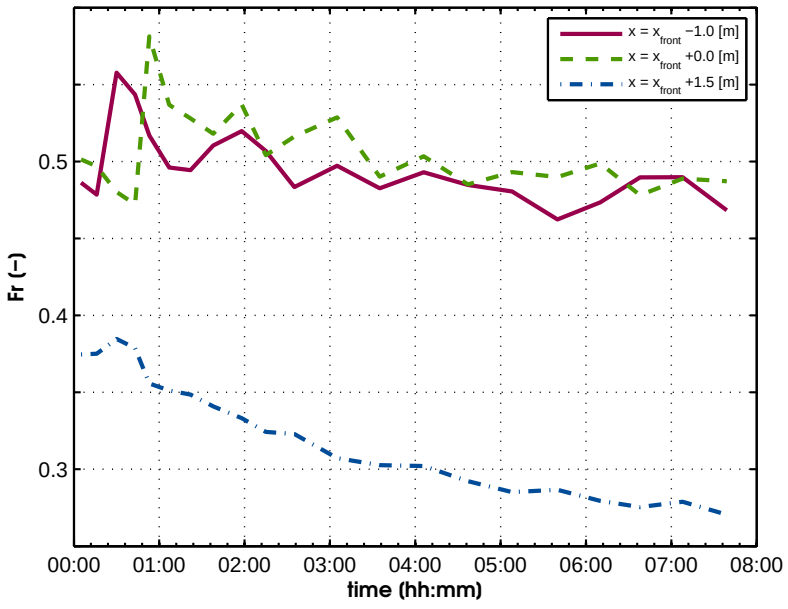

Figure 4.9: Froude number of Experiment E2 over time at three different locations in the flume, 1 m upstream of the shoal front, at the shoal front and 1.5 m downstream of the shoal front.

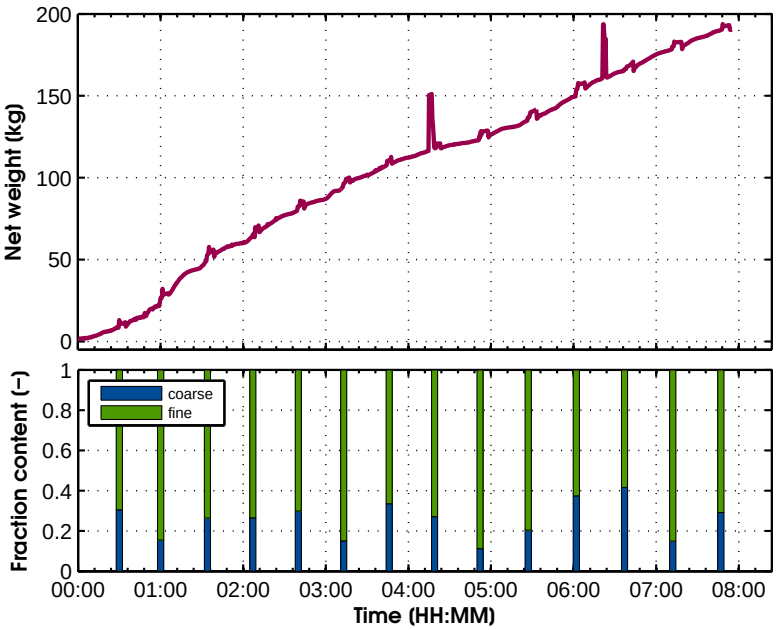

Figure 4.10: Net weight $[kg]$ of the sediment captured at the downstream end of the flume for the total sediment mixture, and per fraction. The net weight is the weight of the dry sediment. The perturbations in the signals are due to the taking of the samples of grain size distribution of the sediment discharge. The fraction content of the coarse and fine fraction is shown in the bottom panel.

4.2.2 Regions of interest

To point out the regions of interest and acting processes in the flume experiment the results of the experiment are plotted in Figure 4.12 at an arbitrary point in time. Figure 4.12 shows the result of Experiment E2, the mixed-size sediment experiment, at time of 1 h 58 min (after the start of the experiment). The top panel shows in black the bed level and in blue the water level, with flow from left to right. The bottom panel shows the grain size distribution of the bed surface in terms of the volume fraction content of the largest grain size (F_{a2}). The following regions are indicated in Figure 4.12:

I. Upstream region of degradation is induced by the lack of sediment feed from upstream.

II. Region over which the shoal has propagated.

III. Region just downstream of the front of the shoal governed by erosion.

IV. Region further downstream where small dunes are visible.

For the bottom panel in Figure 4.12, regarding the grain-size distribution:

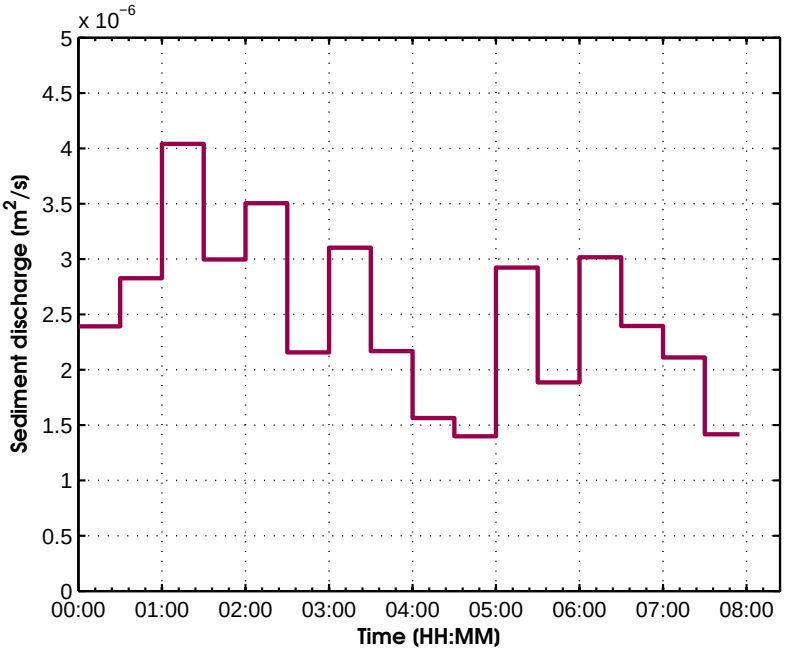

Figure 4.11: Specific sediment discharge $[m^2 s^{-1}]$ at the downstream end of the flume. The graph is constructed taking a 30 min average of the net weight of sediment collected at the downstream of the flume (Figure 4.10) over time, calculating mass to volume with the sediment density $\rho_s = 2650$ $[kgm^{-3}]$.

I. Region where the shoal consists of coarse sediment only.

II. Immediately downstream from the initial shoal the bed surfaces has become coarse due to a propagating shoal.

III. Region just downstream of the shoal, where the bed suffers from erosion and local fining.

IV. Region further downstream where an oscillatory behaviour of the grain size distribution signal is seen. Figure 4.13. shows a photograph of the bed at 2 h 35 min to illustrate the feature. The bed surface of the trough zones of the small dunes show a clear coarsening.

4.2.3 Bed level

Figure 4.14 shows the evolution of the bed level η over time. Figure 4.15 shows the bed level relative to the initial bed level. Due to a technical malfunction the bed level profiles were not measured until the end of the flume and differ in length. Directly downstream of the shoal a region of bed erosion is present.

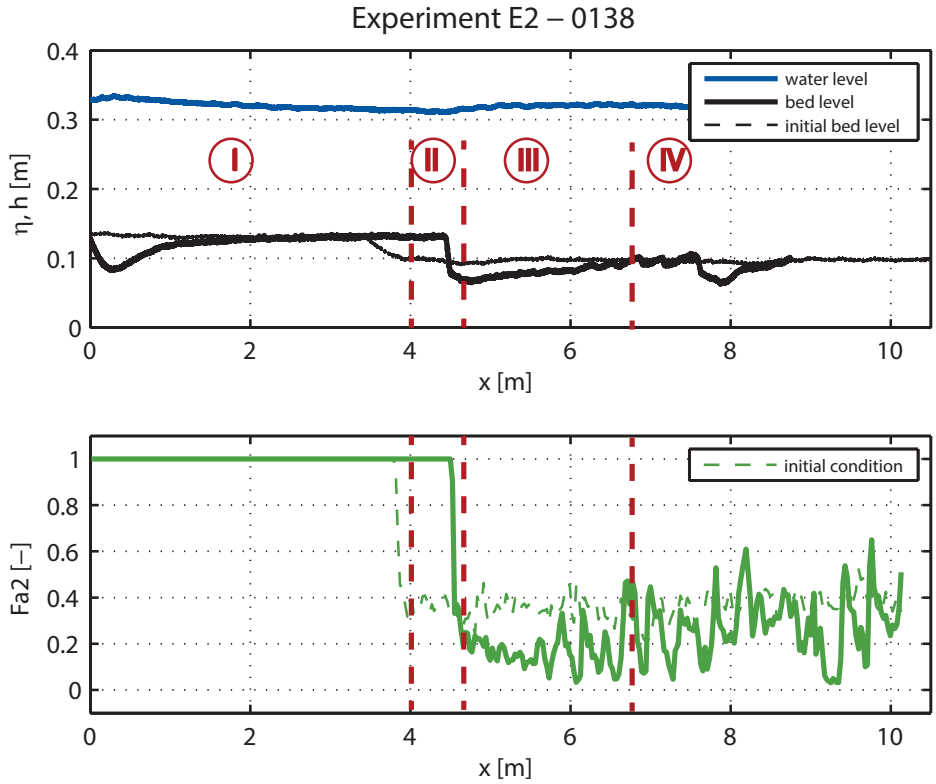

Figure 4.12: Result of Experiment E2, mixed-size sediment experiment, at 1 *h* 58 *min*. In the top panel the water level (h) and bed level (η) and in the bottom panel the volume fraction content of the coarse fraction (F_{a2}). Flow is from left to right. In red the four regions of interest explained above are indicated.

Figure 4.13: Photograph of the downstream part of the flume at 2 *h* 35 *min*. A sorting pattern is well visible. Flow is from left to right.

In Section 2.3.1 on page 19, a distinction between two different situations is made regarding shoal propagation: 1) a case with relatively 'low discharge'; and 2) a case with relatively 'high discharge'. The erosion downstream of the shoal indicates that situation 2 is applicable to this experiment. This means that the effect of the streamwise decrease of the sediment transport rate due to a streamwise increase of flow depth is smaller than the

effect of the streamwise increase of the sediment transport rate due to the smaller average grain size of the bed than the one of the shoal. The net sediment transport rate therefore increases downstream of the shoal, resulting in erosion of the bed downstream of the shoal.

The downstream slope of the erosion 'pit' (region III) smooths out over time since the sediment transport gradient becomes smaller, which is due to the increasing flow depth. When transport rates in the erosion 'pit' become smaller, relative less sediment comes from upstream. With still the same sediment transport rates on the slope, the slope will lower due to erosion, creating a slope with a smaller gradient. This can be seen in the profiles of the bed level for every time shown in Appendix B.

The maximum erosion in that region, relative to the initial bed level, over time $\Delta\eta_{max}(t)$ is plotted in Figure 4.16.

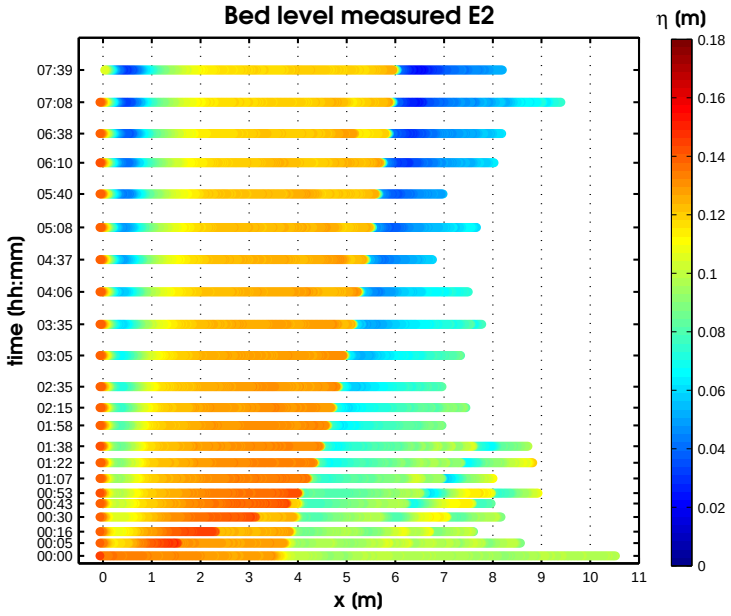

Figure 4.14: Bed level η $[m]$ over time of Experiment E2. Both the propagation of the shoal as well as the erosion downstream of the shoal are well visible. Also the erosion at the upstream boundary is shown. Due to a technical malfunction the bed level profiles were not measured until the end of the flume and differ in length.

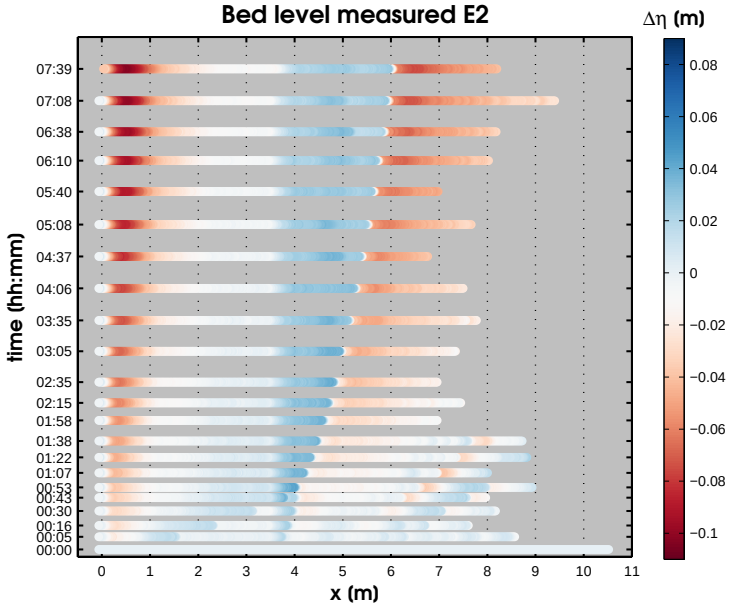

Figure 4.15: Bed level relative to the initial bed level $\Delta\eta = \eta - \eta_{initial}$ $[m]$ over time of Experiment E2. Due to a technical malfunction the bed level profiles were not measured until the end of the flume and differ in length.

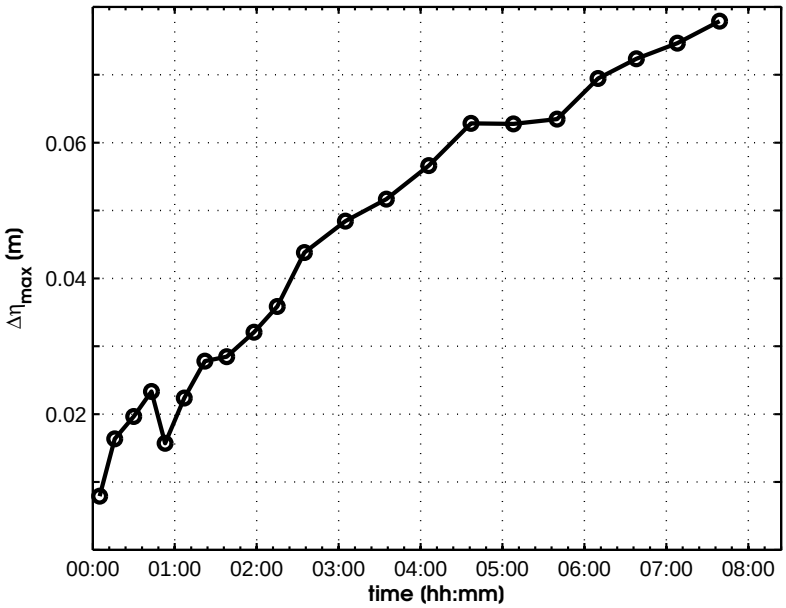

Figure 4.16: The maximum depth of erosion in Experiment E2, $\Delta\eta_{max} = \eta_{initial} - \eta_{min}$, where η_{min} denotes the lowest point in the erosion region downstream of the shoal.

Figure 4.18 shows the distance from the front of the shoal to the point of maximum erosion as a function of the shoal height δ (shown in Figure 4.17). Downstream of the shoal a zone of recirculation is present due to flow separation (Figure 2.11, Section 2.3.2). According to Bradshaw and Wong (1972) the distance of the shoal front to the point of reattachment of the flow is in the order of 10 times the shoal height, $O(10\delta)$. This corresponds reasonably well with the findings from the flume experiment plotted in Figure 4.18, i.e. the location of maximum erosion is found around 4.5–7 times the shoal height δ. At the location of reattachment of the flow the turbulence bursts and sweeps are most intense (Kim et al., 1980). Therefore it is reasonable to assume that the location of maximum erosion is the reattachment point.

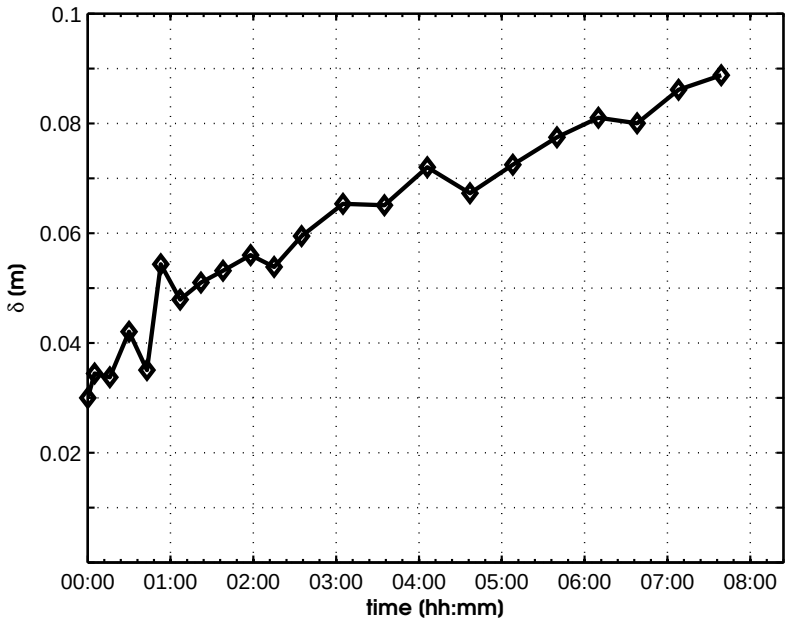

Figure 4.17: Shoal height δ in Experiment E2 as a function of time. The shoal height is measured vertically from the top of the shoal until the bed level directly downstream of the shoal.

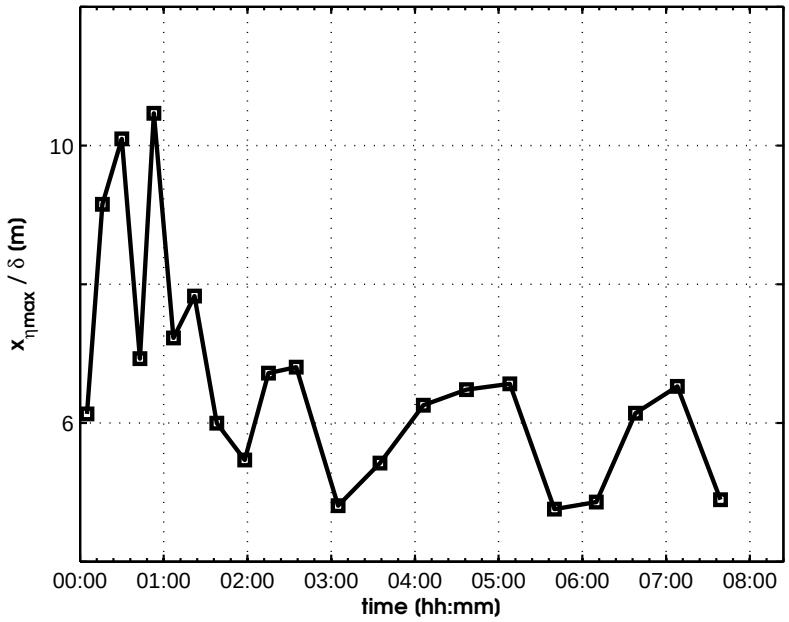

Figure 4.18: Distance of point of maximum erosion downstream of the front of the shoal, relative to the height of the shoal (δ). Experiment E2

4.2.4 Grain size distribution of the bed surface

Figure 4.19 and Figure 4.20 show the grain size distribution of the bed (represented by the volume fraction content of the coarse fraction in the active layer, F_{a2}) in time, both the absolute values and the values relative to the initial grain size distribution $F_{a2,ini}$ ($\Delta F_{a2} = F_{a2} - F_{a2,ini}$). Appendix D shows the actual pictures per time step, with flow from left to right. In Region III a region of fining is visible downstream of the shoal (Figure 4.12).

The fining of the bed downstream of the shoal is in contrast with what was elaborated on in Section 2.3.1 on shoal propagation. In the situation of a 'high discharge', which applies for this experiment, a coarsening of the bed downstream of the shoal is predicted because fine sediment is more mobile than coarse sediment for the same flow characteristics. This is not the case in this experiment. Two explanations can be given: (1) reverse mobility — this means that due to the effects of hiding and exposure, the finer fraction becomes less mobile than the coarse fraction; (2) fining because of the recirculation zone downstream of the shoal (Figure 2.11, Section 2.3.2) that transports fine material upstream while the recirculating flow is not strong enough to transport the coarse fraction upstream. The fining of the bed both occurs upstream and downstream of the point of maximum bed erosion, which seems to agree with the point of flow reattachment. The turbulent bursts and sweeps direct sediment in both up and downstream direction. In downstream direction the sediment is stirred up, the fine fraction is entrained in the flow and therefore transported more easily downstream, covering the coarser fraction.

(3) A third possibilljty is that the fining is caused by sorting of the sediment on the dunes present. Figure 4.14 (better visible in Appendix B) shows bed forms developing right after the start of the experiment. Dune sorting is a certain organization of particles over depth (vertical sorting) caused by the single grains rolling further down the lee face side of the bed form than finer grains. Moreover, due to coarser grains are move more easily to the toe of the lee face, because in the avalanching process that occurs at the lee face side, coarse grains are moved up to the surface of the avalanche causing finer grains to move more slowly and become lodged more easily (Blom et al., 2003). The process of dune sorting is illustrated in Figure 4.21.

Since the fining occurs more in the part of the bed close to the shoal, a combination of explanations 2 and 3 seems to be the more likely explanation for the fining downstream of the shoal. It is plausible that initially the dune sorting occurred, causing the part of the bed close to the shoal to become more fine because of the turbulent recirculation zone, which had no effect on the downstream part of the mixed-sediment reach.

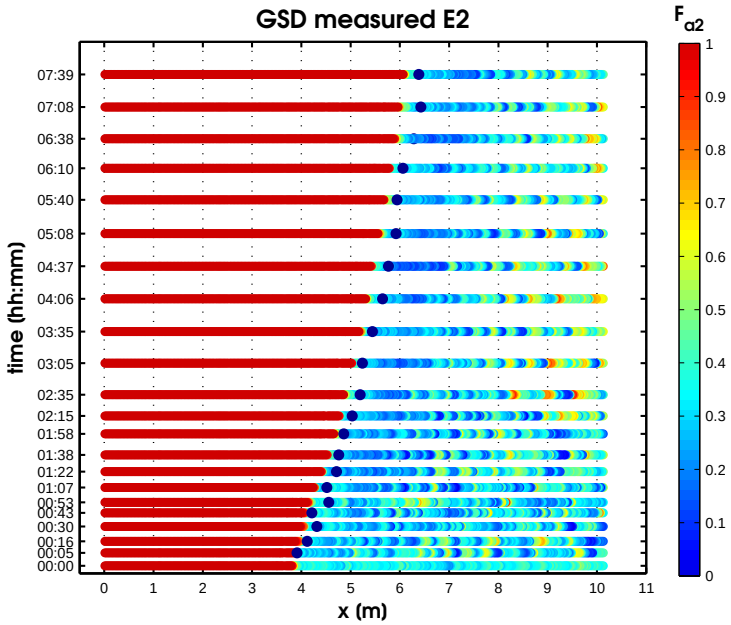

Figure 4.19: Grain size distribution of the bed (volume fraction content in the active layer, F_{a2}) in Experiment E2. A region of fining is well visible downstream of the shoal.

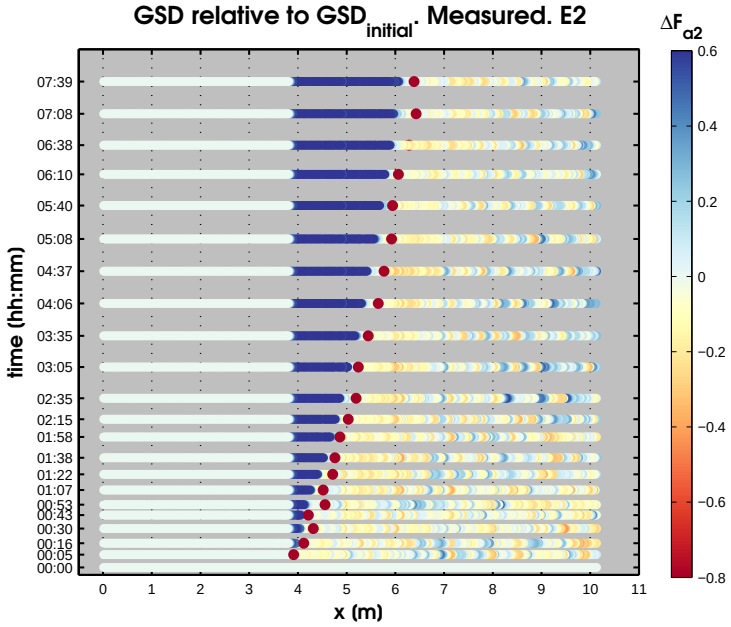

Figure 4.20: Grain size distribution of the bed (volume fraction content in the active layer, F_{a2}) in Experiment E2 relative to the initial grain size distribution. A region of fining is well visible downstream of the shoal. The red dots are the locations of the deepest erosion.

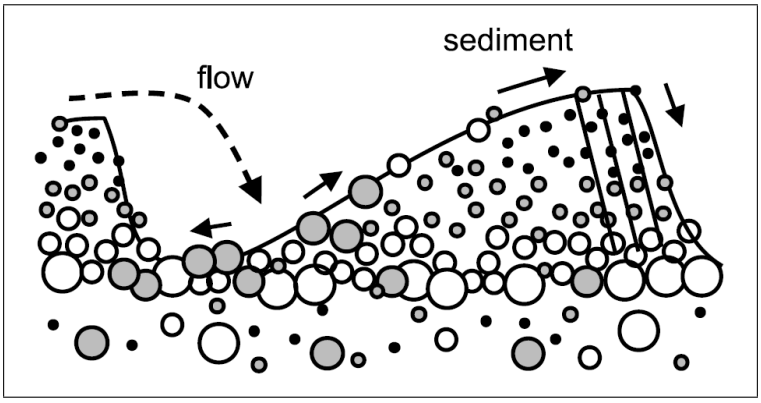

Figure 4.21: Vertical sorting of bed form material and accumulation of coarse material beneath migrating bed forms. From Blom et al. (2003).

4.2.5 Celerities of De Vries and Ribberink wave

Figure 4.22 shows the x-t diagram showing the displacement of the front of the shoal and the front of the Ribberink wave (location of maximum erosion, Figure 4.18). The figure shows that the Ribberink wave precedes the shoal, but both have the same celerity. This can be explained by the fact that the Ribberink wave does travel with a slightly higher celerity than de De Vries wave (the propagating shoal) and this effect goes together with erosion downstream of the shoal. The Ribberink wave triggers a degradation wave of the bed. The coarsening wave, the Ribberink wave is in this case, gives rise to an increase of sediment transport, resulting in bed degradation. The recirculation zone arising because of the erosion downstream of the shoal, can prohibit the Ribberink wave to travel faster than the shoal.

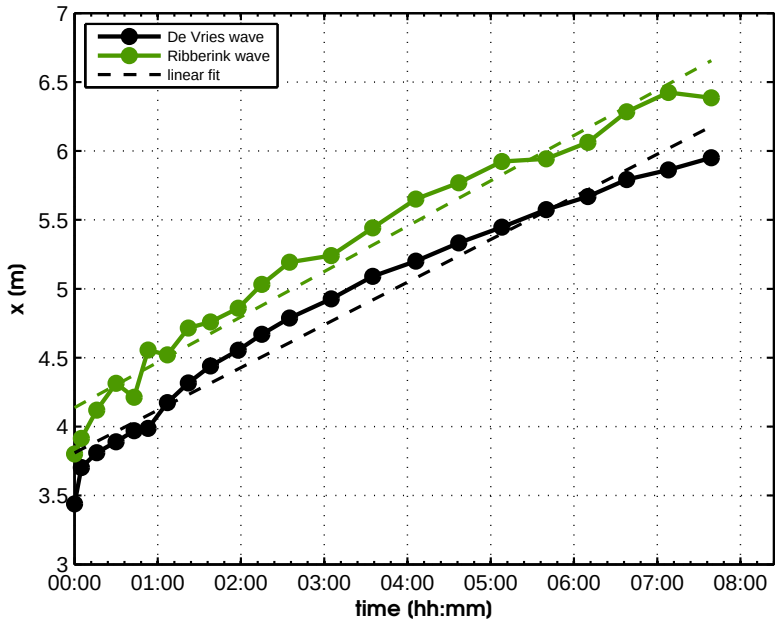

Figure 4.22: x-t diagram of Experiment E2 of the displacement of the front of the shoal and the front of the Ribberink wave, i.e. location of maximum erosion. Ribberink wave and De Vries wave do not differ in celerity. The dashed lines are linear fits through the data of which the gradient represents the celerity of the associated wave.

5 | Numerical predictions

5.1 Mathematical description of numerical model

The numerical model, developed and described by Stecca et al. (submitted), solves the one-dimensional, non-linear system of partial differential equations (PDEs) given by the Saint-Venant-Exner equations for free-surface flow (Equations 2.1 to 2.3) coupled with the Hirano active layer equations for mixed-sediment morphodynamics (Equation 2.5). The coupled Saint-Venant-Hirano model results in a non-conservative system of PDEs, which has been analysed by Stecca et al. (2014).

A sediment transport model is needed to evaluate the bed load transport of each fraction ($q_{bk} = F_{ak}Q_{bk}$). The model for the grainsize-selective sediment transport considered here is the relation by Meyer-Peter and Müller (1948) including the hiding-exposure correction by Egiazaroff (1965):

$$Q_{bk} = A\left(\Delta g d_{sk}^3\right)^{1/2} \max\left(\left(\mu\theta_k - \xi_k\theta_c\right), 0\right)^B, \tag{5.1}$$

in which θ_c is the critical Shields stress, A and B are dimensionless and constant parameters, Δ is the submerged density defined as $\Delta = \rho_s/\rho_w - 1$, where $\rho_s = 2650\ \ kgm^{-3}$ and $\rho_w = 1000\ \ kgm^{-3}$, respectively, the sediment and water density. The ripple factor $\mu \leq 1$ is the ratio of grain shear stress and total bed shear stress (Ribberink, 1987). θ_k is the Shields number relative to the k-th sediment fraction, defined as:

$$\theta_k = \frac{q^2}{\Delta d_{sk} C^2 g h^2}, \tag{5.2}$$

with C the dimensionless Chézy coefficient, defined as $C = C_D/\sqrt{g}$, with $C_D\ [m^{1/2}s^{-1}]$ the dimensional Chézy coefficient. C is assumed constant. The correction factor for the hiding effect for the k-th fraction ξ_k as formulated by Egiazaroff (1965), is given by:

$$\xi_k = \left(\frac{\log_{10} 19}{\log_{10}\left(19\frac{d_{sk}}{\overline{d_s}}\right)}\right)^2, \tag{5.3}$$

The correction factor ξ_k for hiding effects reduces the mobility of the finer grains and enlarges the mobility of the coarser grains compared to a case with uniform sediment.

The system is numerically solved by path-conservative numerical methods (Maso et al., 1995), which enable for restoration of conservation even adopting a non-conservative formulation and thus are able to reproduce the speed of waves as described by the system of partial differential equations. In detail, the DOT method of Dumbser and Toro (2011), extended to second-order accuracy in the ADER framework (Toro and Titarev, 2002), is implemented.

5.2 Numerical settings

In this chapter, the flume experiments of Chapter 3, Experiments E1 and E2 are numerically reproduced. The initial and boundary conditions in the numerical simulations are set identical to the ones in the flume experiments. The grain sizes used in the model are set to the d_{50} of the sediment fractions used in the flume experiments.

The experiments are numerically modelled employing the second-order ADER-ENO DOT scheme (Stecca et al., submitted) with $CFL = 0.9$. The computational domain of 10 meters is divided into 200 equally spaced computational cells.

5.2.1 Calibration of the friction coefficient

Friction, in the form of a dimensionless Chèzy coeffient C, is calibrated by calculating backwater profiles with the numerical model with a fixed bed for various values of C. The predicted backwater profiles are compared with the measured profiles giving, where the computations with the best fitted backwater profiles gives the best value for the dimensionless Chèzy coeffient C. Figure 5.1a shows the backwater profiles for numerical predictions of tracer Experiment E1 on time 2 h 20 min. The Chezy value resulting in the numerically predicted backwater curve best resembling the measured backwater curve is $C = 14$. In dimensional form $C_D = C\sqrt{g} = 14\sqrt{g} = 43.8$ $[m^{1/2}s^{-1}]$. For Experiment E2 the numerically predicted backwater curves are presented in Figure 5.1b on time 2 h 15 min. $C = 14$ results in the best resemblance of the measured backwater curve.

5.2.2 Calibration of parameters for bed load formulation

The coefficients in the Meyer-Peter and Müller bedload transport equation (Equation 5.1) are calibrated to the data obtained from the flume experiments. The starting point for the values — A, B, μ, θ_{cr} — are the values

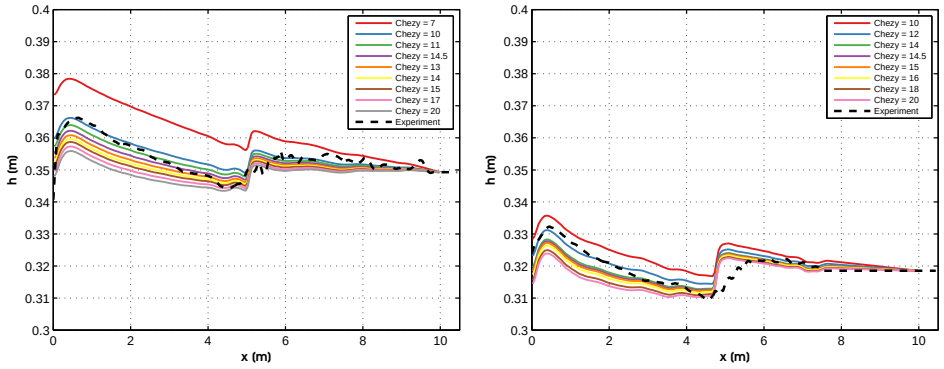

(a) E1 **(b)** E2

Figure 5.1: Comparison of backwater profiles for different dimensionless Chezy friction coefficients C. Subfigure (a) shows the backwater profiles for numerical predictions of tracer Experiment E1 on time 2 h 20 min. The Chezy value resulting in the numerically predicted backwater curve best resembling the measured backwater curve is $C = 14$. In dimensional form $C_D = C\sqrt{g} = 14\sqrt{g} = 43.8\ [m^{1/2}s^{-1}]$. For Experiment E2 the numerically predicted backwater curves are presented in subfigure (b) on time 2 h 15 min. $C = 14$ results in the best resemblance of the measured backwater curve.

of the original Meyer-Peter and Müller bedload formulation (Meyer-Peter and Müller, 1948), namely: $A = 8,\ B = 1.5,\ \mu = 1$ and $\theta_{cr} = 0.047$.

The following quantities were available to calibrate the parameters on:

- Sediment transport measured at the downstream end of the flume
- The composition of the sediment transport (fraction of coarse and fine)
- Erosion depth both at the upstream end, as well as downstream of the shoal
- Transport velocity of the shoal

The parameters $A,\ B$ and θ_{cr} were set equal for both experiments, since differentiating them between both experiments would be physically unrealistic. The ripple factor was kept at $\mu = 1$ in the tracer experiment (E1) since no bed form arised in the flume experiment

The composition of the sediment discharge was not used as a calibration quantity since the change of grain size distribution of the bed would have great effect on the composition of the sediment discharge and the change of grain size distribution is a phenomenon that we want to study in this numerical experiment and compare with the flume experiments.

We used the following order in calibrating the parameters of the transport equation:

1. First the parameters were calibrated on the sediment transport at the downstream end of the flume;
2. it was then found that the erosion depth at the upstream end was not sufficient which led to the conclusion that the threshold for incipient motion of the coarse fraction was too high, resulting in lowering the value of the critical shear stress to $\theta_{cr} = 0.03$;
3. this led to a too high transport velocity of the shoal through the domain. The transport velocity was lowered by decreasing A.
4. Through iteration the optimal values for A and μ were found for Experiment E2

Figure 5.2 shows the specific sediment discharge for Experiment E1 at the downstream end of the flume together with the measured specific sediment discharge. For the predicted values the sediment transport rates of the tracer material and the material original in the bed are also shown. In the flume experiment no tracer material reached the downstream end of the flume. The sediment transport in the tracer experiment is significantly higher than the measured sediment transport. The reason for this is unknown.

Figure 5.3 shows the specific sediment discharge at the downstream end of the flume together with the measured sediment discharge for Experiment E2. The predicted transport rates of the coarse and fine material are also shown. For the flume experiment this composition was measured by taking samples at certain time intervals. The results of this was already shown in Chapter 4, Figure 4.11. The total predicted sediment discharge seems coincide quite well with the measured sediment discharge.

The active layer thickness is set to $L_a = 2\overline{d_{90}}$ $[m]$, for Experiment E1. The geometric grain size of the mixture for which 90% of the grains is finer $\overline{d_{90}}$ is given by:

$$\overline{d_{90}} = d_{ref} 2^{\psi_s} \tag{5.4}$$

$$\psi_s = \sum F_{ak} \psi_k \tag{5.5}$$

$$\psi_k = \log_2 \frac{d_{k,90}}{d_{ref}}, \tag{5.6}$$

with the reference diameter $d_{ref} = 1\ mm$ and $d_{k,90}$ is the grain size for which 90% is finer in size fraction k. This imposed value of the active layer thickness is known to be reasonable since for a plane bed case holds $L_a = n_a d_{90}$, with n_a ranging from 1–2 (Parker, 2004). For Experiment E2 the active layer thickness was set to $L_a = 0.03$ $[m]$, equal to the average bed form height present in the downstream part of the flume.

The calibrated values for A, B, μ, L_a and θ_{cr} for both predictions of Experiment E1 and E2 are given in Table 5.1.

Table 5.1: Parameters of the numerical setup. A, B, μ and θ_{cr} are variables in the Meyer-Peter and Müller bed load transport equation (Equation 5.1).

		Prediction	
Variable	**Unit**	E1	E2
C	$[-]$	14	14
L_a	$[m]$	$2\overline{d_{90}} = 0.0050$	0.030
A	$[-]$	1.8	1.8
B	$[-]$	1.5	1.5
μ	$[-]$	1.0	0.86
θ_{cr}	$[-]$	0.030	0.030

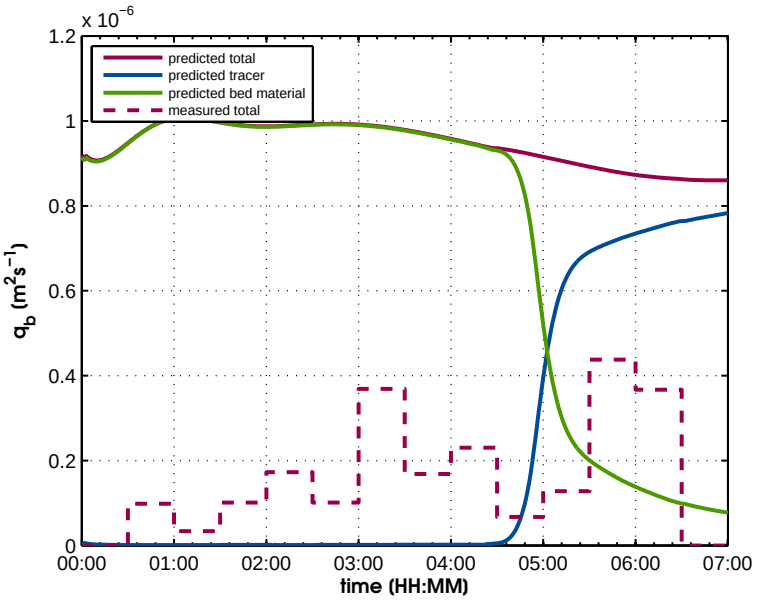

Figure 5.2: Predicted total specific sediment discharge of Experiment E1 at the downstream end of the flume including the mean value.

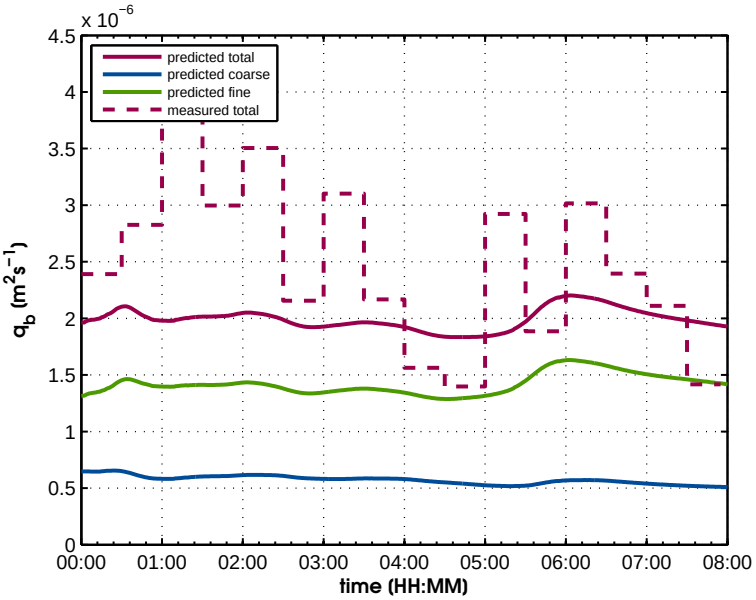

Figure 5.3: Predicted total specific sediment discharge of Experiment E2 at the downstream end of the flume including the mean value. Around 1 hour, a coarsening wave reaches the end of the flume causing the sediment transport rate to go down.

5.3 Predicted results for tracer experiment E1

5.3.1 Results

Figure 5.4 shows the predicted bed level η $[m]$ over time for flume experiment E1. The figure shows a clear propagation of the shoal in downstream direction. Erosion at the upstream end is caused by the lack of sediment input. Although erosion occurs, it is not as severe as was observed in the flume experiment E1 (Figure 5.5). This may be due to the fact that the recirculation zone that was present in flume experiment was not reproduced by the numerical model. Figure 5.6 and Figure 5.7 respectively show the predicted and measured bed level relative to the initial bed level.

Figure 5.8 shows the predicted grain size distribution of the bed over time in terms of the volume fraction content of the tracer fraction F_{a2}. The bed downstream of the shoal shows that tracer material has travelled further than the shoal. This means that tracer material from the shoal precedes the bed wave. Figure 5.9 shows the measured grain size distribution of Experiment E1 in which the tracer material not precedes the front of the shoal.

5.3.2 Comparison with experimental data

In Figure 5.10 the displacements are shown of the front of the shoal (De Vries wave) and the Ribberink wave — the front (dot-dashed line) and the x-coordinate of the centroid for the part where $0 < F_{a2} < 1$ — of both the flume experiment E1 and the numerical prediction of this experiment. The figure shows that the celerities of the Ribberink wave are much higher than the celerity of the De Vries wave. This means that tracer material has travelled further than the shoal, in contrast to what was seen in the flume experiment where no tracer material preceded the shoal front. The higher celerity of the front of the Ribberink wave than that of the centroid also shows that the tracer material has spread over the bed downstream of the shoal.

The Ribberink wave celerity is directly proportional to the sediment discharge and inversely proportional to the active layer thickness. Figure 5.2 shows that the predicted sediment discharge is to high compared to the measured sediment discharge. This could be a reason for the large Ribberink wave celerity.

5.3.3 Conclusions

It can be concluded that the numerical prediction of the tracer experiment (E1) shows a similar transport of the shoal, i.e. De Vries wave, to the flume experiment. In the numerical predictions the tracer material travels over and further than the front of the shoal, as opposed to the tracer material in

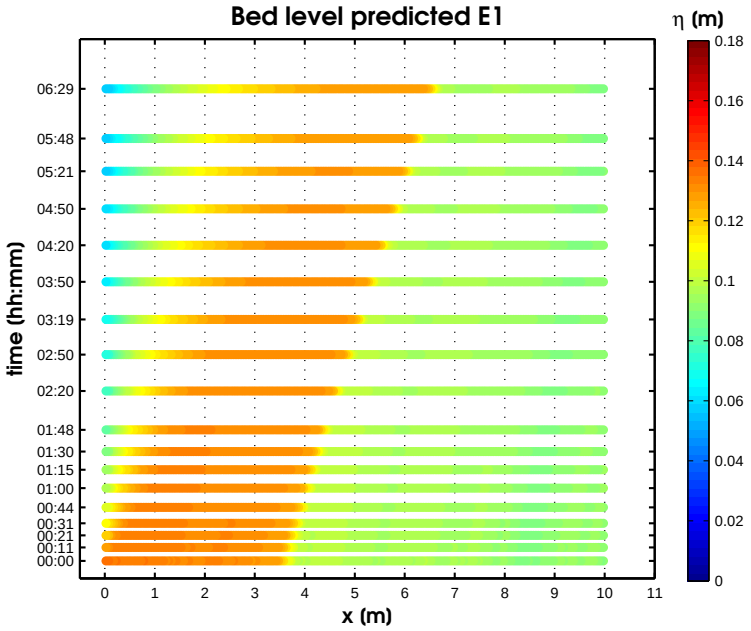

Figure 5.4: Numerical model prediction of the bed level η $[m]$ over time of Experiment E1.

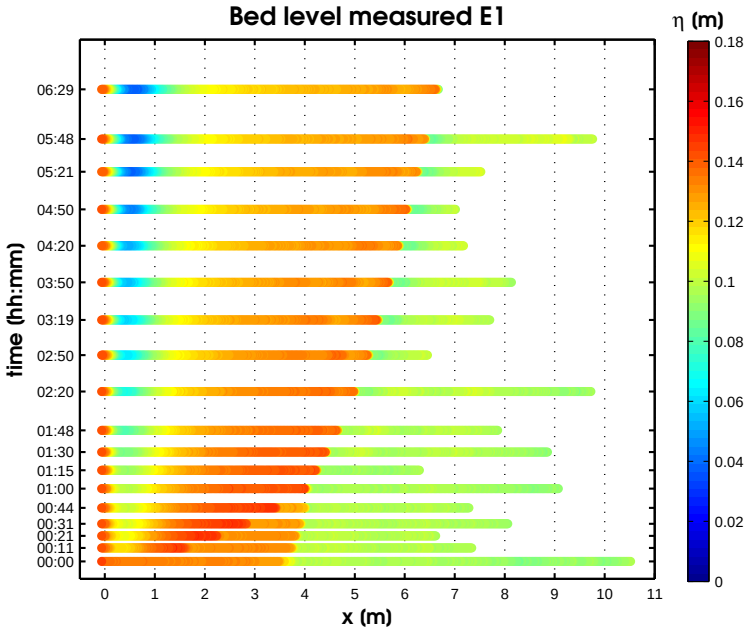

Figure 5.5: Bed level η $[m]$ over time of Experiment E1. The propagation of the shoal is well visible. Also the erosion at the upstream boundary is shown. Due to a technical malfunction the bed level profiles were not measured until the end of the flume and differ in length.

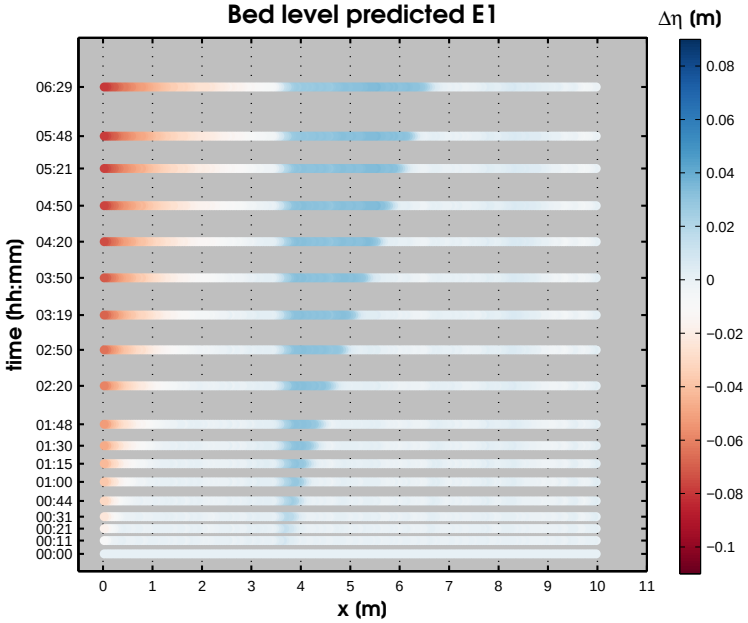

Figure 5.6: Numerical model prediction of the bed level relative to the initial bed level ($\Delta\eta = \eta - \eta_{initial}$ $[m]$) over time of Experiment E1.

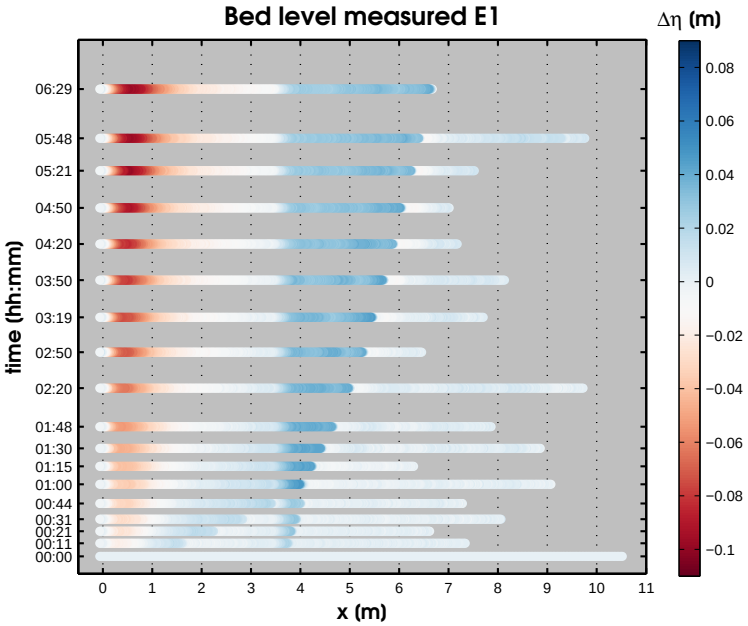

Figure 5.7: Bed level relative to the initial bed level ($\Delta\eta = \eta - \eta_{initial}$ $[m]$) over time of Experiment E1. The propagation of the shoal is well visible. Also the erosion at the upstream boundary is shown. Due to a technical malfunction the bed level profiles were not measured until the end of the flume and differ in length.

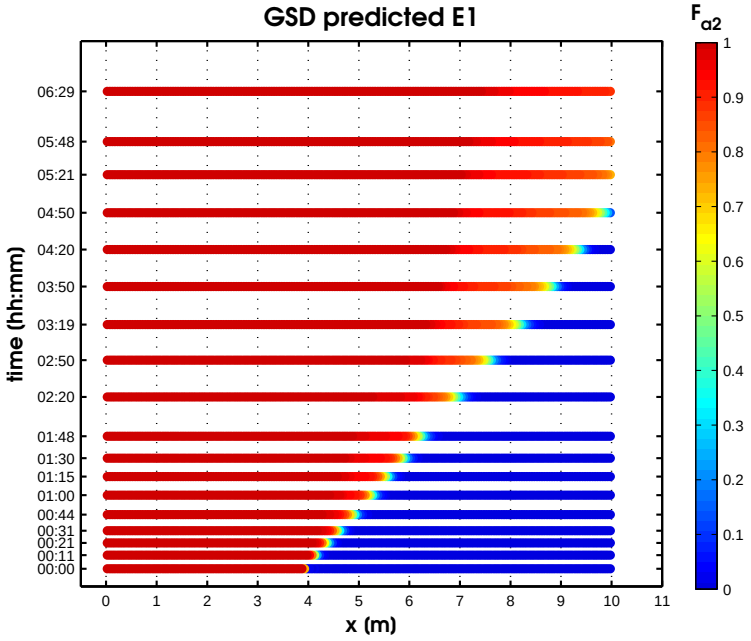

Figure 5.8: Numerical model prediction of the grain size distribution of the bed (volume fraction content in the active layer of the painted fraction, F_{a2}) of Experiment E1

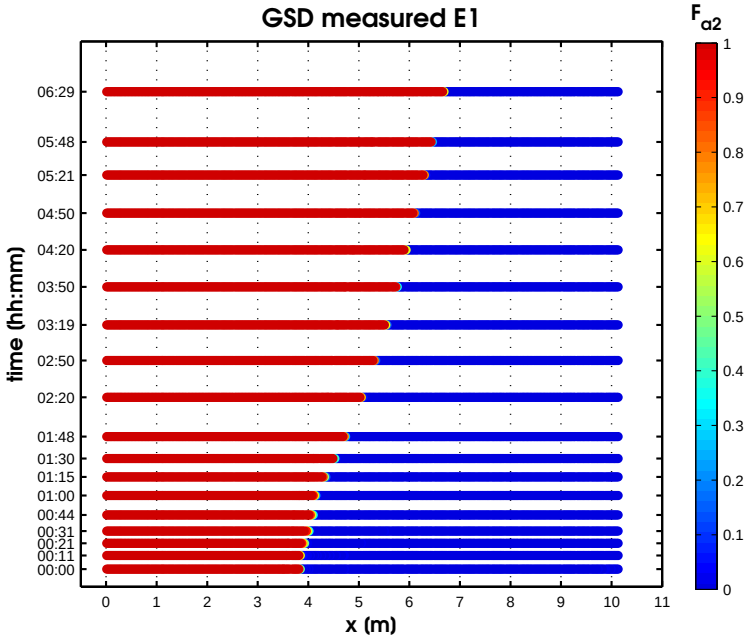

Figure 5.9: Grain size distribution of the bed surface (volume fraction content in the active layer of the painted fraction, F_{a2}) of Experiment E1.

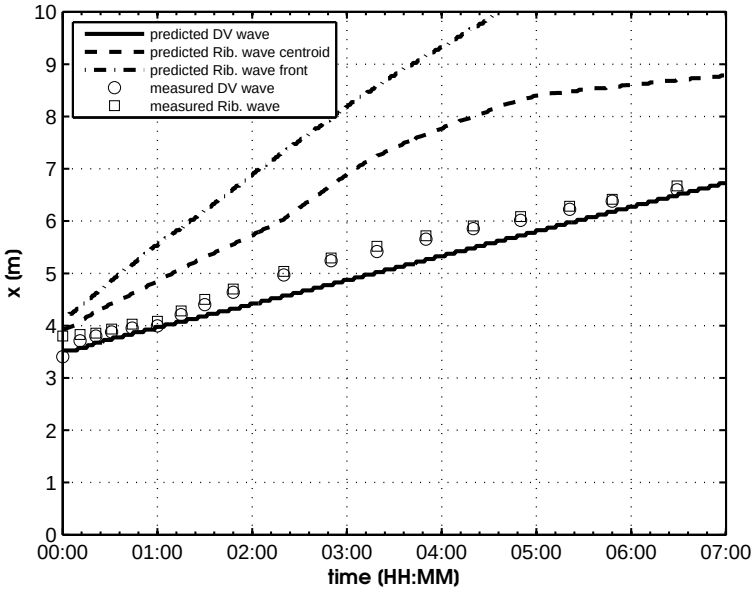

Figure 5.10: x-t diagram of the displacement of the front of the shoal and the Ribberink wave, both the front (dot-dashed line) and the x-coordinate of the centroid for the part where $0 < F_{a2} < 1$, compared to the displacements of the front of the shoal and Ribberink wave of the numerical prediction of the flume experiment. The front of the Ribberink wave travels outside the domain. The steps in the predicted outcomes are the result of having a limited number of grid cells.

the flume experiment which remained in the shoal. The predicted Ribberink wave thus travels faster than the measured Ribberink wave. The numerical model uses the Hirano model for mixed-size sediment, thereby creating a wave of a different sediment fraction, while there is in fact uniform sediment. The Ribberink wave arising in the numerical prediction therefore does not have any physical meaning.

5.4 Predicted results for mixed-size sediment experiment E2

5.4.1 Results

Figure 5.11 shows the predicted bed elevation of the mixed-size sediment experiment E2. The figure shows a clear propagation of the shoal in downstream direction. Near the upstream boundary an area of erosion is present caused by a lack of sediment feed from upstream. Downstream of the shoal front erosion occurs. In both erosional areas the erosion is less than in the flume experiment (Figure 5.12). Figure 5.13 and Figure 5.14 respectively show the predicted and measured bed level relative to the initial bed level.

It is important to note that the numerical model does not reproduce the turbulent recirculation zone that was present in the flume experiment. This means that the erosion both at the upstream end as well as at the area downstream of the front of the shoal is less severe.

Figure 5.15 shows the predicted grain size distribution of the bed in terms of the volume fraction content of the coarsest fraction F_{a2} with time. Figure 5.17 and Figure 5.18 show, respectively, the predicted and measured grain size distribution of the bed relative to the initial grain size distribution. The results show almost no change of the bed grain size distribution compared to the initial bed. This means that the fine fraction is as mobile as the coarse fraction. This is in contrast with the measured grain size distribution of the bed of the flume experiment (Figure 5.16) were a distinct fining of the bed is visible.

The theory of Section 2.3 regarding shoal propagation predicted a coarsening of the bed downstream of the shoal. In the 'high discharge' situation, which applies to this situation, the streamwise increase in flow depth has relatively less effect on sediment transport rates than the streamwise decrease in mean grain size diameter of the bed. This results in a streamwise increase of sediment transport rates, creating a coarsening of the bed. The fining of the bed that occurred in the flume experiment seems to be due to the recirculation zone downstream of the shoal and fining due to dune sorting (Section 4.2.4). In the numerical model, turbulent recirculation is not resolved, which may have been the reason for the fining not to be captured by the model. Also, the active layer thickness L_a set in the numerical computation could play a role in the absence of a change in the grain size distribution of the bed. The active layer thickness was set to the mean bedfrom height, but bed forms did not appear in the predicted results.

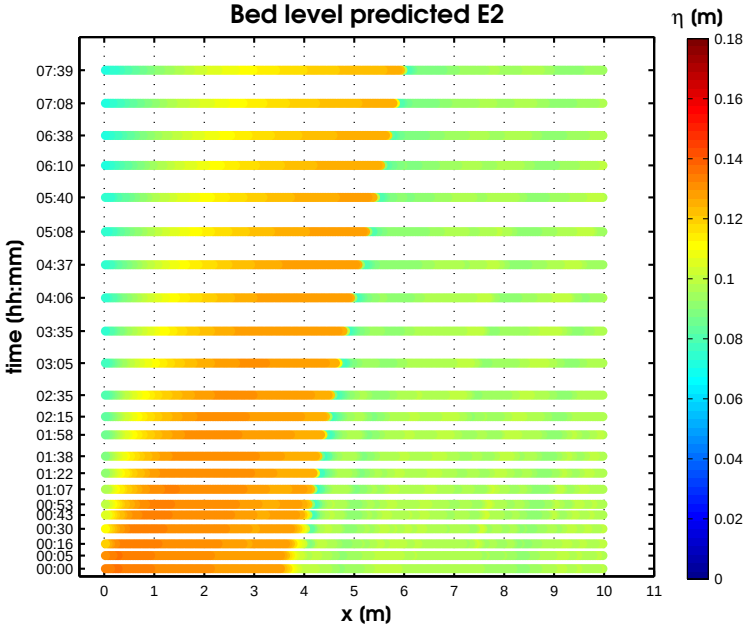

Figure 5.11: Numerical model prediction of the bed level η $[m]$ over time of Experiment E2.

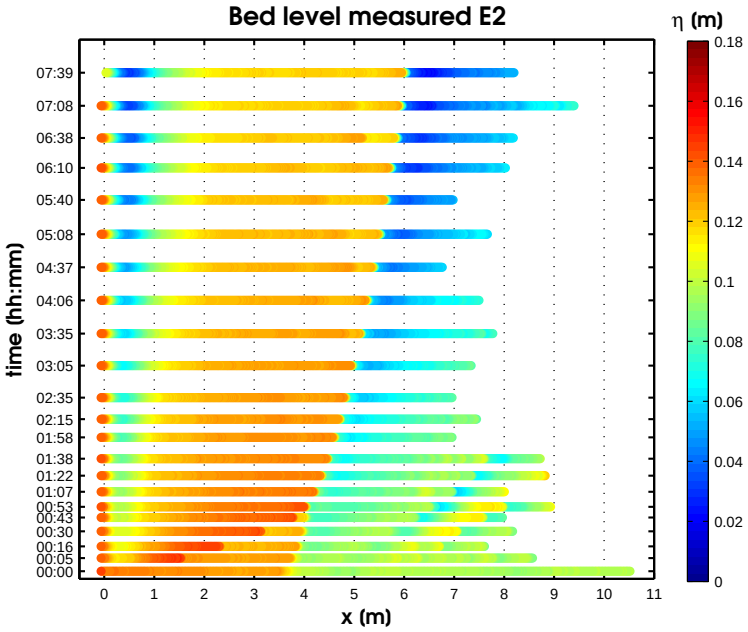

Figure 5.12: Bed level η $[m]$ over time of Experiment E2. Both the propagation of the shoal as well as the erosion downstream of the shoal are well visible. Also the erosion at the upstream boundary is shown. Due to a technical malfunction the bed level profiles were not measured until the end of the flume and differ in length.

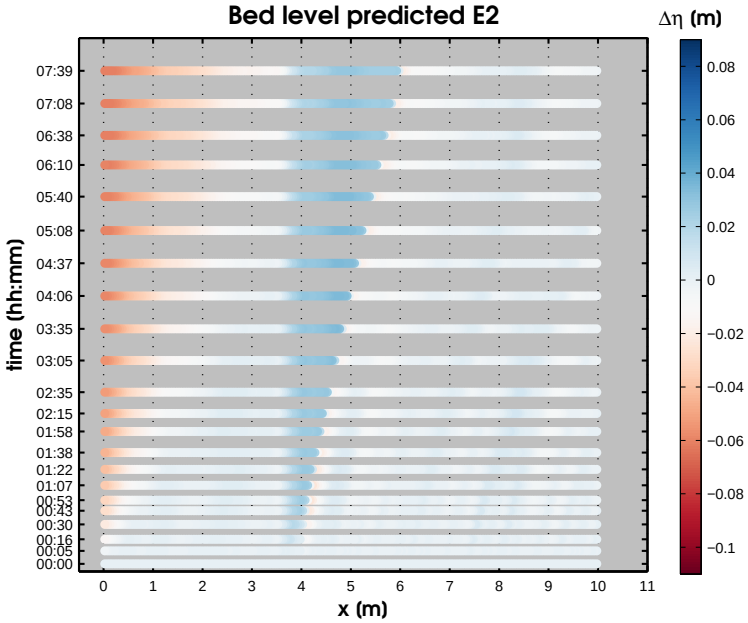

Figure 5.13: Numerical model prediction of the bed level relative to the initial bed level ($\Delta\eta = \eta - \eta_{initial}$ $[m]$) over time of Experiment E2.

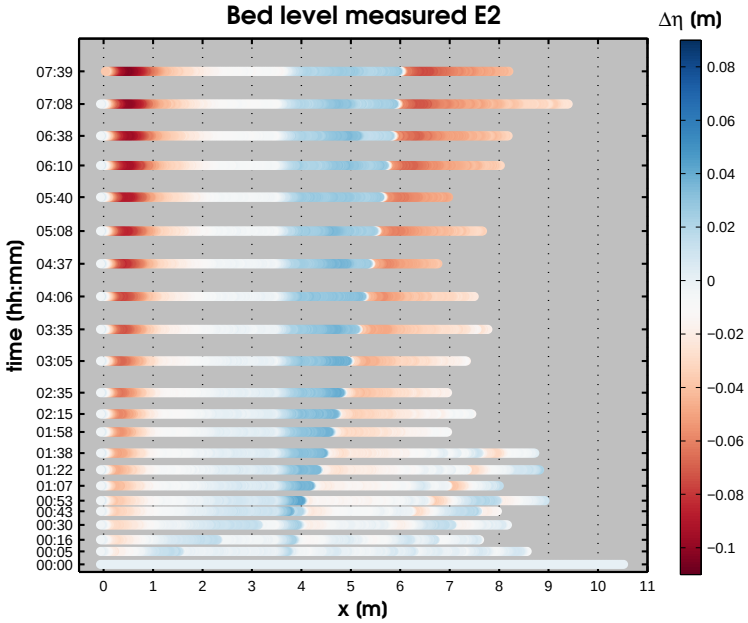

Figure 5.14: Bed level relative to the initial bed level $\Delta\eta = \eta - \eta_{initial}$ $[m]$ over time of Experiment E2. Both the propagation of the shoal as well as the erosion downstream of the shoal are well visible. Due to a technical malfunction the bed level profiles were not measured until the end of the flume and differ in length.

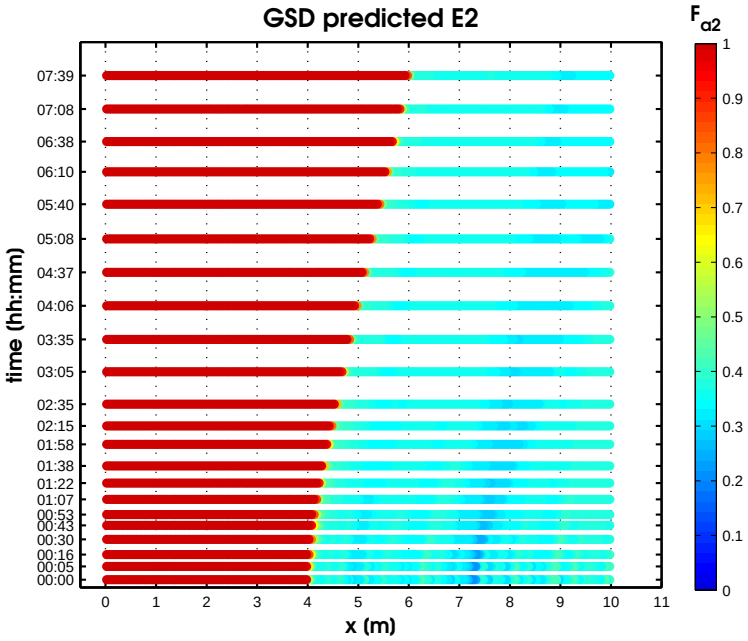

Figure 5.15: Numerical model prediction of the grain size distribution of the bed (volume fraction content in the active layer of the painted fraction, F_{a2}) of Experiment E2.

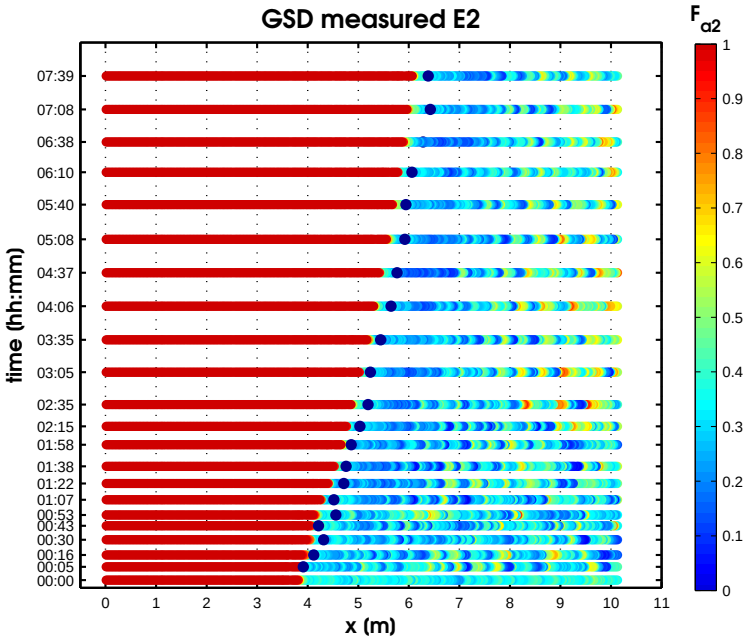

Figure 5.16: Grain size distribution of the bed (volume fraction content in the active layer, F_{a2}) in Experiment E2. A region of fining is well visible downstream of the shoal.

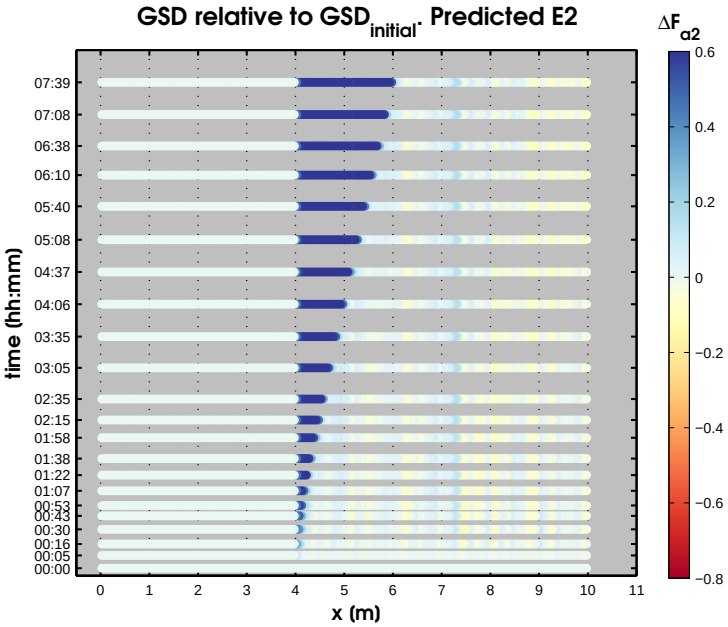

Figure 5.17: Numerical model prediction of the grain size distribution of the bed relative to the initial grain size distribution ($\Delta F_{a2} = F_{a2} - F_{a2,initial}$) of Experiment E2.

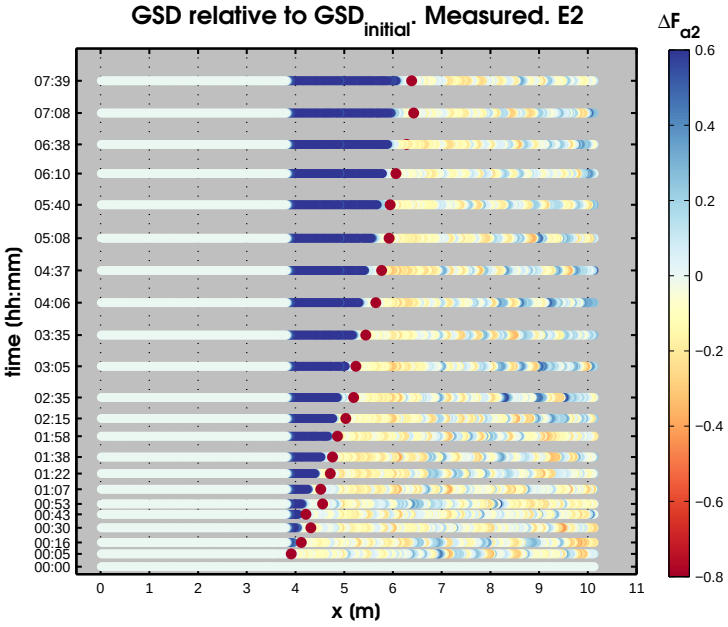

Figure 5.18: Grain size distribution of the bed (volume fraction content in the active layer, F_{a2}) in Experiment E2 relative to the initial grain size distribution. A region of fining is well visible downstream of the shoal. The red dots are the locations of the deepest erosion ($\Delta\eta_{max}$).

5.4.2 Comparison with experimental data

Figure 5.19 shows the x-t diagram containing the displacements of the front of the shoal and Ribberink wave of both the flume experiment E2 and the numerical prediction. In the first place it can be clearly observed that the predicted celerities of De Vries and Ribberink wave, represented by the displacement of the front of the shoal and the largest x-coordinate for which $F_{a2} = 1$, respectively, do not differ. Secondly, Figure 5.10 shows clearly that the predicted displacement of De Vries and Ribberink wave are about the same as the measured displacements with the difference that the measured Ribberink wave is a bit further downstream since it represents the erosional wave downstream of the shoal.

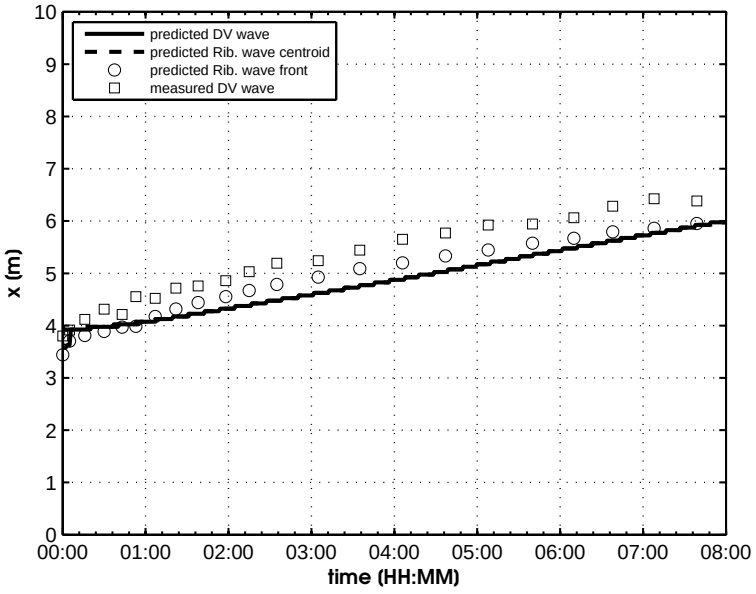

Figure 5.19: x-t diagram of the measured displacement of the front of the shoal and the front of the Ribberink wave (erosional wave) of the mixed-size sediment flume Experiment E2, compared to the displacements of the front of the shoal and Ribberink wave, i.e. largest x-coordinate for which $F_{a2} = 1$, of the numerical prediction of the flume experiment. The steps in the predicted outcomes are the result of having a limited number of grid cells.

5.4.3 Conclusions

It can be concluded that the numerical prediction of the mixed-size sediment experiment (E2) shows a similar transport of the shoal, i.e. De Vries wave, to the flume experiment. Almost no change in bed grain size distribution occurs compared to the initial bed in the numerical prediction of the flume experiment. The predicted Ribberink wave thus travels with the same

celerity as the measured Ribberink wave and does not precedes the De Vries wave. The difference in the evolution of the grain size distribution of the bed in the flume experiment and the numerical reproduction may be due the fact that the numerical model does not resolve the turbulent recirculation zone or that no dunes were present in the numerical outcomes.

5.5 Analytical versus measured and predicted wave celerities

5.5.1 Tracer experiment (E1)

Table 5.2 shows the celerities of the measured De Vries and Ribberink waves compared to the analytical value for these waves and the predicted celerities. The predicted Ribberink wave celerity is defined in two ways : (1) as the celerity of the front of change of grain size distribution, i.e. the front is the most downstream point for which $F_{a2} > 0$, and; (2) as the celerity of the centroid of the wave of change of grain size distribution which is the x-coordinate of the centroid for the part where $0 < F_{a2} < 1$. The celerities of the linear fit are the gradients of a linear fit in through the displacements.

Measured versus analytical celerities

The difference of the De Vries wave celerity of the experiment is about twice as high as the analytical De Vries wave (Equation 2.7). It is important to note that the analytical values by Stecca and Ribberink are linearised and inviscid (neglecting the frictional source terms in the momentum equation), which is valid because they only apply to small perturbations. This implies that the solutions only apply to waves that develop and propagate over short time and length scales (a few seconds and meters, Stecca et al., 2014). The difference between the measured and analytical celerities can be explained by this, since the experiment is a friction dominated situation, where the friction suppresses the bed perturbation wave celerity and the propagating shoal, which is in fact the De Vries wave, is not a small perturbation.

The analytical celerities by Ribberink (1987) and Stecca et al. (2014) for the Ribberink wave are the same. The celerity of Ribberink describes the celerity of the disturbance of the average diameter of the mixture (Equation 2.9) and Stecca's celerity describes the celerity of the wave per size fraction (Equation 2.13). Since in a uniform sediment case the fraction diameter equals the average diameter, both celerities are the same.

The measured celerities of the Ribberink wave are an order $O(10)$ smaller than the analytical Ribberink wave celerities. Again the explanation can be found in the linearisation and inviscidness of the analytical solutions. Thereby the active layer thickness is highly influential for the outcome of the analytical solution — the active layer thickness is inversely proportional to the Ribberink wave celerity — and in this case set to $L_a = 2\overline{d_{90}}$. Since the analytical celerity is higher than the experimental celerity, one might argue to increase the active layer thickness in the analytical model. However the active layer thickness then becomes too large to fulfil the requirements set by Parker (2004): $L_a = n_a d_{90}$, with n_a ranging from 1–2.

Analytical versus numerical celerities
The analytical celerity of the De Vries wave is about twice as high as the measured De Vries wave celerity. This can be explained by the linearised and inviscid analytical approximations as mentioned in above paragraph. The analytical Ribberink wave celerities are almost the same as the numerical celerity. Since for both solutions the same transport model and active layer thickness is used the results do not differ much. The numerical model does take non-linearities into account, but they do not play a role in this case since no bed elevation changes occur downstream of the shoal.

Measured versus numerical celerities
As mentioned in Section 5.3, the measured and predicted celerities do not differ. The measured Ribbberink wave is slower than the predicted Ribberink wave celerity. The difference in the front and centroid celerity of the numerical outcomes shows the spreading of the shoal material over the bed downstream of the shoal.

Table 5.2: Measured celerities of De Vries wave and Ribberink wave in Experiment E1, the tracer sediment experiment, together with the analytical celerity according to Ribberink (1987) and Stecca et al. (2014) (Section 2.1.2) and the celerities from the numerical predictions. For the analytical sorting wave celerities, an active layer thickness of $L_a = 2\overline{d_{90}} = 5.0\ mm$ is used. Celerities in ms^{-1}.

		Celerities	
		De Vries wave	Ribberink wave
Experiment	Linear fit	1.37E-04	1.32E-04
Analytical	Ribberink Stecca	2.59E-04	2.00E-03 2.00E-03
Numerical	Linear fit	1.28E-04	2.10E-04 (centroid) 2.30E-04 (front)

5.5.2 Mixed-size sediment experiment (E2)

Table 5.3 shows the celerities of the De Vries wave (shoal) and Ribberink wave (location of maximum erosion downstream of the shoal) of the experiment, together with the analytical values for these waves by Ribberink (1987) and Stecca et al. (2014) and the predicted celerities. The celerities of the linear fit are the gradients of a linear fit in through the displacements.

Measured versus analytical celerities
The analytical celerities of the De Vries wave are more or less the same as the measured De Vries wave celerities.

The measured celerities for the Ribberink wave are about twice as low as the analytical celerities. This can be explained by the fact that the

analytical solutions are linear, while non-linear effect occur in the flume experiments, due to the interaction of the change of grain size distribution of the bed with the change of bed level. A larger active layer thickness in the analytical model would result in a smaller Ribberink wave celerity.

Analytical versus numerical celerities
The numerical De Vries wave celerity is almost the same as the analytical De Vries wave celerity, but the numerical celerity is slightly slower. The numerical Ribberink wave celerity is of the order $O(10)$ smaller than the analytical Ribberink wave celerities. Both solutions use the same transport model and active layer thickness but the analytical model does not take into account non-linear effects, which do play a role in the flume experiment and can explain the order of difference.

Measured versus numerical celerities
As mentioned in Section 5.4.2 the numerical wave celerities for both the De Vries wave as the Ribberink wave do not differ much from measured wave celerities.

Table 5.3: Celerities of measured De Vries wave and Ribberink wave in Experiment E2, the mixed-size sediment experiment, together with the analytical celerities according to Ribberink (1987) and Stecca et al. (2014) (Section 2.1.2) and the celerities from the numerical predictions. For the analytical sorting wave celerities, an active layer thickness of $L_a = 0.03\ m$ is used. Celerities in ms^{-1}.

		Celerities	
		De Vries wave	Ribberink wave
Experiment	Linear fit	8.60E-05	8.49E-05
Analytical	Ribberink	8.70E-05	1.49E-04
	Stecca		1.77E-04
Numerical	Linear fit	7.67E-05	7.52E-05

6 | Conclusions and recommendations

6.1 Conclusions

River beds are sometimes protected from degradation by a nourishment of sediment material. Laboratory experiments have been conducted to gain insight in the behaviour of such nourishments and more general to study the behaviour of a river bed mixed-size (bimodal) sediment in a physical, controlled environment. In detail the behaviour and celerities of the arising De Vries an Ribberink wave have been studied. De Vries and Ribberink waves have been also been studied in a tracer experiment, where grain-size-selective processes where avoided/dismissed. For that purpose a series of two experiments have been conducted, in both installing a shoal from the upstream end, with one experiment with unisize sediment in which the shoal material was coloured to act as a tracer (Experiment E1) and one experiment with bimodal sediment (Experiment E2). Numerical predictions of the experiments have been made.

6.1.1 Uniform sediment (tracer)

In the experiment with uniform sediment, the tracer experiment (E1), the shoal propagated in downstream direction. Also no change in tracer content and bed level was observed downstream of the shoal.

The De Vries wave and Ribberink wave corresponding with the sediment of the shoal (blue painted) did not show any difference in transport celerity. This means that none of the tracer sediment from the shoal travelled further than the shoal.

It can be concluded that the numerical prediction of the tracer experiment (E1) shows a similar transport of the shoal, i.e. De Vries wave, to the flume experiment. In the numerical predictions the tracer material travels over and further than the front of the shoal, as opposed to the tracer material in the flume experiment which remained in the shoal. The predicted Ribberink

wave thus travels faster than the measured Ribberink wave. The numerical model uses the Hirano model for mixed-size sediment, thereby creating a wave of a different sediment fraction, while there is in fact uniform sediment. The Ribberink wave arising in the numerical prediction therefore does not have any physical meaning.

6.1.2 Mixed-size sediment

In the mixed-size sediment experiment E2, the shoal propagated in downstream direction, with the front of the shoal increasing in height (relative to the bed) giving rise to a turbulent recirculation zone downstream of the shoal. This turbulent recirculation seems to have caused the transport of fine material back in upstream direction causing the bed downstream of the shoal to become finer with time. Turbulent bursts and sweeps also seems to have caused the finer material to be entrained more easily by the flow and cover the coarser material downstream of the point of reattachment of the turbulent shear layer, resulting in a fining of the bed. In addition to that the fining of the bed could also have been caused by the vertical sorting over the bed forms arising in the bed from the start of the experiment, causing the coarser material to be moved down and fine the top layer of the bed.

It can be concluded that the numerical prediction of the mixed-size sediment experiment (E2) shows a similar transport of the shoal, i.e. De Vries wave, to the flume experiment. Almost no change in bed grain size distribution occurs compared to the initial bed in the numerical prediction of the flume experiment. The predicted Ribberink wave thus travels with the same celerity as the measured Ribberink wave and does not precedes the De Vries wave. The difference in the evolution of the grain size distribution of the bed in the flume experiment and the numerical reproduction may be due the fact that the numerical model does not resolve the turbulent recirculation zone or that no dunes were present in the numerical outcomes.

6.1.3 General

In general, relating back to the premisses of the Introduction concerning river nourishments and model predictions for river safety, the conclusions of this thesis show that the grain size distribution of the nourished material is of great influence on the propagation of the nourished material and on bed level changes downstream of the nourishment. As concluded from the flume experiments, when the nourished material (a hump similar to the shoal of the conducted experiments in this thesis) is coarser than the river bed, an erosional wave downstream of the nourishment will arise, travelling with the same celerity as the nourished material. If the nourishment is done to protect or counteract river bed degradation, this erosional effect caused by

the shoal should be considered seriously.

The Iffezheim case, discussed in Section 2.2, shows the dispersive character of different grain sizes. This is confirmed by the results of the mixed-size sediment experiment although hard conclusions have to be avoided since there was a lack of incoming sediment from upstream and the therewith related erosion on the shoal could have influenced the dispersive character.

In practise, numerical models are used to predict river bed changes to design protection measures. When using Hirano's conservation model for mixed-size sediment, the active layer thickness is still a great unknown and difficult to predict beforehand. Since the experimental results show that the Ribberink wave travels with the same celerity as the De Vries wave, it might be possible in practical uses of numerical models to tune the active layer thickness such that both waves travel together.

6.2 Recommendations

When conducting further experiments to investigate the physical behaviour of Ribberink waves and to improve the experiments conducted in this thesis, the following things are recommended to be taken into account:

When performing a mixed-size sediment experiment as in our case, i.e. with a bimodal sediment mixture, it is recommended to use different colour coarse sediment in bed and shoal to distinct between sediment coming from the shoal or from the original bed. Especially when a coarsening of the bed downstream of the shoal occurs it can be proven where this coarse material had come from.

To use a numerical model that resolves the turbulence so that the effect of the recirculation zone downstream of the shoal can cause the erosion as it was seen in the flume experiment and allows the study of the influence of the erosional area on the changes in grain size distribution of the bed in a numerical model.

Bibliography

Berkhout, B. (**2014**). *The Importance of Being Sorted: A numerical study into the behaviour of Hirano's sorting waves.* Additional thesis, Delft University of Technology.

Blom, A. (**2008**). "Different approaches to handling vertical and streamwise sorting in modeling river morphodynamics." *Water Resources Research*, 44(3): n/a–n/a. URL `http://dx.doi.org/10.1029/2006WR005474`.

Blom, A., Ribberink, J. S., and de Vriend, H. J. (**2003**). "Vertical sorting in bed forms: Flume experiments with a natural and a trimodal sediment mixture." *Water Resources Research*, 39(2): n/a–n/a. URL `http://dx.doi.org/10.1029/2001WR001088`.

Bradshaw, P. and Wong, F. (**1972**). "The reattachment and relaxation of a turbulent shear layer." *Journal of Fluid Mechanics*, 52: 113–135. URL `http://journals.cambridge.org/article_S002211207200299X`.

Brodkey, R. S., Wallace, J. M., and Eckelmann, H. (**1974**). "Some properties of truncated turbulence signals in bounded shear flows." *Journal of Fluid Mechanics*, 63: 209–224. URL `http://journals.cambridge.org/article_S0022112074001108`.

De Vries, M. (**1965**). "Considerations about non-steady bed-load transport in open channels." In "Proc. IAHR Leningrad," pages 3.8.1 – 3.8.8. Int. Assoc. for Hydraul. Res.

De Way, M. (**2014**). *Sediment augmentation and the migration of shoals.* Bachelor thesis, Delft University of Technology.

Dumbser, M. and Toro, E. (**2011**). "A simple extension of the Osher Riemann solver to non-conservative hyperbolic systems." *Journal of Scientific Computing*, 48: 70–88.

Egiazaroff, V. I. (**1965**). "Calculation of non-uniform sediment concentrations." *J. of Hydr. Div., ASCE*, 91(HY4).

Fennis, F. (**2013**). *Sediment nourishment in the Dutch Rhine*. Bachelor thesis, Delft University of Technology.

Gölz, E. (**2002**). "Iffezheim field test — three years experience with a petrographic tracer." In "The Structure, Function and Management Implications of Fluvial Sedimentary Systems (Proc. Alice Springs Symp)," 276.

Gölz, E., Theis, H., and Trompeter, U. (**2006**). *Tracerversuch Iffezheim*. Report bfg-1530, Bundesanstalt für Gewässerkunde (BFG) and Wasser- und Schiffahrtsamt Freiburg (WSA).

Hirano, M. (**1971**). "River bed degradation with armoring." *Transaction Japanese Society Civil Engineering*, 3: 194–195.

Hirano, M. (**1972**). "Studies on Variation and Equilibrium State of a River Bed Composed of Non-uniform Material." *Transaction Japanese Society Civil Engineering*, 4: 128–129.

Kim, J., Kline, S. J., and Johnston, J. P. (**1980**). "Investigation of a Reattaching Turbulent Shear Layer: Flow Over a Backward-Facing Step." *Journal of Fluids Engineering*, 102(3): 302–308. URL `http://dx.doi.org/10.1115/1.3240686`.

Lyn, D. and Altinakar, M. (**2002**). "St. Venant–Exner Equations for Near-Critical and Transcritical Flows." *Journal of Hydraulic Engineering*, 128(6): 579–587. URL `http://dx.doi.org/10.1061/(ASCE)0733-9429(2002)128:6(579)`.

Maso, G. D., Floch, P. L., and Murat, F. (**1995**). "Definition and weak stability of nonconservative products." *Journal de Mathematiques pures et appliques*, 74(6): 483–548.

Meyer-Peter, E. and Müller, R. (**1948**). "Formulas for bed-load transport." In "Proceedings of second Congress IAHR," 2, pages 39–64. Stockholm.

Mosselman, E. and Sloff, K. (**2007**). "The importance of floods for bed topography and bed sediment composition: numerical modelling of Rhine bifurcation at Pannerden." In "Gravel-Bed Rivers VI: From Process Understanding to River Restoration," volume 11 of *Developments in Earth Surface Processes*, pages 161 – 179. Elsevier. URL `http://www.sciencedirect.com/science/article/pii/S092820250711124X`.

Mosselman, E., Sloff, K., and Van Vuren, S. (**2008**). "Different sediment mixtures at constant flow conditions can produce the same celerity of bed disturbances." In "River Flow 2008: Proceedings of the International Conference of Fluvial Hydraulics," pages 1373–1377.

Orrú, C., Chavarrías, V., Uijttewaal, W. S. J., and Blom, A. (**2014**). "Image analysis for measuring the size stratification in sand-gravel laboratory experiments." *Earth Surface Dynamics*, 2(1): 217–232. URL `http://www.earth-surf-dynam.net/2/217/2014/`.

Parker, G. (**1991**a). "Selective Sorting and Abrasion of River Gravel. I: Theory." *Journal of Hydraulic Engineering*, 117(2): 131–147. URL `http://dx.doi.org/10.1061/(ASCE)0733-9429(1991)117:2(131)`.

Parker, G. (**1991**b). "Selective Sorting and Abrasion of River Gravel. II: Applications." *Journal of Hydraulic Engineering*, 117(2): 150–171. URL `http://dx.doi.org/10.1061/(ASCE)0733-9429(1991)117:2(150)`.

Parker, G. (**2004**). *1D sediment transport morphodynamics with applications to rivers and turbidity currents*. E-book. Online available.

Ribberink, J. (**1987**). *Mathematical modelling of one-dimensional morphological changes in rivers with non-uniform sediment*. Ph.D. thesis, Delft University of Technology, Delft, Netherlands.

Sieben, J. (**1997**). *Modelling of hydraulics and morphology in mountain rivers*. Ph.D. thesis, Delft University of Technology, Delft, Netherlands.

Sloff, K. and Mosselman, E. (**2012**). "Bifurcation modelling in a meandering gravel–sand bed river." *Earth Surface Processes and Landforms*, 37(14): 1556–1566. URL `http://dx.doi.org/10.1002/esp.3305`.

Stecca, G., Siviglia, A., and Blom, A. (**2014**). "Mathematical analysis of the Saint-Venant-Hirano model for mixed-sediment morphodynamics." *Water Resources Research*, 50(10): 7563–7589. URL `http://dx.doi.org/10.1002/2014WR015251`.

Stecca, G., Siviglia, A., and Blom, A. (**submitted**). "An accurate numerical solution to the Saint-Venant-Hirano model for mixed-sediment morphodynamics in rivers." *Submitted to Advances in Water Resources*.

Suzuki, K. (**1976**). *On the propagation of a disturbance in the bed composition of an open channel*. Report r 1976/09/l, Delft Univ. of Thechn., Dept. of Civil Eng., lab. of Fluid Mechanics.

Toro, E. and Titarev, V. (**2002**). "Solution of the generalized Riemann problem for advection-reaction equations." In "Proceedings of the Royal Society of London Series A. Mathematical Physical and Engineering Sciences," 485(2018), pages 271—281.

Weichert, R. B., Wahrheit-Lensing, A., Frings, R. M., Promny, M., and Vollmer, S. (**2010**). "Morphological characteristics of the river Rhine between Iffezheim and Bingen." In "River Flow 2010," volume 1, pages 1077–1084. Braunschweig, Germany.

A | Iffezheim field case data

A.1 Grain size distributions per date

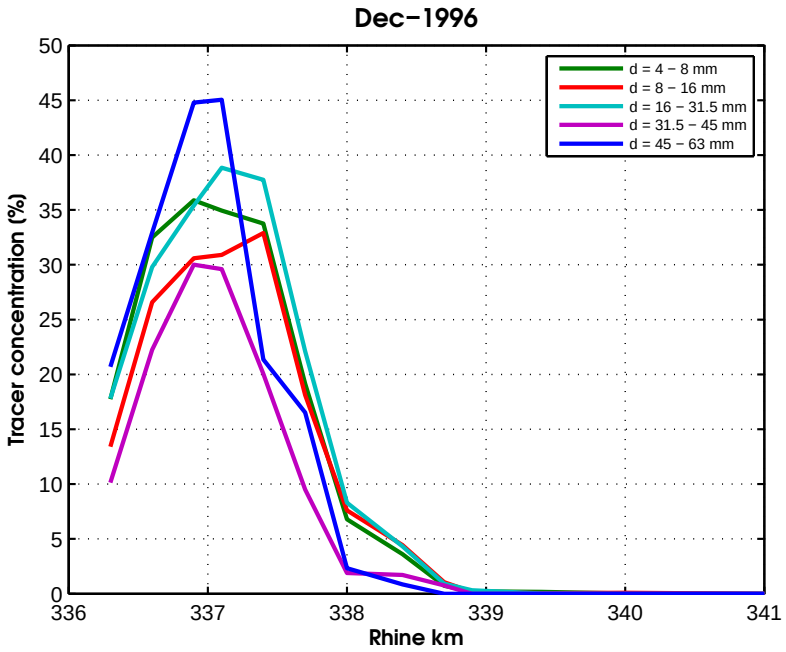

Figure A.1: Distribution of all fractions over longitudinal direction.

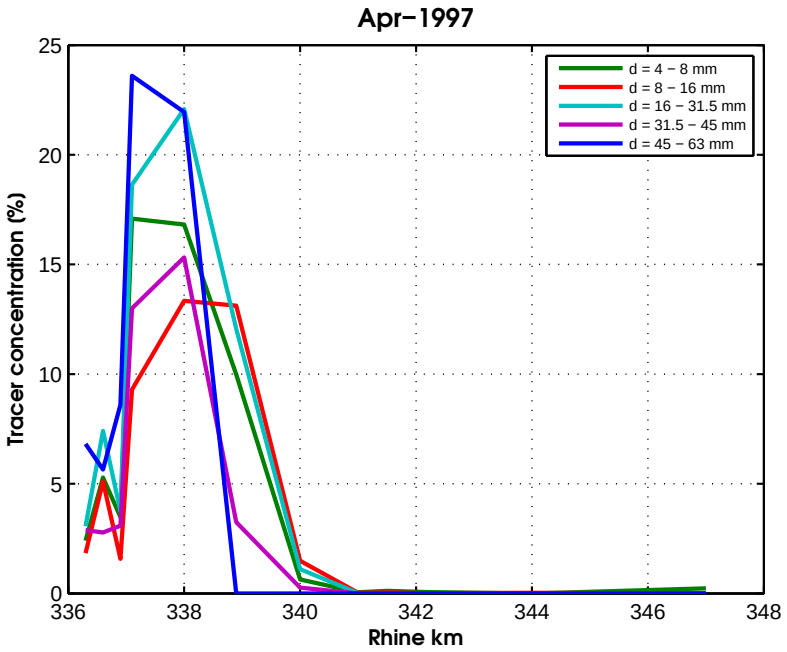

Figure A.2: Distribution of all fractions over longitudinal direction.

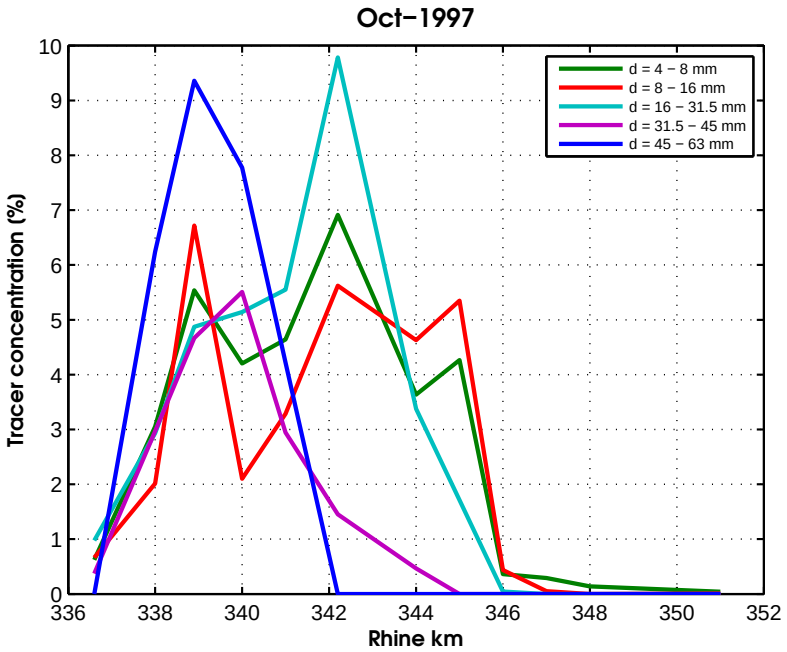

Figure A.3: Distribution of all fractions over longitudinal direction.

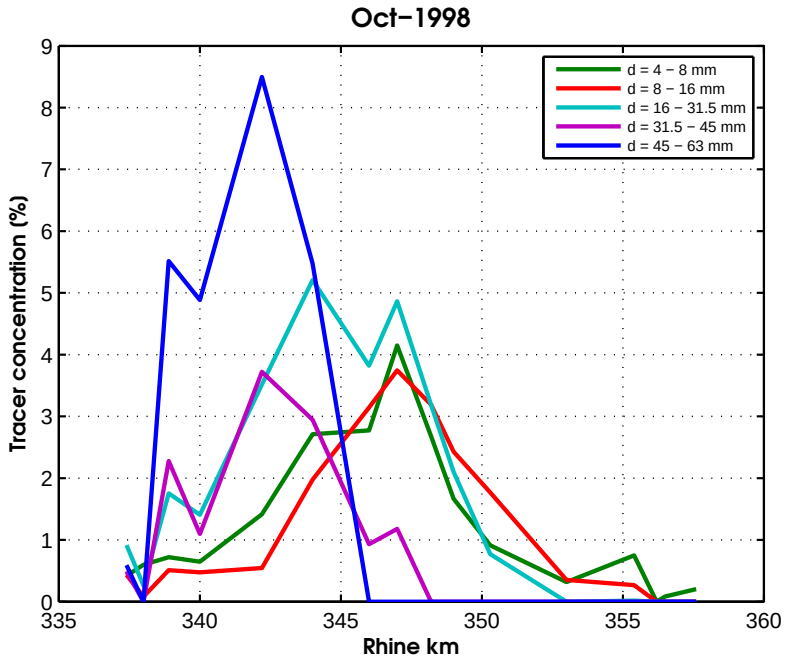

Figure A.4: Distribution of all fractions over longitudinal direction.

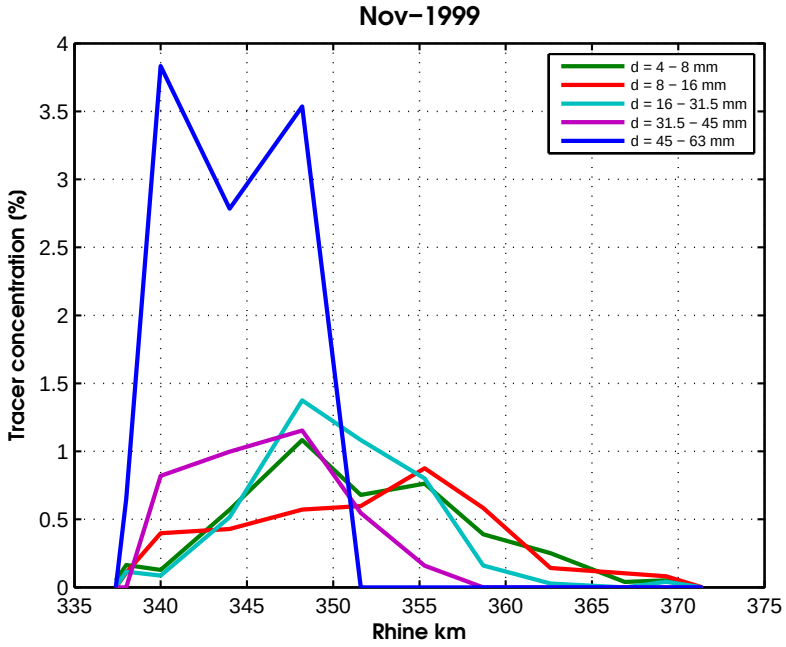

Figure A.5: Distribution of all fractions over longitudinal direction.

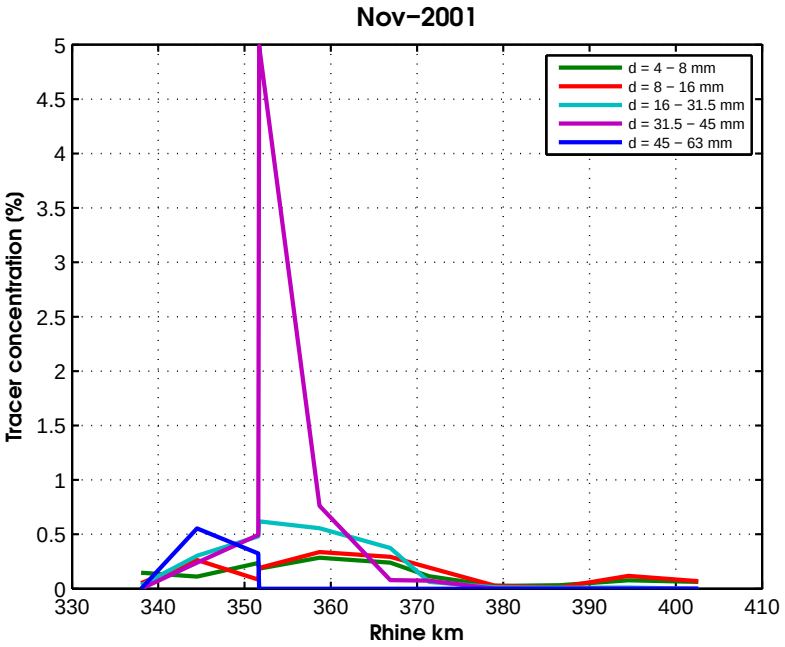

Figure A.6: Distribution of all fractions over longitudinal direction.

A.2 Grain size distributions per fraction

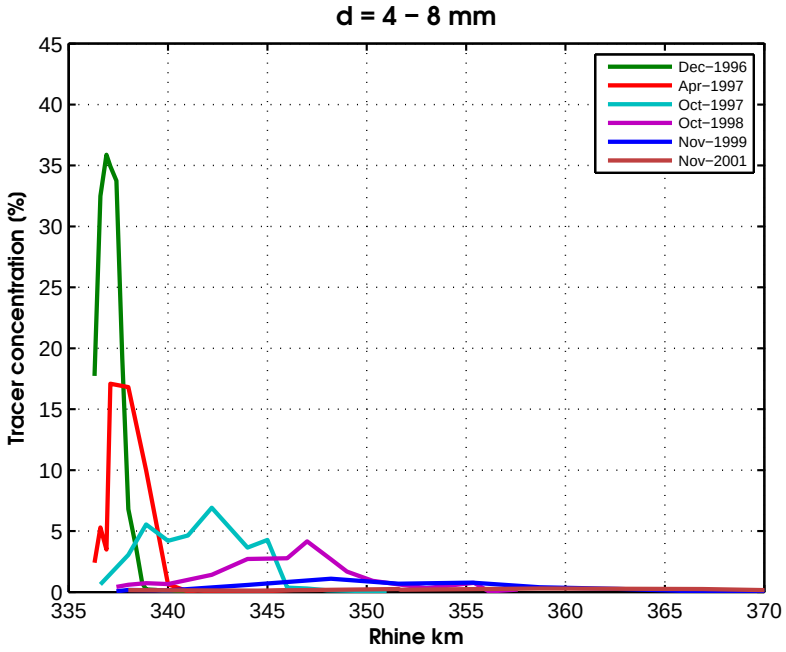

Figure A.7: Distribution of one fractions for each sampling time.

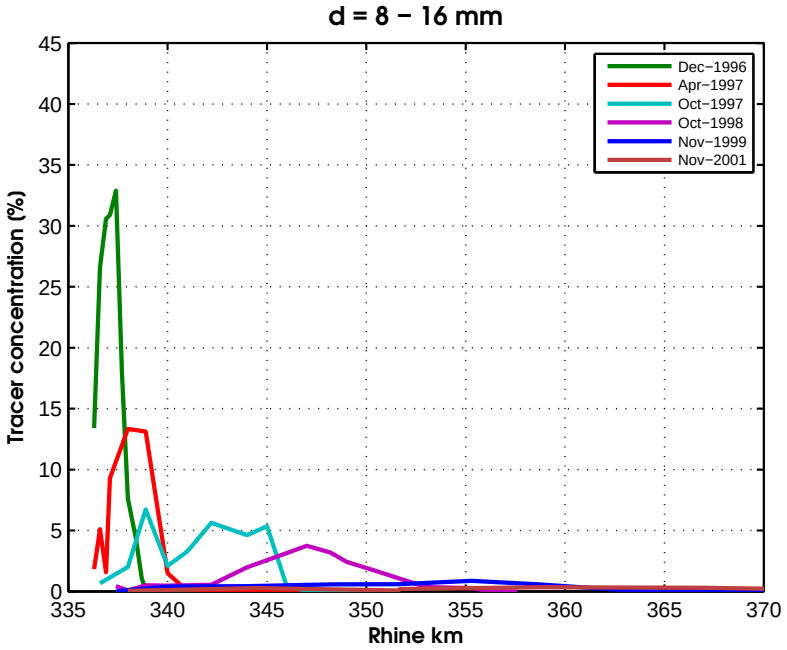

Figure A.8: Distribution of one fractions for each sampling time.

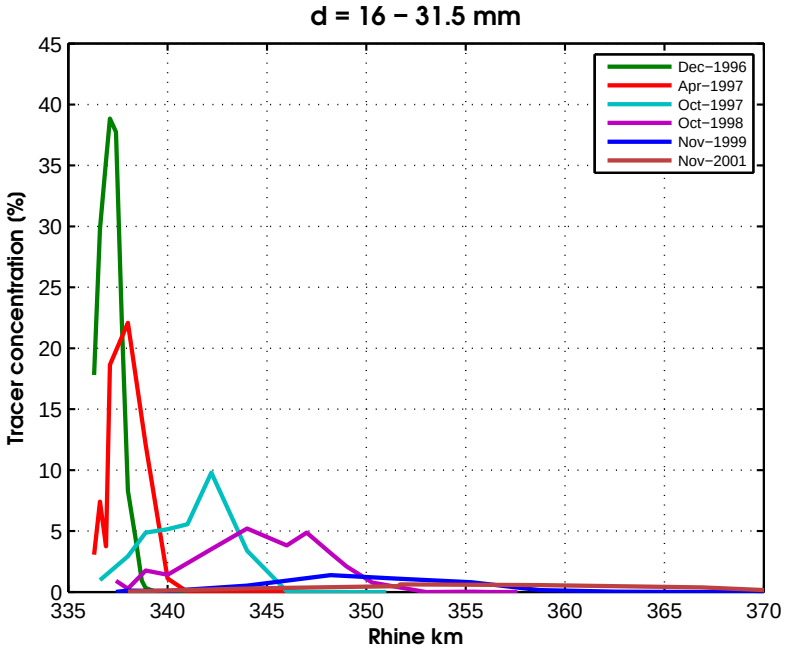

Figure A.9: Distribution of one fractions for each sampling time.

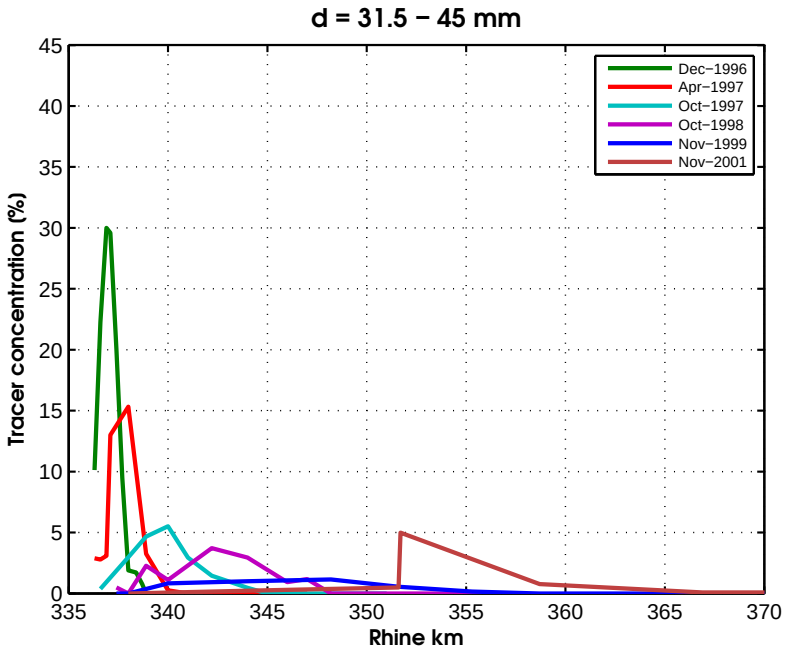

Figure A.10: Distribution of one fractions for each sampling time.

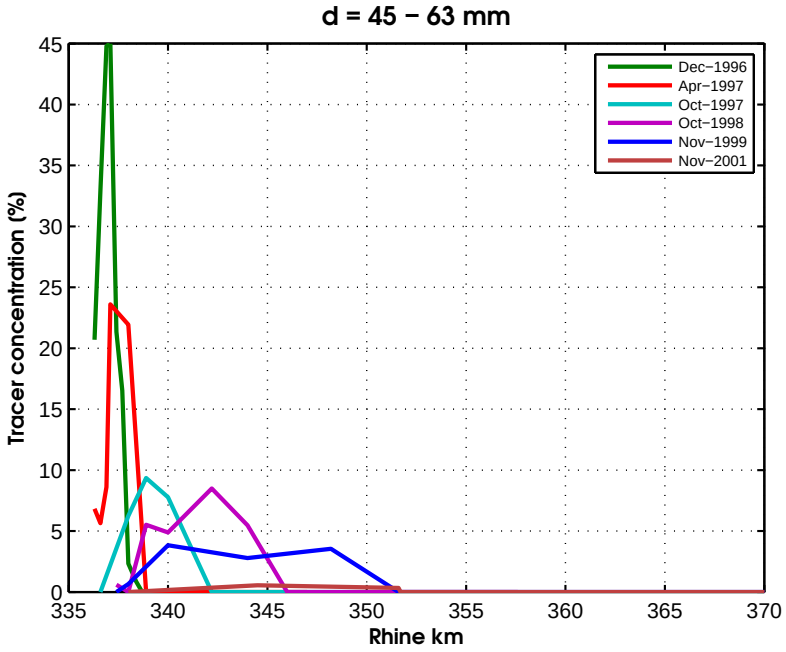

Figure A.11: Distribution of one fractions for each sampling time.

B | Profiles of bed and water level and grain size distribution of bed surface in Experiment E2

Profiles of, top panel: bed level (black) and water level (blue) and bottom panel: grain size distribution in terms of volume fraction content of the coarsest fraction F_{a2}. The vertical dashed line in both the upper and lower panel shows the largest x-coordinate for which $F_{a2} = 1$. Time in the title of the figures are in $[hhmm]$.

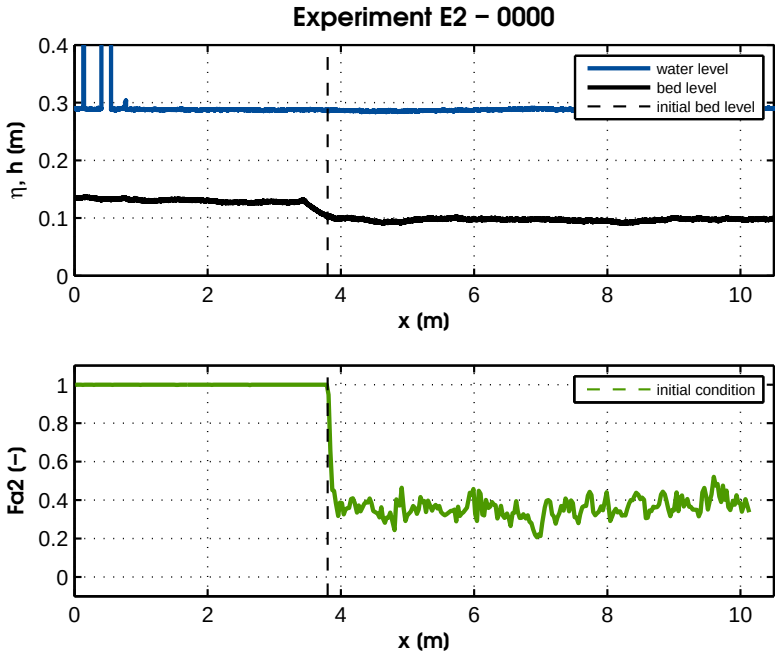

Figure B.1

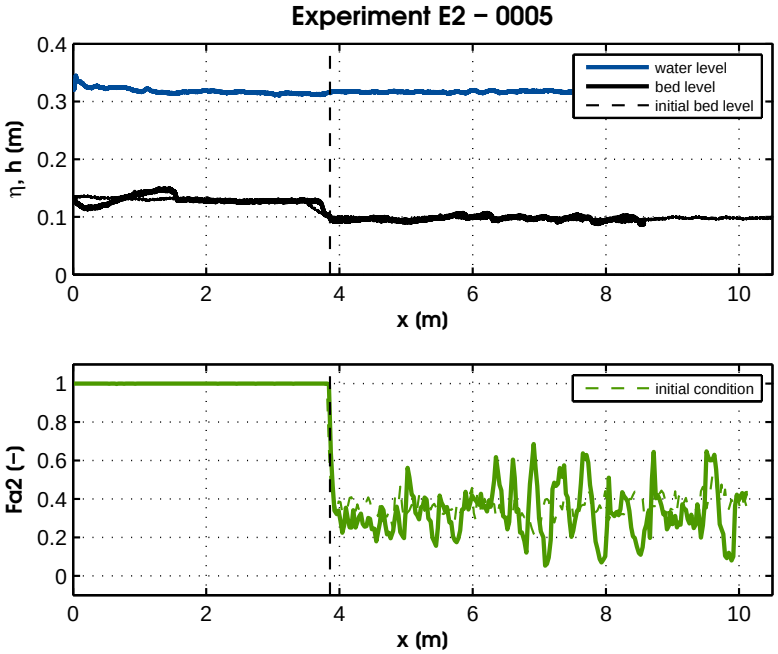

Figure B.2

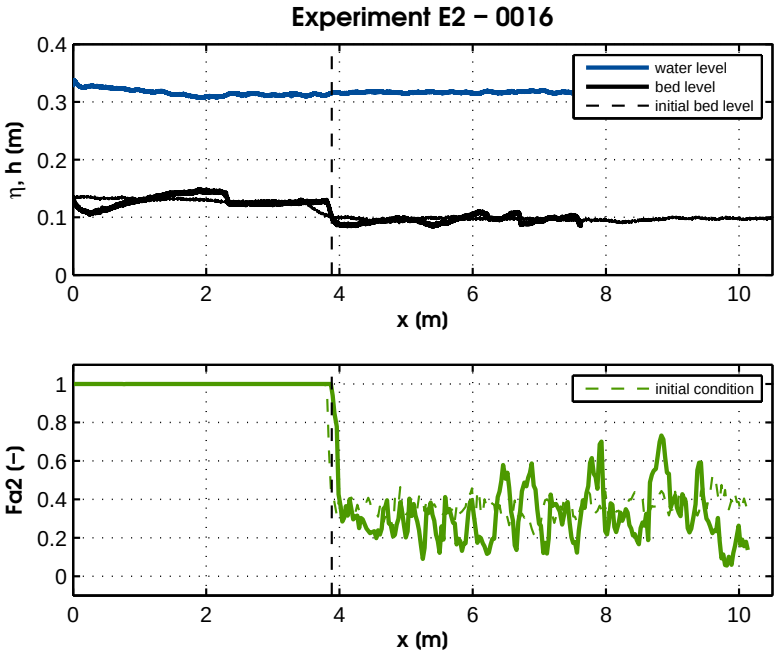

Figure B.3

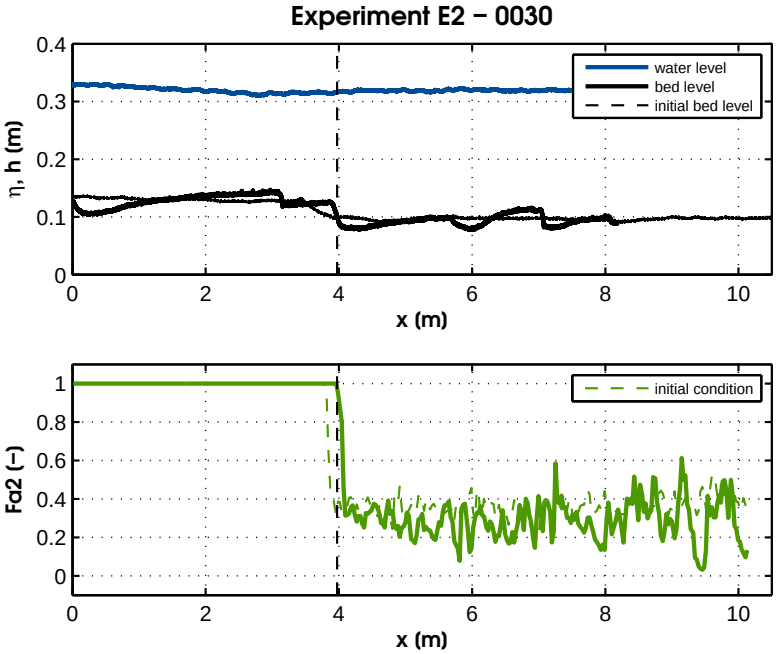

Figure B.4

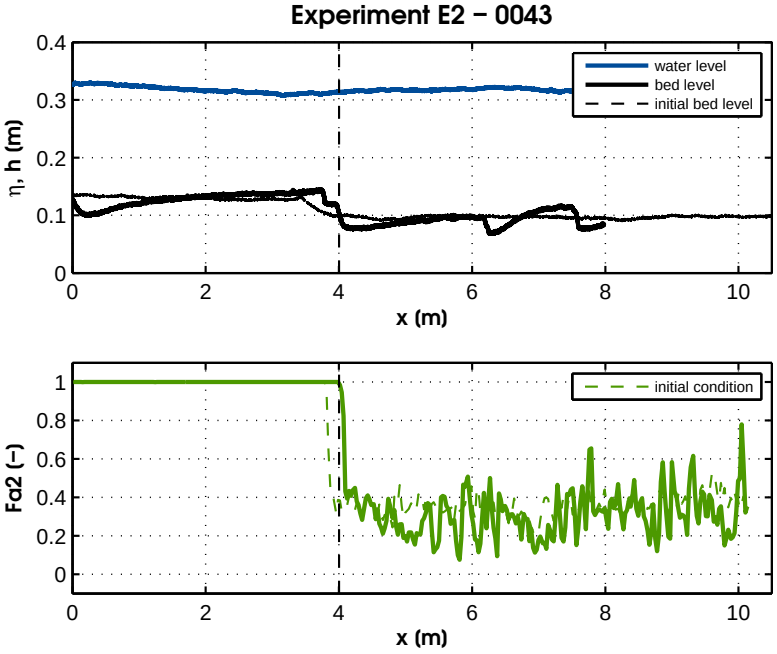

Figure B.5

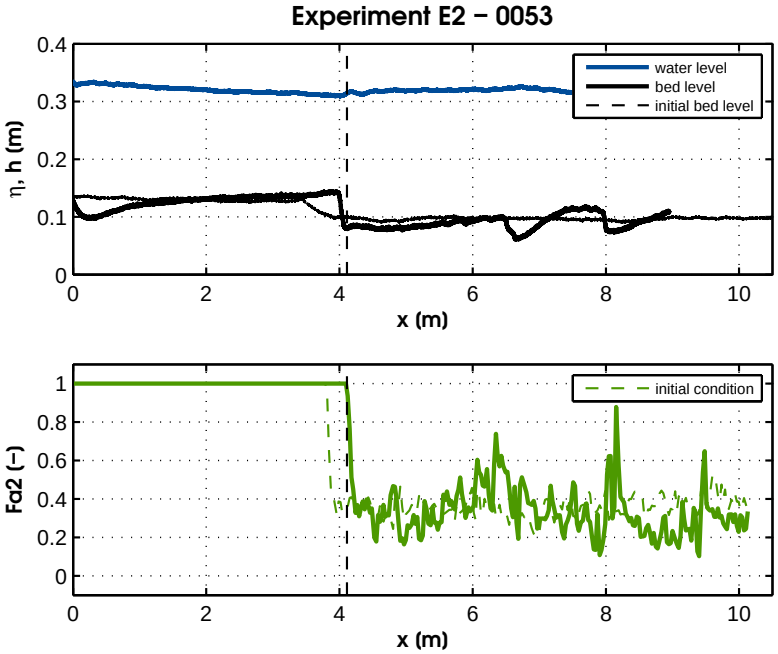

Figure B.6

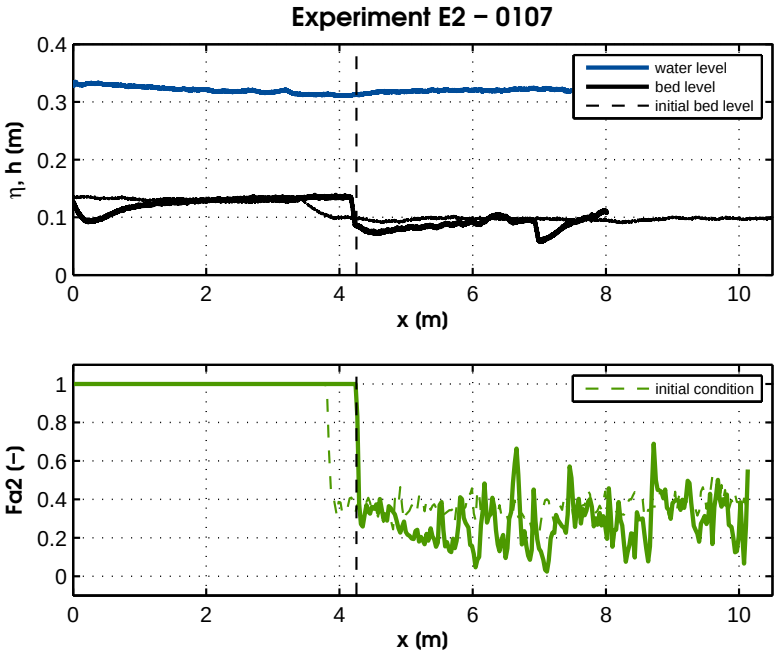

Figure B.7

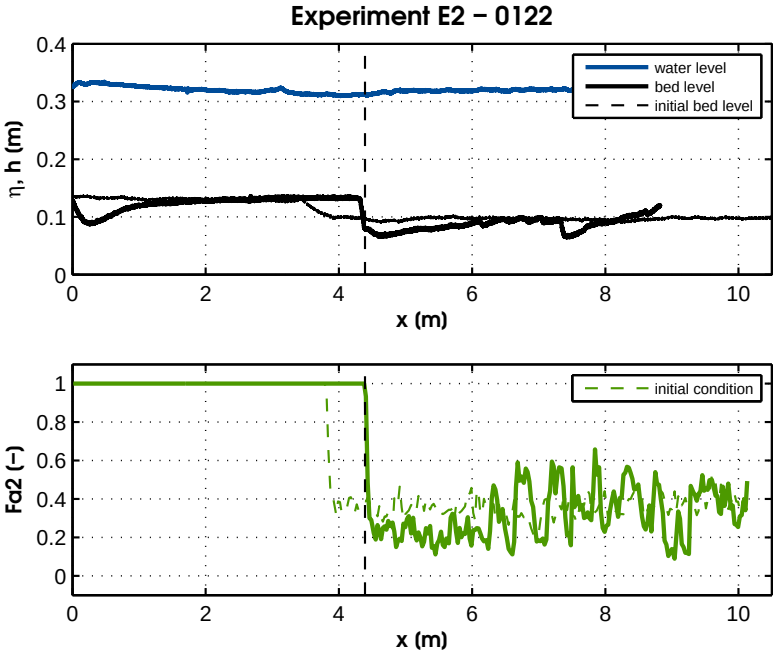

Figure B.8

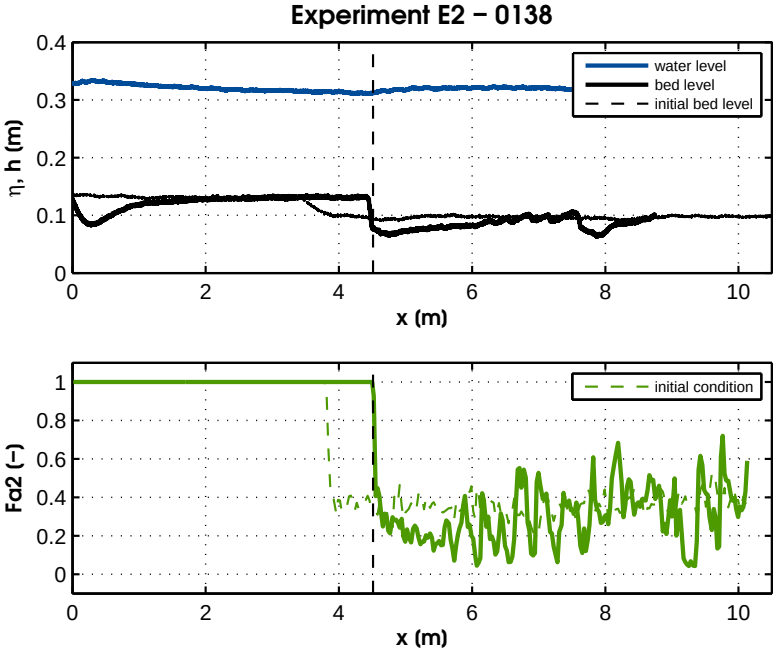

Figure B.9

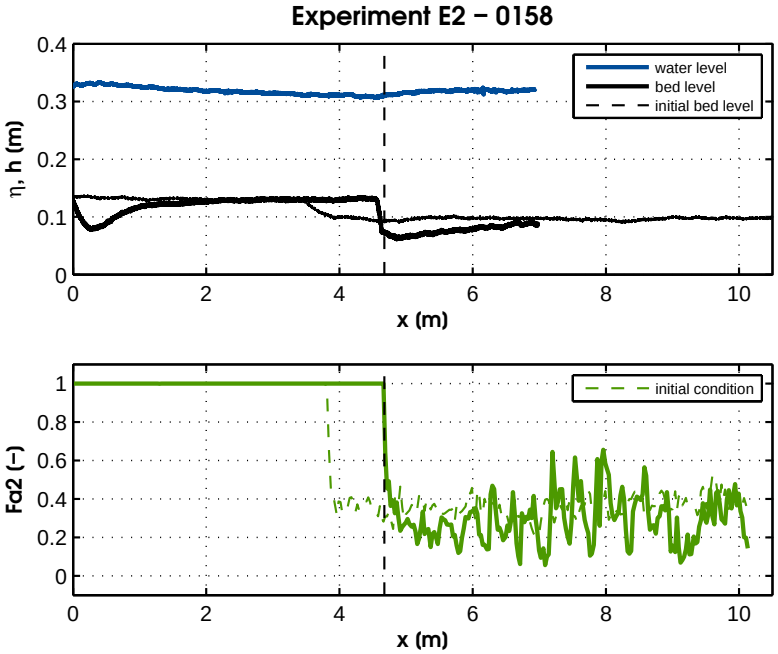

Figure B.10

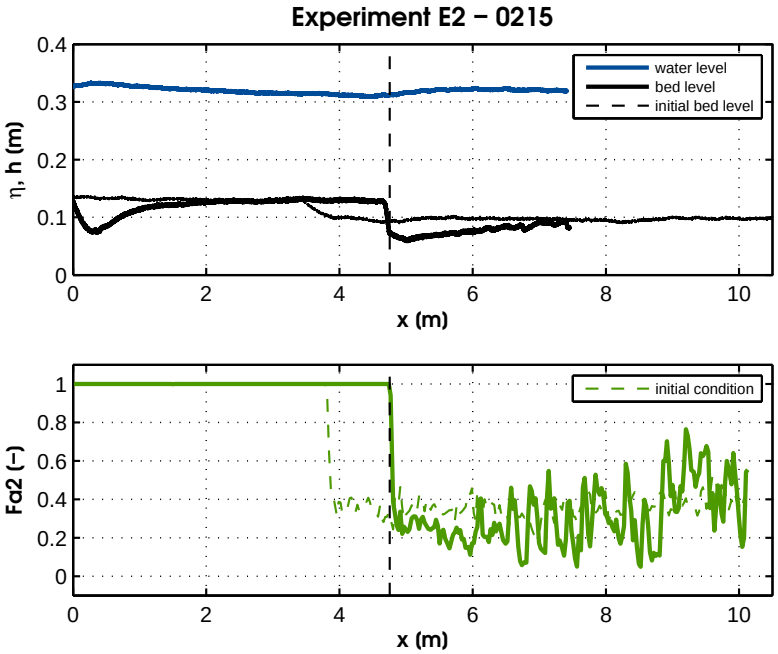

Figure B.11

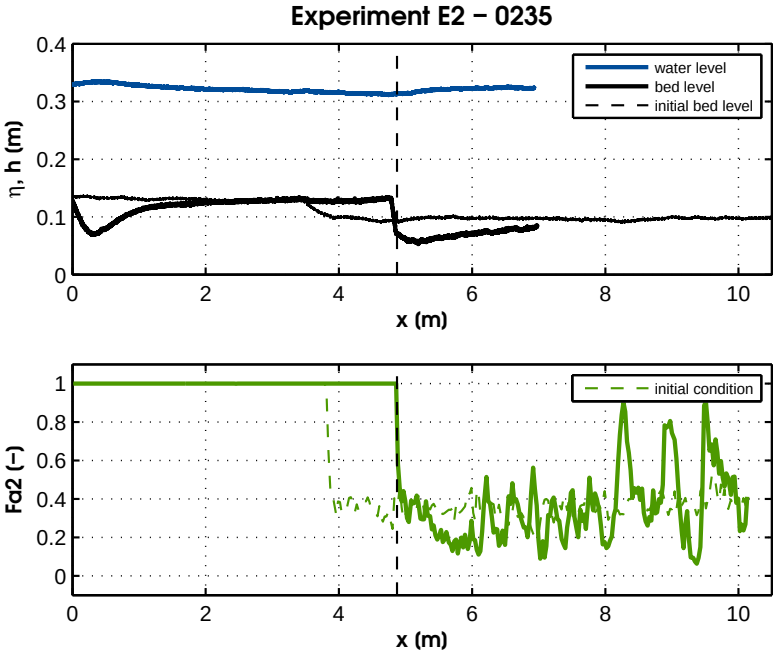

Figure B.12

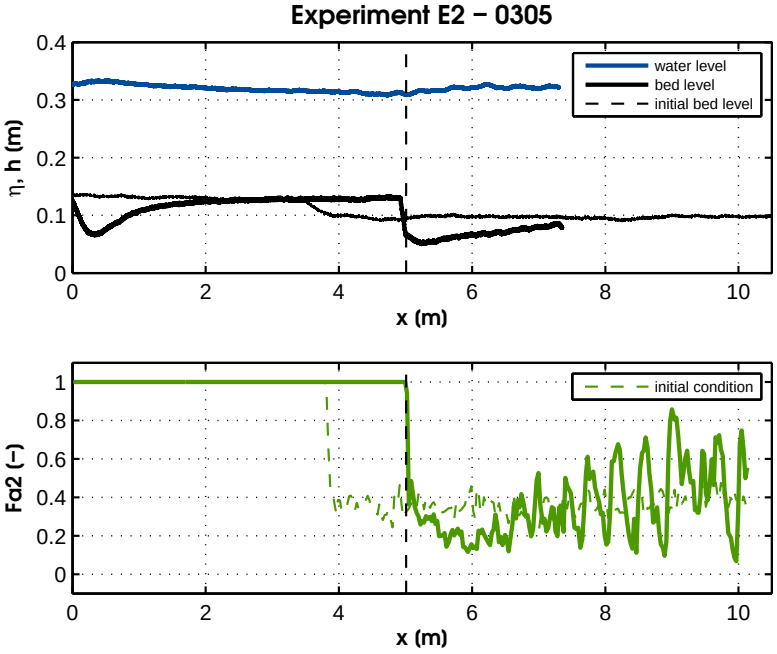

Figure B.13

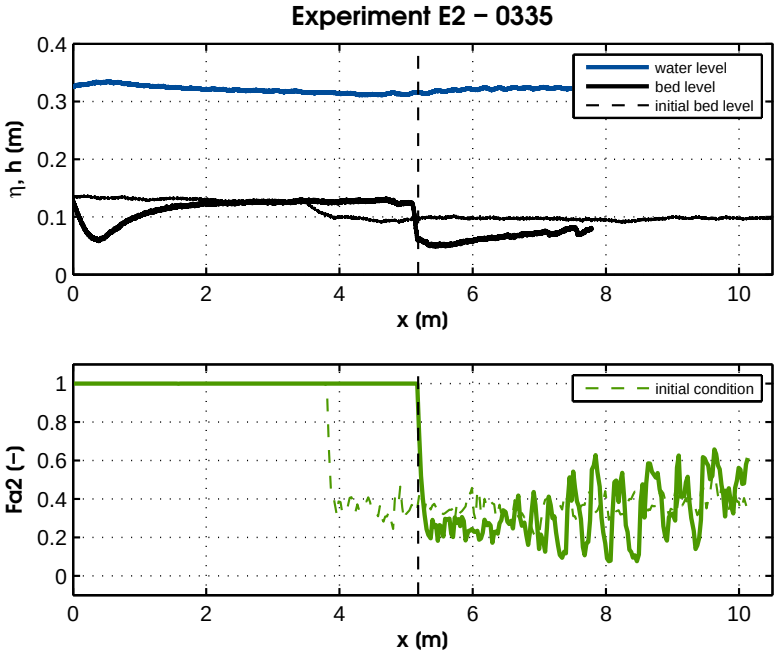

Figure B.14

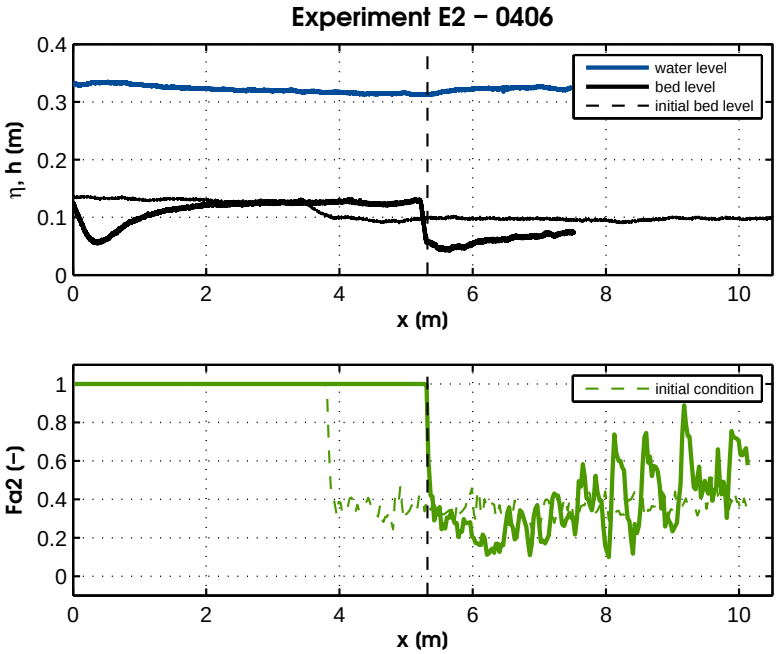

Figure B.15

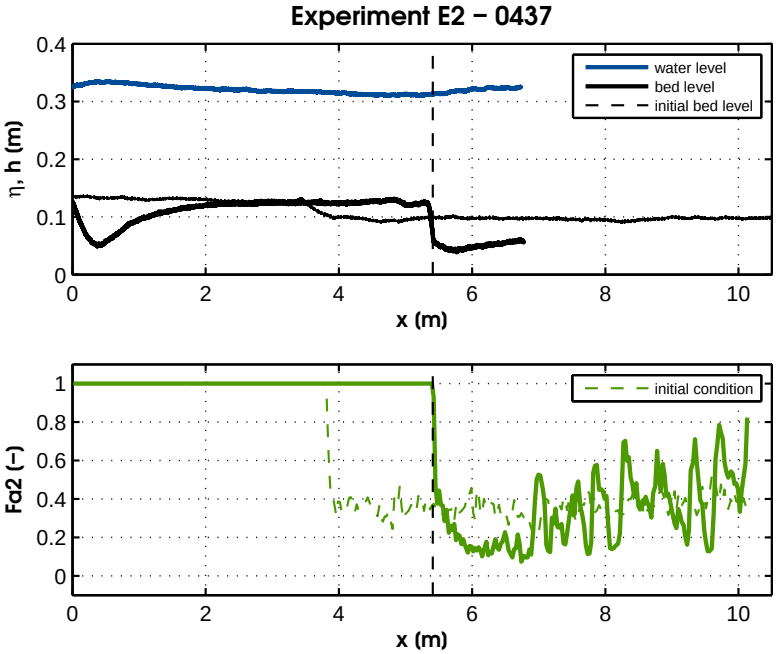

Figure B.16

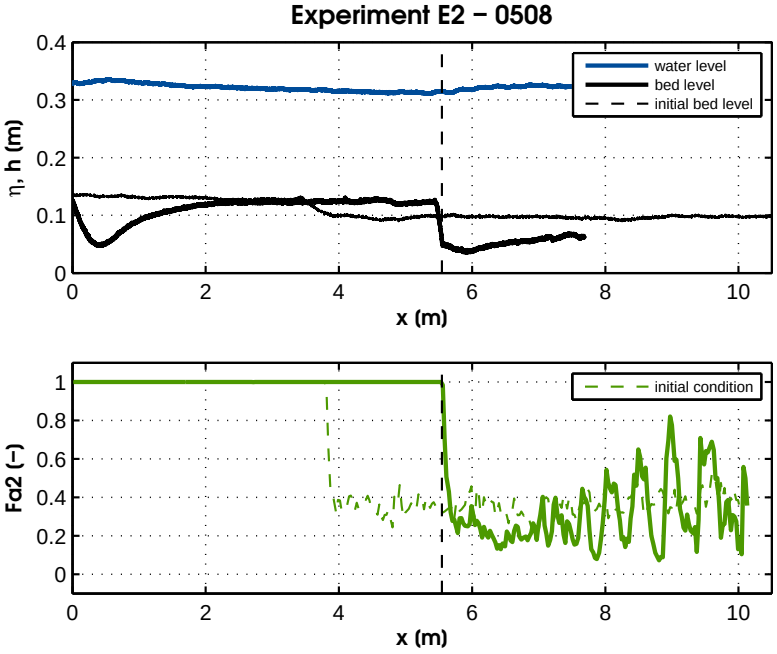

Figure B.17

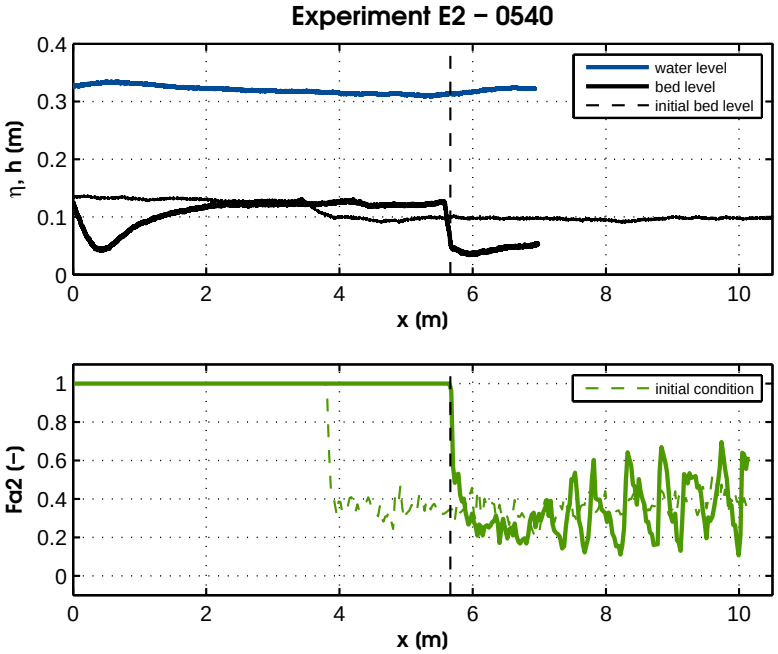

Figure B.18

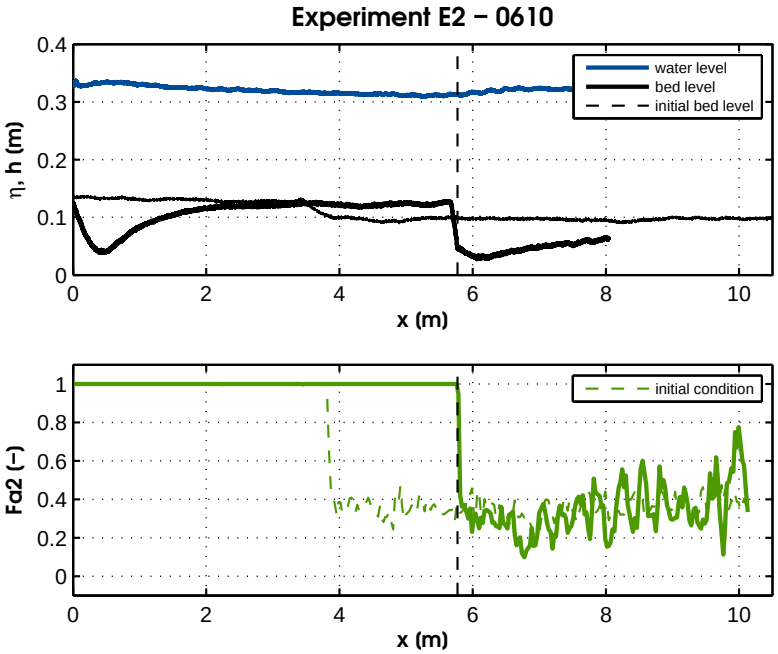

Figure B.19

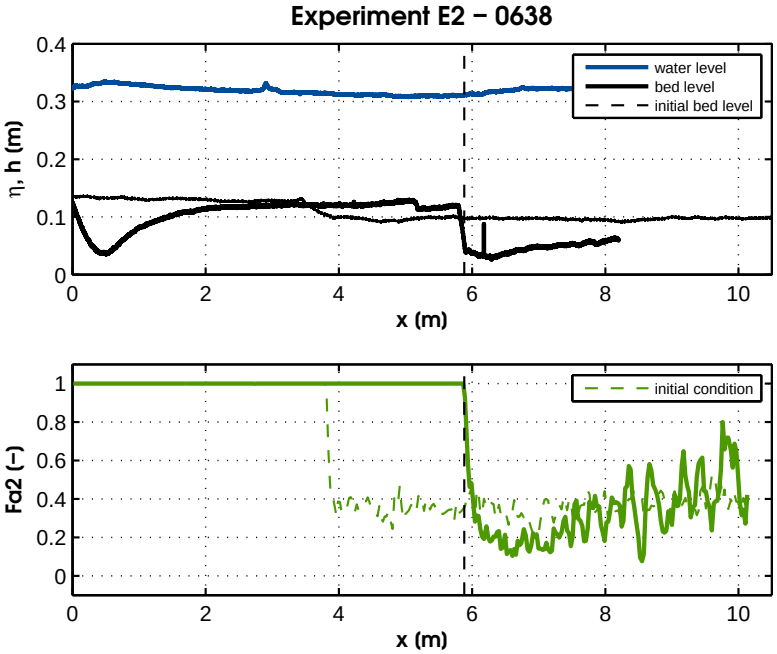

Figure B.20

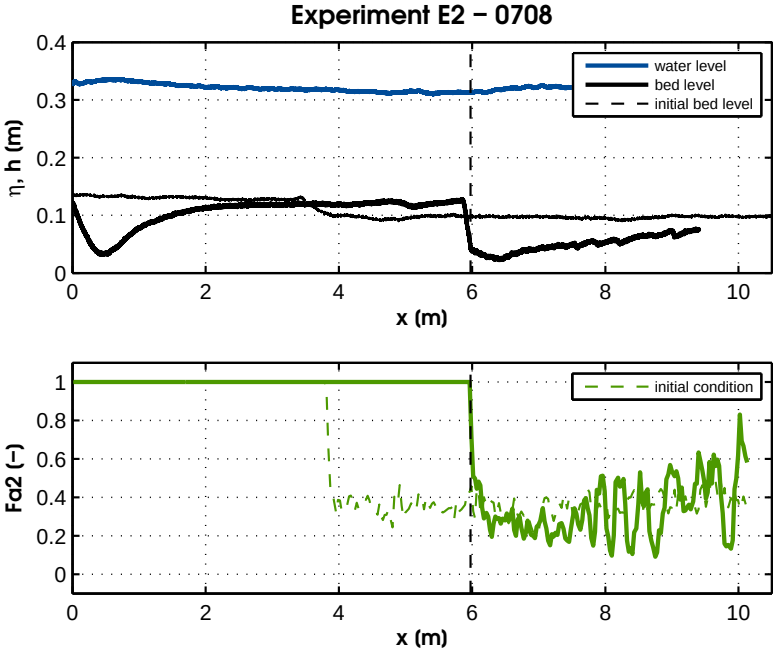

Figure B.21

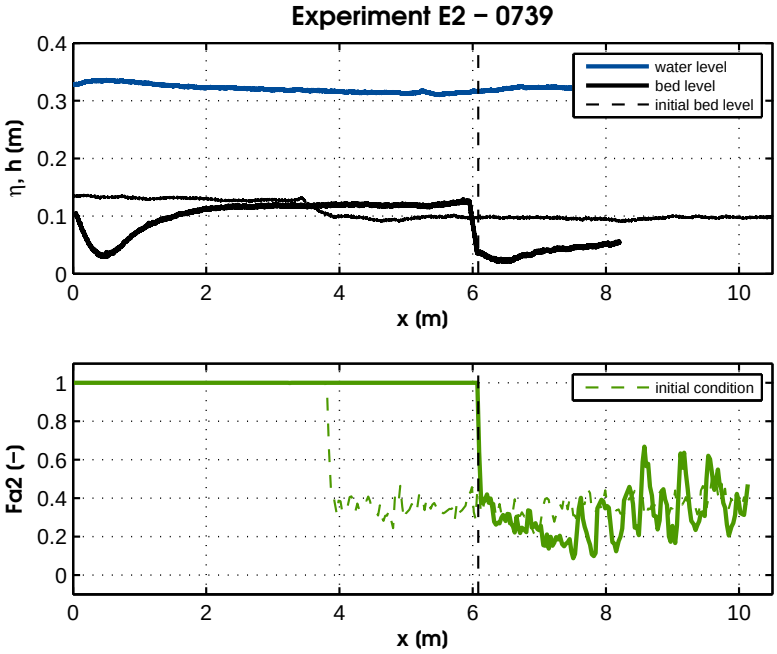
Experiment E2 – 0739
water level
bed level
initial bed level
η, h (m)
x (m)
initial condition
Fa2 (–)
x (m)

Figure B.22

C | Photographs of bed surface, Experiment E1

Time
[hh:mm]

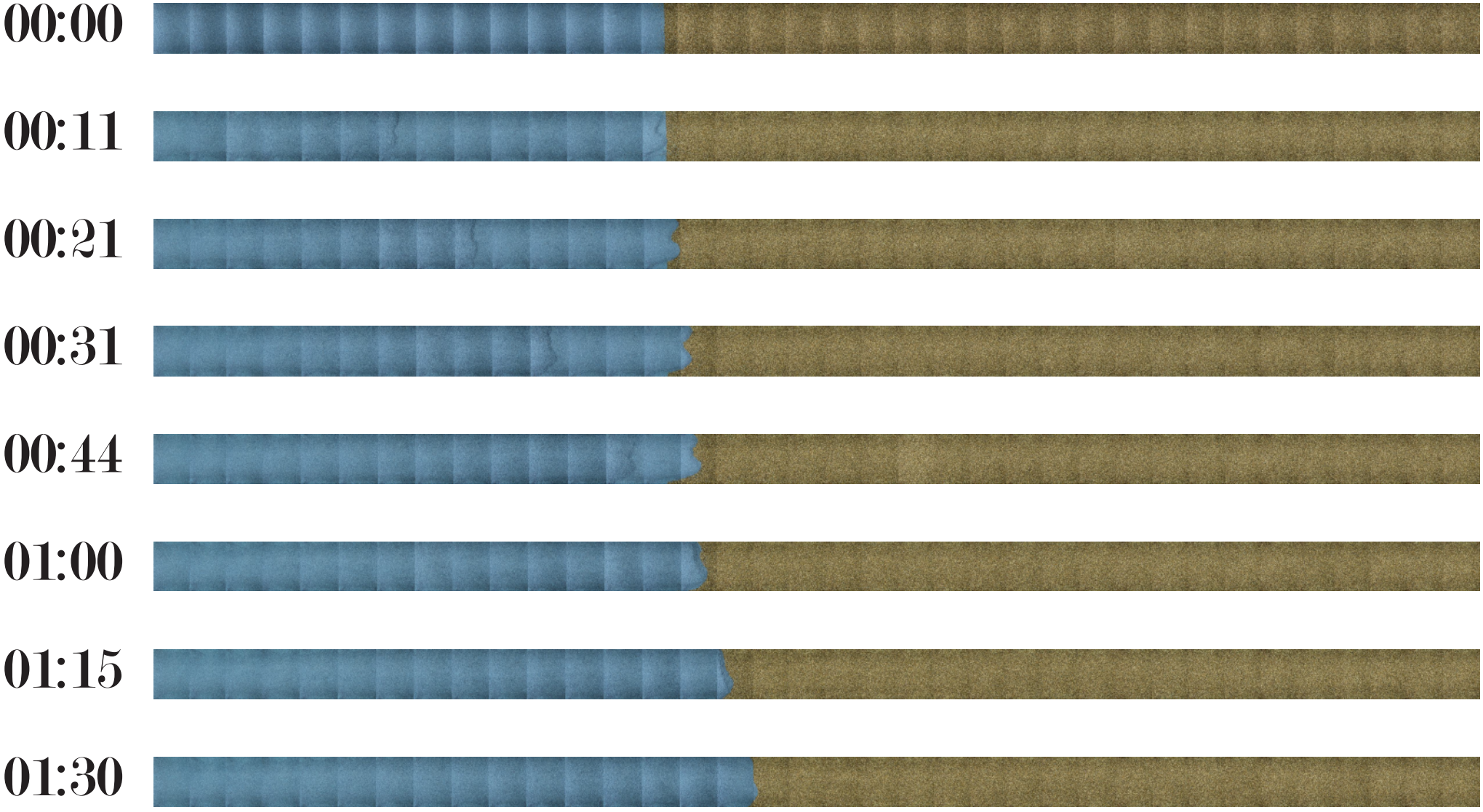

01:48

02:20

02:50

03:19

03:50

04:20

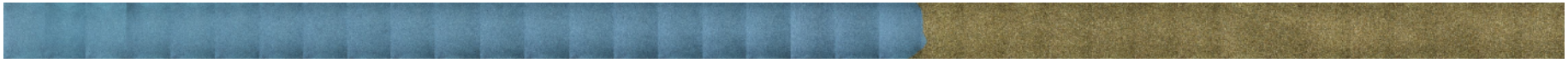

04:50

05:21

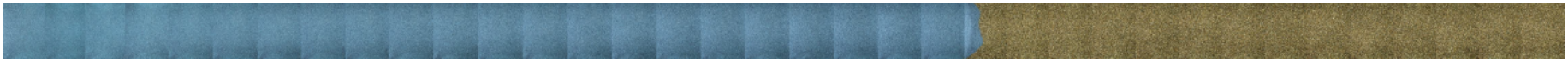

05:48

06:29

06:59

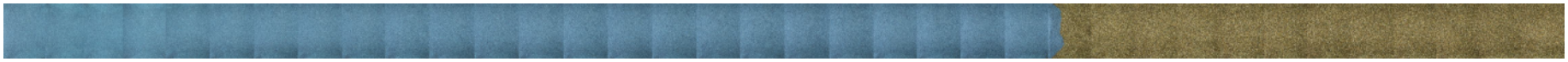

D | Photographs of bed surface, Experiment E2

Time
[hh:mm]

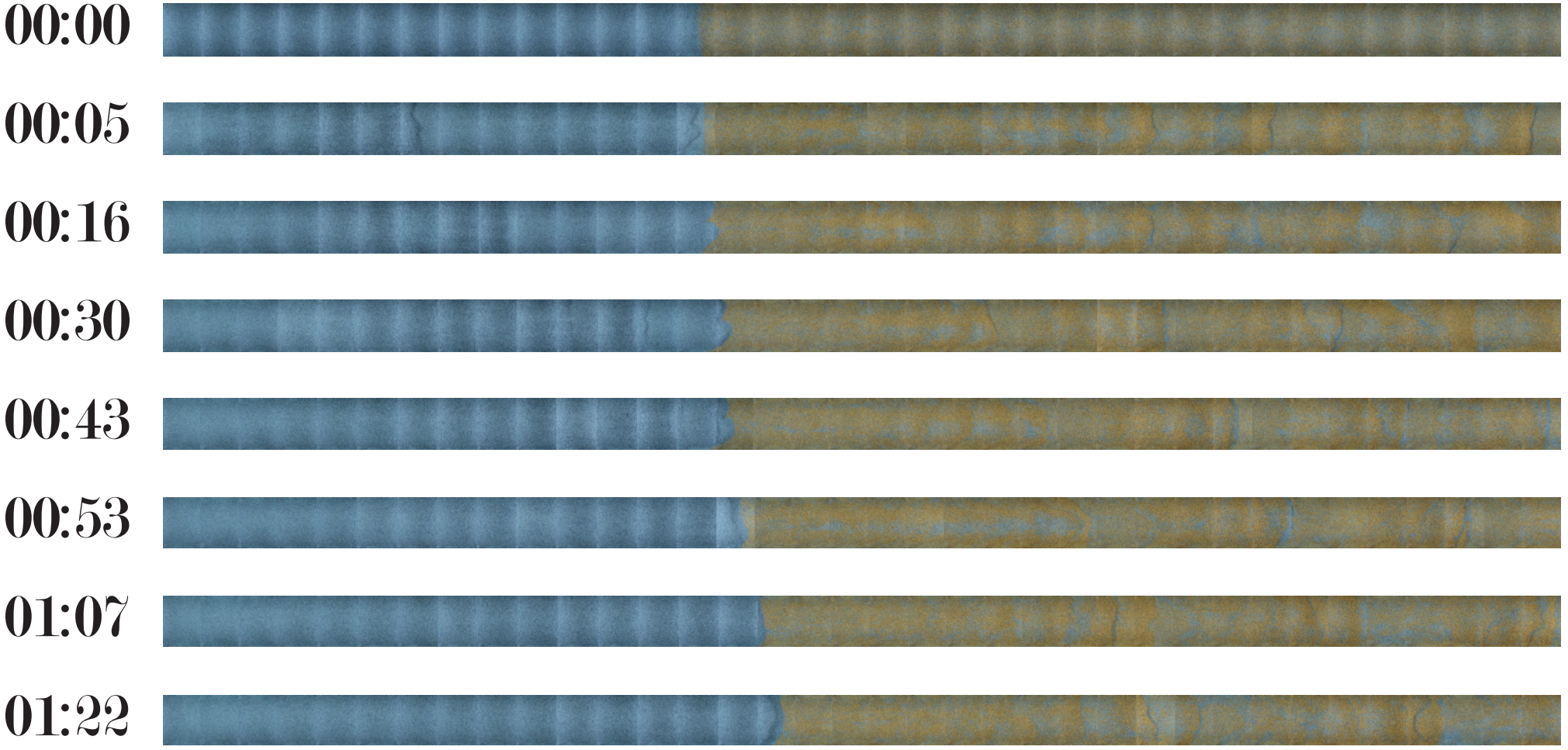

01:38

01:58

02:15

02:35

03:05

03:35

04:06

04:37

05:08

05:40

06:10

06:38

07:08

07:39